NEAR-WALL REACTION EFFECTS ON FILM-COOLED SURFACE HEAT TRANSFER

by

DANIEL ROBERT KIRK

B.S. Mechanical Engineering, Rensselaer Polytechnic Institute, 1997
M.S. Aeronautics and Astronautics, Massachusetts Institute of Technology, 1999

Submitted to the Department of Aeronautics and Astronautics
In partial fulfillment of the requirements for the degree of

DOCTOR OF PHILOSOPHY

at the

MASSACHUSETTS INSTITUTE OF TECHNOLOGY

[June 2003]
August 2002

Author ....
Department of Aeronautics and Astronautics
August 9, 2002

Certified by...
Ian A. Waitz
Professor of Aeronautics and Astronautics
Thesis Supervisor

Certified by...
Edward M. Greitzer
H. N. Slater Professor of Aeronautics and Astronautics

Certified by...
Gerald R. Guenette
Principal Research Engineer

Accepted by...
Edward M. Greitzer
H. N. Slater Professor of Aeronautics and Astronautics
Chair, Graduate Committee

Near-Wall Reaction Effects on Film-Cooled Surface Heat Transfer

by

Daniel Robert Kirk

Submitted to the Department of Aeronautics and Astronautics
on August 9, 2002, in partial fulfillment of the requirements for the degree of
Doctor of Philosophy

Abstract

As commercial and military aircraft engines approach higher total temperatures and increasing overall fuel-to-air ratios, there exists a potential for significant heat release to occur in the turbine if energetic species emitted from the combustor are further oxidized during interaction with film-cooling flows. Currently there is little basis for understanding the effects on aero-performance and durability due to such secondary reactions.

To study surface heat flux augmentation due to near-wall reactions, a shock tube experiment was employed to generate short duration, high temperature (1000-2800 K) and pressure (6 atm.) fuel-rich flows over a film-cooled flat plate. The relative increase in surface heat flux due to near-wall reactions was investigated over a range of fuel levels, mass blowing ratios (0.5-2.0), and Damköhler numbers (ratio of flow to chemical time scales) from near zero to 30. It was shown that significant increases in surface heat flux can be produced due to chemical reactions in the film-cooling layer. Under some conditions, the heat flux exceeded that obtained when no film-cooling layer was present on the surface.

A numerical tool was developed and showed good agreement with the experimental results for predicting changes in surface heat flux and film effectiveness in the presence of local reactions. Off-surface effects and changes in convective heat transfer coefficient were also evaluated. Realistic turbine and cooling flows were examined to ascertain the robustness of various cooling configurations to near-wall reactions.

The result of this work is a set of tools based on a group of parameters that can be used to assess changes in heat load due to near-wall reactions. The non-dimensional parameters are the Damköhler number (Da), mass and momentum blowing ratios (B and I), freestream energetic heat release potential (H^*), and scaled heat flux ratio (Q_s). The scaled heat flux ratio always increases with Damköhler number and depends on the structure of the cooling jet, but is not a function of the freestream fuel energy content.

Thesis Supervisor: Ian A. Waitz
Title: Professor of Aeronautics and Astronautics

Acknowledgements

Praise be to the God and Father of our Lord Jesus Christ, who has blessed us in the heavenly realms with every spiritual blessing in Christ. For he chose us in him before the creation of the world to be holy and blameless in his sight. In love he predestined us to be adopted as his sons through Jesus Christ, in accordance with his pleasure and will – to the praise of his glorious grace, which has freely given in the One he loves. In him we have redemption through his blood, the forgiveness of sins, in accordance with the riches of God's grace that he lavished on us with all wisdom and understanding.

Ephesians 1:3-8

All glory and praise to my Father

The completion of this thesis would not have been possible without the assistance, advice, and guidance from my thesis committee. Foremost, I would like to thank my thesis advisor, during both my masters and doctoral study, Professor **Ian A. Waitz**. In May of 1997, before I committed to attending MIT, Prof. Waitz told me, "My job is to provide as many opportunities as possible for you to shine." Those words have rung true over my five years at the Gas Turbine Laboratory, and for those opportunities I am grateful. I look forward to continuing our relationship in a professional capacity as well as my advisor and friend. Thanks to committee member Dr. **Gerald R. Guenette** for his expert help and support on numerous occasions, and specifically in the design and construction of the experiment. I have enjoyed our many conversations, both about research and many things non-engineering. Thanks to committee member Professor **Edward M. Greitzer** for his support and guidance throughout this project, and specifically for facilitating the development of the non-dimensional representation and careful review of the data. Thanks especially for his role in honing skills that I will use throughout my career: learning how to ask the appropriate key questions and how to deliver the important points.

The High Fuel-Air Research effort was sponsored by the support of Pratt & Whitney. Thanks to Drs. **Frederick Soechting, Charles Graves, Saadat Syed, Thomas Auxier, William Kvasnak**, and **Atul Kohli** of Pratt & Whitney, and Dr. **Catalin Fotache** of the United Technologies Research Center. At MIT, I have been fortunate to have worked with **Stephen P. Lukachko**, who is largely responsible for the foundations of this research, and the results presented in this thesis have benefited greatly from his input. Special thanks to the best undergraduate student I have ever worked with, **Krzysztof Fidkowski**.

I would also like to express my thanks and appreciation for my best pals at the lab, who will surely remain my close friends for life. These relationships are without doubt the best things that I leave MIT with. Thanks to **Spad** for always being the Spad, **CP** for being the Top Dawg, **Lohner** for being the Lohne Dawg, **Bot** for never being serious, **Sumita** for always being serious, and **B** for being an especially close friend to me. The memories that I share with each of you will always keep me laughing and I look forward to many more fun times. Other friends that have made my GTL experience more memorable include **D. Ward, Jon Protz, Amit Mehra, Adam London**, and **Brian Schuler**. To my pal **David Milanes**, best of luck as you continue the shock tube tradition and HFA research. Finally, a very special thanks to **Lori Martinez, Diana Park, Paul Warren, Victor Dubrowski, Jimmy Letendre**, and **Jack Costa**.

Serdecznie dziekuje dla mojej mamy I taty za wychowanie mnie w wierze I dla pracy w Jezusie Chrytisie. Dziekuje bardzo za wasza milosc I cierpliwosc, moje ciazka prace poswiecelem dla was. Unbound thanks to my dear parents for years of love and guidance, this thesis is dedicated to you.

Many pages of acknowledgments could be composed if I were to simply list the names of those that I am indebted to for support, friendship, advice, and prayer. My family and friends at home, undergraduate colleagues, and church friends would be at the forefront. I conclude here with a heartfelt thank you to those special individuals for supporting me through the conclusion of this chapter of my life. I proceed to the next with your support and with the words I shall strive to adhere to.

However, I consider my life worth nothing to me, if only I may finish the race and complete the task the Lord Jesus has given me – the task of testifying to the gospel of God's grace.

Acts 20:24.

This material is based upon work under a NSF Graduate Fellowship. Any opinions, findings, conclusions, or recommendations expressed by the author do not necessarily reflect the views of the NSF.

Table of Contents

Chapter 1

Chapter 2

Chapter 3

Chapter 4

Chapter 5

List of Figures

List of Tables

Nomenclature

Roman

A	pre-exponential factor
B	mass blowing parameter, $\rho_c u_c/\rho_\infty u_\infty$
C_p	constant pressure specific heat, (J/kg K)
Da	Damköhler number, τ_{flow}/τ_{chem}
D	cooling hole diameter, (m)
E_a	activation energy
EI	emission index
FAR	fuel-air ratio
h	convective heat transfer coefficient, (W/m^2 K)
H^*	heat release potential, $(T_{ad} - T_{t\infty})/T_{t\infty}$
I	momentum blowing parameter, $\rho_c u_c^2/\rho_\infty u_\infty^2$
k	thermal conductivity, (W/m K)
L	length scale, (m)
LHV	lower heating value
M	Mach number, u_∞/a_∞
NGV	nozzle guide vane
P	static pressure, (N/m^2)
Pr	Prandtl number, $C_p\mu/k$
$\dot{q}$	heat flux, (W/m^2)
Q_s	scaled heat flux ratio, $(q_{hot}-q_{cold})/(q_{max}-q_{cold})$
Re	Reynolds number, $\rho u_\infty x/\mu$
S	mixedness parameter, σ/ϕ
St	Stanton number, $h/u_\infty \rho Cp$
T	temperature, (K)
TIT	turbine inlet temperature
x	streamwise distance, (m)
X	mole fraction
y	vertical (normal to surface) distance, (m)
Y	mass fraction
z	lateral distance, (m)

Greek

ΔH_t	change in total enthalpy
ΔT_t	change in total temperature
ϕ	equivalence ratio
ϕ_{exit}	local equivalence ratio at combustor exit
ϕ_{local}	turbine flow equivalence ratio local to surface
ϕ_{streak}	initial streak equivalence ratio
η	film-cooling effectiveness, $(T_\infty - T_f)/(T_\infty - T_c)$
η_b	overall combustor/burner efficiency
η_{exit}	local efficiency at combustor exit
η_{local}	turbine flow combustion efficiency local to surface
κ	thermal diffusivity, (m^2/s)
μ	viscosity, $(N\ s/m^2)$
θ	hydrodynamic similitude scaling parameter, $(T_\infty - T_w)/(T_\infty - T_c)$
ρ	density, (kg/m^3)
σ	standard deviation
τ	characteristic time, (s)
ζ	penetration depth, (m)

Subscripts

ad	adiabatic
c	coolant
chem	chemical time to 95% completion
cold	non-reactive heat flux
d	driving
f	film
hot	reactive heat flux
max	maximum heat flux
o	oxidizer
t	total or stagnation quantities
test	test time
thresh	threshold
w	wall
∞	freestream

Chapter 1

Introduction

1.1 Background, Motivation, and Thesis Scope

Requirements for increased specific thrust and efficiency mandate high operating temperatures in modern aircraft engines and consequently higher fuel-to-air ratios in the combustor. As the fuel-to-air ratio is increased, there exists a potential for significant heat release to occur in the turbine if energetic species emitted from the combustor are further oxidized. Possible processes that lead to continued heat release downstream of the combustor are shown in the diagram of Figure 1.1.

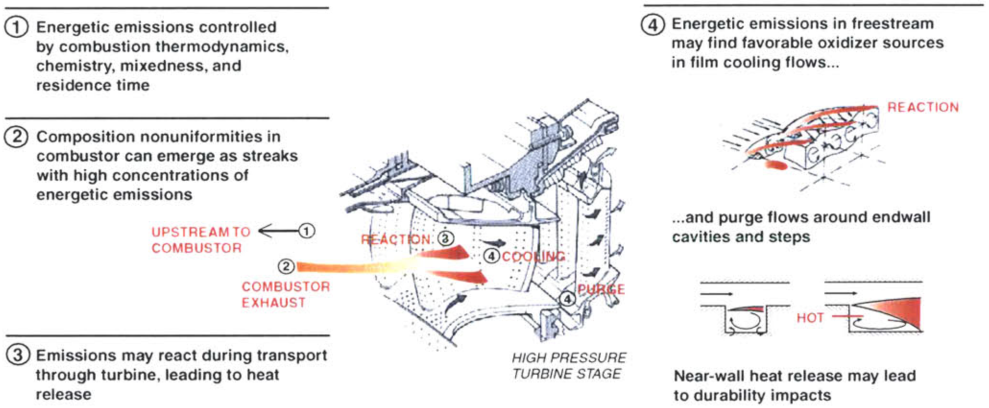

Figure 1.1: Phenomenology of Secondary Combustion in the Turbine

The source of these reactive species entering the turbine may be combustor unmixedness, such as fuel-rich streaks, or limitations on chemical residence time. Even a perfectly mixed flow, as fuel-to-air ratios approach stoichiometric levels, increased combustor exit concentrations of CO, OH, H_2, and O are thermodynamically favored. The decreasing temperatures and pressures along the turbine flow path encourage these species to recombine and subsequently raise the effective temperature of the turbine freestream flow. If these energetic species pass near film-cooled turbine surfaces, they may interact with the coolant air leading to elevated surface heat fluxes. In some cases, the heat flux may be greater than if no cooling were present. Such supplementary heat loads must be quantified so that suitable compensation in film-cooling strategies or structural robustness may be made. Currently there is little basis for understanding the effects on aero-performance and durability due to such secondary reactions.

With the potential for near-wall reaction to be more prevalent as combustor fuel-to-air ratios increase, it is the aim of this thesis to take the first steps toward understanding and suggesting how to design for near-wall secondary reactions. In this context, a set of governing parameters was developed which are used to describe and characterize the influence and effect of near-wall secondary reactions on surface heat flux. These parameters allow estimates to be made on the potential impact to film-cooled turbine surfaces over a range of flow and chemical time scales, blowing parameters, and freestream fuel levels. Parametric studies of film-cooling hole spacings were performed over a range of conditions in an effort to reduce heat load to the surface in the presence of near-wall reactions.

1.2 Literature Review

Although there is no formal literature base for the interaction of a film-cooling layer with a reacting freestream flow, several related areas of study exist that map to the phenomenology of Figure 1.1, these include: combustor exit flow composition and mixedness, streak migration from the combustor through the turbine, film-cooling methods and design, reacting shear layer and boundary layer flows, and analyses of heat release potential at turbine sites due to reaction.

1.2.1 Combustor Exit Speciation and Mixedness

The fluid and chemical conditions that lead to near-wall surface reactions arise from some level of residual fuel or reactive species exiting the combustor un-burned. The energetic species may then react en route or at turbine film-cooled surface sites. A categorization and understanding of the potential levels of energetic species exiting the combustor is essential to estimating the magnitude of heat release which can be achieved further downstream. The first study of this type was completed in Reference [39] and outlined the range of energetic emissions into the turbine which could arise due to combustor inefficiency and unmixedness over a range of modern and future aircraft engine operating conditions. A summary of the results of this work will be presented in Section 1.2.5 and in Chapter 2.

Research that describes the velocity, turbulence, and temperature profiles from combustor exit flows can be found in References [8, 15]. These works indicate that combustor exit flows may contain regions where the temperatures may range from compressor discharge levels to those exceeding the turbine allowable metal temperature by 250-520 K. Since the time for which it takes chemical reactions proceed to completion is a strong function of temperature, such a temperature span provides a wide range of chemical time scales. Turbulence level in the combustor exit flow is important as it may impact the convective heat transfer to the downstream turbine blades as well as on the combustor liner. Turbulence levels are also important for determining mixing rates or reactive streaks and thus determining their behavior as they move through the turbine as discussed in Appendix A.

1.2.2 Combustor Hot Streak Migration

The combustor non-uniformities discussed above may manifest themselves as slugs or streaks of fluid that exit the combustor and traverse to and through the turbine. Research has been completed in understanding how and where such streaks will convect as they travel to the turbine, as well as their impact on turbine durability, [8, 19, 21, 23, 30, 43, 48, 49]. The work is important for assessing the conditions under which reactive streaks may migrate to and interact with film-cooling layers. For convenience, several of these are summarized in Table 1.1.

Table 1.1: Summary of Literature Review on Hot Streak Migration and Turbine Durability

Reference	Relevance
Dorney, Gundy-Burlet and Sondak (1998): A Survey of Hot Streak Experiments and Simulations, [6].	Overview of hot streak body of knowledge (experiments and simulations) amassed over the last 20 years.
Bulter, Sharma, and Dring (1989): Redistribution of an Inlet Temperature Distortion in an Axial Flow Turbine Stage, [5].	Pioneering investigation of hot streak phenomena in turbine. Demonstrated inadequacy of 2-D schemes to reproduce experimental results.
Roback and Dring (1992): Hot Streaks and Phantom Cooling in a Turbine Rotor Passage Part 1 - Separate Effects, [48]	Parametric dependence of streak transport.
Roback and Dring (1992): Hot Streaks and Phantom Cooling in a Turbine Rotor Passage Part 2 - Combined Effects and Analytical Modeling, [49]	
Krouthen and Giles (1988): Numerical Investigation of Hot Streaks in Turbines, [34].	
Dorney, Davis, Edwards and Madavan (1992): Unsteady Analysis of Hot Streak Migration in a Turbine Stage, [8].	3-D computational comparisons with experimental data, indicated 3-D nature of the rotor flow field.
Gundy-Burlet and Dorney (1996): Three-Dimensional Simulations of Hot Streak Clocking in a 1-1/2 Stage Turbine, [20].	
Prasad and Hendricks (1999): A Numerical Study of Transport Mechanisms in Axial Flow Turbines, [47].	Demonstrates that although rotor flow field is highly unsteady, quantitative estimate of the radial transport velocity may be obtained from steady analyses. Suggests control of radial transport through blade twist variation.

In secondary flows due to radial temperature distortions, endwall vortices and tip leakage flow redistribute the mid-span hot fluid toward the tip and hub walls. The gas segregation caused by circumferential distortion leads to higher temperatures on the pressure side than the suction side of a turbine airfoil. This effect can be reduced by increasing the flow coefficient (decreasing wheel speed). Furthermore, preferential migration to portions of the airfoil, or tip and hub regions within the turbine, may lead to increases in heat loading of up to 100 K, [48, 49]. Numerical and analytical assessment (secondary flow arguments) of the transport mechanisms responsible for streak migration in turbines have also been used to develop 'reverse twist' blade geometries that can be employed to direct hot streaks toward the center of the blade passage rather than toward the tip region, [47].

Although such work on thermal streak migration is important and demonstrates the impact that hot streaks may have on turbine durability, no work has been completed to determine what may happen if such a streak is fuel-rich and encounters a film-cooled surface. Furthermore, no studies have been completed to assess the fate of fuel-rich or fuel-lean streaks as they migrate and react from the combustor exit through the turbine. A component of the work presented in this thesis is to assess the fate of such fuel-rich streaks, and to determine whether such streaks will react or mix-out with the freestream flow prior to arrival at film-cooled turbine sites. Such a reactive streak analysis is summarized in Appendix A, which also contains additional literature references relevant to hot streak behavior in the combustor-turbine flow-field.

1.2.3 Film-cooling Review

If the fuel-rich streaks described above arrive at oxygen-rich film-cooled turbine surfaces, a potential exists for chemical reactions to take place near the surface. No film effectiveness or cooling performance data exist for cases where the freestream is fuel-rich, and establishment of such a data base, over a range of pertinent turbine parameters, is one of the primary goals of this thesis. For this reason an experiment and numerical tool were employed to probe such near-wall reaction phenomena. The body of literature on film-cooling studies for gas turbine applications is extensive, and the focus of this review is to summarize those works that directly influenced the development of this thesis.

The influence of mass blowing ratio on film effectiveness is summarized in Reference [22] over a range of blowing ratios and freestream conditions. These correlations are used in later parts of this thesis to compare with experiments and computations. References [17, 16, 41] were used in the experimental and numerical studies for understanding the behavior, mechanisms, and differences in film effectiveness of attached and lifted film-cooling jets. A series of papers, [1, 46, 58], facilitated development of the governing parameters used to describe the film-cooling flow over a range of freestream and coolant conditions. These works outlined the effects of temperature ratio on the hydrodynamics of film-cooling and the influence on adiabatic film effectiveness for an experimental configuration identical to that used in the experiments of this work. Correlations that are developed in this work for reactive cases are based on methods described in Reference [37] for a series of round film-cooling hole arrays.

1.2.4 Reacting Shear Layer and Boundary Layer Flows

Insight into the problem this thesis addresses can be gained through a review of research done on chemically reacting boundary layer flows. Reacting boundary layers can either be laminar or turbulent, however, this review is dedicated to the latter case since those occurring in practice in the turbine are of this type. For equilibrium cases, or cases where the chemical kinetics are taking place infinitely fast, the solution of the problem can usually be obtained in terms of existing solutions of the conventional boundary layer equations, and the problem is more or less reduced to algebraically reevaluating the proper energy, or thermal, driving potential. An argument made in this thesis will point to the fact that the change in surface heat flux due to near-wall reactions can be established by determining what the increase in driving temperature is above the non-reactive case. Also, when chemical reactions are considered to occur infinitely fast, the governing equations are essentially the same as those for chemically inert boundary layers, and the chemical reactions are governed by the characteristics of the boundary layer alone.

Nonequilibrium cases occur when the chemical reactions proceed at a finite rates and are more complicated. The most interesting features of the chemically reacting boundary layers are due to coupling of the boundary-layer characteristics with the finite-rate chemical reactions. Studies of reacting turbulent boundary layers are summarized in Reference [36].

Several works [25, 59] have developed solutions for and conducted experiments on diffusion flames in two-dimensional, accelerating mixing layers that have application for reacting wall boundary layers. These results have shown that in the presence of exothermic reaction, there are non-monotonic velocity and density variations across the layer, meaning the peak velocity and a minimum density occur near the middle of the layer. The results also showed that the growth rate of the layer decreases slightly with increasing heat release. The overall entrainment into the layer is substantially reduced as a consequence of heat release, which is consistent with a corresponding reduction in turbulent shear stresses. Mean temperature rise profiles, normalized by the adiabatic flame temperature rise, were not greatly changed in shape over the range of heat release performed in these studies. A similar scaling is employed in the experiments presented in this thesis, but applied to heat flux, rather than temperature rise.

1.2.5 Summary of Preliminary High Fuel-To-Air Research

An analysis that ties many of these concepts together and forms the motivation for the research presented in this thesis is summarized in Reference [39]. In addition to providing estimates on combustor exit flows, that work takes the first steps toward estimating the bounds on the magnitude of energy release (in terms of a total temperature rise, ΔT_t) that may take place in the turbine due to secondary reactions. Results relevant to the present work are:

1. Identification of some of the parameters on which the energy release within the turbine depends on, namely the fluid and chemical time scales and freestream fuel energy content.
2. Characterization of modern and future combustor exit speciation, which provided insight into the levels of energetic emissions that may be encountered by film-cooled turbine surfaces.
3. Development of a 'worst case scenario' heat load impact method to estimate the fluid and chemical times associated with flow through the turbine, as well as the total temperature rise associated with the fuel-rich freestream encountering an oxygen rich source.

More details on this work are found in Chapter 2. Although this work provides bounding estimates, no detailed experimental or numerical measurements on the interaction of a fuel-rich freestream with a film-cooling layer at turbine conditions have been completed. Nor does there exist a complete description of the phenomena of near-wall reactions in terms of governing parameters. As near-wall reaction occurrences become more prevalent such research is vital to future engines designs and it is this endeavor that forms the focus of this thesis.

1.3 Objectives

The research in this thesis addressed the problem of a reactive freestream flow interacting with a film-cooling layer. The specific research objectives were:

1. To design and perform an experimental investigation of changes in surface heat flux due to the interaction of a fuel-rich freestream with a film-cooling layer over a range of turbine parameters including: freestream fuel energy content, blowing ratio, and flow and chemical time scales.
2. To characterize the thermodynamic, chemical, and fluid drivers of turbine heat release through a set of parameters and models which can be used to describe the features of near-wall reactions.
3. To apply these models to estimate changes in surface heat flux over a range of turbine conditions, to predict when current cooling strategies will deteriorate, and to determine what types of film-cooling scenarios may lead to extended surface durability.
4. To define the applicability and limitations of these parameters and simplified models in the design process.

1.4 Contributions

Contributions of this thesis include:

1. The first experimental investigation of changes in surface heat flux due to near-wall reactions were completed. The results enable predictions of changes in surface heat flux to the surface as a fuel-rich freestream interacts with a film-cooling layer over a range of turbine parameters, including freestream fuel level, blowing ratio, and changes in the ratio of flow to chemical time-scales.
2. A set of governing non-dimensional parameters were identified and shown to characterize the behavior of these flows. As an example, increasing the Damköhler number increases the level of augmented heat flux to the surface for constant freestream fuel concentration and blowing ratio. However, the level of fuel in the freestream is critical to assessing the impact to the surface in terms of total temperature rise and consequently heat flux.
3. A numerical tool predicted changes in surface heat flux and film effectiveness over a range of important parameters. This tool enabled understanding of the differences in surface heat flux attributable to attached versus lifted film-cooling jets is crucial to placement of film-cooling holes. Using the numerical tool, any current design can be placed in scrutiny of increased freestream fuel levels or Damköhler numbers to establish when such a design is no longer an effective means of protecting the surface.
4. Limitations on the set of governing parameters and simplified tools were determined. The set of governing parameters developed from the experiments and numerical studies were based on results from a 35° injection cooling hole on a flat plate.

1.5 Thesis Overview

The next chapter of this thesis presents the important non-dimensional parameters that can be used to characterize the flow of interest. Also contained in this chapter is an overview of the characterization of combustor exit speciation and the characteristic time scale method used to estimate Damköhler numbers and total temperature rise. Chapter 3 presents the experimental methods used to make reactive heat transfer measurements on a film-cooled flat plate over a range of turbine conditions. Chapter 4 presents an analysis of this data and the evidence to support that the selected group of parameters described in Chapter 2 is complete. Chapter 5 continues with a numerical study of near-wall reactions and film-cooling configurations. Chapter 6 provides case study examples which demonstrate the utility of the work and how the tools may be incorporated into a design process. Chapter 7 presents a thesis summary and conclusions, as well as a brief discussion of future work that will extend this research to account for additional cooling geometries in the turbine such as step re-circulation zones. Appendix A discusses a set of simplified models which can be employed to study the fate of a fuel-rich streak as it convects from the combustor exit into and through the turbine providing estimates of mixing and fuel levels at particular turbine locations.

Chapter 2

Governing Physical Parameters

The primary purpose of this chapter is to introduce parameters that can be used to characterize the influence of secondary reactions on surface heat flux. Although these parameters were derived from a series of analytical, experimental, and computational efforts (Chapters 3-5), they are presented at the outset to frame the problem. Additionally, this chapter describes the range of energetic emissions expected from modern and future combustors, thus providing guidance for the experimental and computational studies. Finally, an overview of the characteristic flow and chemical time scale method, as well as total temperature increases due to secondary reactions, is presented.

2.1 Relevant Physical Parameters

The governing non-dimensional parameters and the section of this chapter in which they are developed and described are summarized in Table 2.1:

Table 2.1: Governing Non-Dimensional Parameters

Parameter	Definition	Description	Section
Damköhler Number, Da	$Da = \frac{\tau_{flow}}{\tau_{chem}}$	Comparative ratio of flow time (convective or mixing) to chemical (ignition or completion) time.	2.2
Freestream Fuel Energy Content, H^*	$H^* = \frac{\Delta h_t}{h_{t\infty}}$	Heat release parameter used to define the increase in total fluid enthalpy normalized by the freestream total enthalpy.	2.3
Blowing Parameters, B, I	$B = \frac{\rho_c u_c}{\rho_\infty u_\infty}, I = \frac{\rho_c u_c^2}{\rho_\infty u_\infty^2}$	Mass and momentum blowing parameters specifying the mass and momentum fluxes of the film-coolant to that of the freestream flow, respectively.	2.4
Scaled Heat Flux Ratio, Q_s	$Q_s = \frac{q_{hot} - q_{cold}}{q_{max} - q_{cold}}$	Ratio of increase in surface heat flux due to reaction over a non-reactive scenario normalized by the maximum possible heat flux that can be attained over a non-reactive scenario.	2.5

In forthcoming chapters it is shown that these parameters are a useful way to describe the changes in surface heat flux due to the presence of local reaction. The next several sub-sections discuss the development of each of these parameters.

2.2 Comparing Flow and Chemical Time Scales: The Damköhler Number

The potential impact of heat release (either freestream oxidation or interaction with film-cooling layers) depends on the convective, mixing, and chemical processes taking place within the combustor and turbine. The Damköhler number, defined as the ratio of a characteristic flow time, τ_{flow}, to a characteristic chemical time, τ_{chem}, is used to capture the macroscopic physical features controlling the flow-chemistry interactions:

$$\mathrm{Da} = \frac{\tau_{\mathrm{flow}}}{\tau_{\mathrm{chem}}} \tag{2.1}$$

The numerator of the Damköhler number is a flow time. For durability considerations, this is taken as a convective flow time, τ_{conv}, over a component, such as a blade chord or between film-cooling holes. In Chapter 3, this value will be taken as the time for the freestream flow, u_∞, to travel over 10 cooling hole diameters, or $\tau_{flow}=10D/u_\infty$. Mixing time scales, τ_{mix}, associated with both turbulent diffusion in the freestream and decay of film-cooling effectiveness may also be used in appropriate circumstances [39]. Mixing can play an important mitigating role, for example by diffusing streaks of energetic species en route to the turbine or by limiting the rate at which these species combine with film-cooling flows.[1]

The denominator of the Damköhler number is the time it takes for chemical reactions to proceed. The relevant chemical times are the time required for a given mixture to ignite, τ_{ign}, and the time required to complete the reaction process, τ_{react}, which are further discussed in the next section. Chemical times are determined using a constant pressure, adiabatic, chemical kinetics calculation for a homogenous flow [29, 39]. Energy released during reaction is assumed to result in a temperature rise with no contribution to or adjustment of the flow kinetic energy. The calculations are performed at the greatest local temperature under the assumption that the hot-side temperature of a mixing-layer drives ignition and reaction [12]. For example, in situations where the core flow encounters a colder film-cooling flow, the freestream temperature, T_∞, is used in the calculation.

The magnitude of the Damköhler number is indicative of the potential for and character of a reaction. For cases where $\mathrm{Da} \ll 1$ there is not enough time for reactions to take place during the traverse of the flow over the blade or in between film-cooling holes. When $\mathrm{Da} \gg 1$ ample time exists for reactions to proceed to completion and for maximum heat release. If the ratio is near unity, heat release will occur in a distributed manner and the maximum local temperature increase may not be realized. In any case, the impact on heat transfer is related to the change in local driving temperature, but mixing has a key role in determining the extent of impact.

2.3 Potential Heat Release and Freestream Fuel Energy Content, ΔT_t and H^*

The local concentration of energetic emissions partly determines the potential for energy release. An energy release parameter, here defined as a maximum increase in total temperature, ΔT_t, is used to specify an upper limit on the magnitude of impact. The chemical time scales τ_{ign} and τ_{react} are specified explicitly in

---

[1] In Chapters 4 and 5 it will be shown that this mixing time scale of freestream and coolant flows can be related to the slope of a line on a Q_s versus Da plot for a given blowing parameter, B or I.

reference to ΔT_t. For this study, ignition is defined as the time to reach 5% of ΔT_t and the completion of reaction is defined as the time to reach 95% of ΔT_t. The value of ΔT_t is determined by the adiabatic flame temperature and bounds the magnitude of maximum heat release. The chemical composition of the turbine flow sets the available energy. Pertinent to secondary combustion, the available energy is specified with reference to the lower heating value (LHV), again an upper limit. Local turbine temperatures and pressures are used to specify the thermodynamic state of the mixture prior to combustion. The range of energetic emissions that can be expected to occur from modern and future engines will be discussed in more detail in Section 2.6.

The freestream energy content can be defined in several ways, as described in Reference [39]. A heat release parameter, H^*, which is closely related to the total temperature rise, is used throughout this work. H^* is defined as the ratio of the potential enthalpy change due to reaction normalized by the freestream total enthalpy, $h_{t\infty}$, as shown in equation 2.2.

$$H^* = \frac{\Delta h_t}{h_{t\infty}} \approx \frac{\Delta T_t}{T_{t\infty}} \qquad 2.2$$

H^* as a metric for the potential energy release content of the freestream is a versatile and easy to use quantity that can be compared between different engines, experiments, and computational cases.

2.4 Mass and Momentum Blowing Parameters, B and I

Parameters that govern the hydrodynamics of the jet to freestream interaction and the associated heat transfer include the cooling hole geometry and coolant-to-freestream ratios of density, velocity, mass and momentum flux. The mass flux ratio, B, and the momentum flux ratio, I, are defined as:

$$B = \frac{\rho_c u_c}{\rho_\infty u_\infty}, I = \frac{B^2}{DR}, I = \frac{\rho_c u_c^2}{\rho_\infty u_\infty^2} \qquad 2.3$$

The mass flow blowing parameter, B, is the appropriate parameter for heat transfer studies because surface heat flux scales with the mass flow rate, ρu, passing over the surface. The momentum blowing parameter, I, is the appropriate parameter for describing whether the film-cooling jet is attached or lifted off the surface. For round 35° injection film-cooling-holes, the value that distinguishes whether the jet is attached or lifted from the surface is $I \sim 0.7$ [16]. For the experimental and numerical cases, both the mass flow and momentum blowing parameters are provided. It will be shown that the location of the maximum surface heat flux depends on whether the cooling jets are attached or lifted from the surface, although the magnitude of the maximum heat flux is relatively consistent for a given Da and H^*.

2.5 Scaled Heat Flux Ratio, Q_s

In order to apply the experimental and computational results, the data must be scaled so that it can be referenced to other conditions.[2] This is accomplished using the following scaling:

$$Q_s = \frac{q_{hot} - q_{cold}}{q_{max} - q_{cold}} = \frac{q_{hot} - q_{cold}}{q(T_{ad}) - q_{cold}} \qquad 2.4$$

The maximum possible heat flux, q_{max}, is that which would be achieved if the local reaction proceeded to the adiabatic flame temperature, $T_{ad}=T_{t\infty}+\Delta T_t$. The scaled heat flux ratio, Q_s, represents how much surface heat flux augmentation was achieved for any given situation compared to how much augmentation could possibly have been achieved. The q_{hot} and q_{cold} heat fluxes are measured directly from the surface of a turbine blade, experiment, or computation. The maximum temperature, T_{ad}, is calculated from knowledge of H^* and an empirical correlation for the heat transfer coefficient.[3] Thus if $q_{hot}=q_{cold}$, 0% of the potential augmentation was achieved, and if $q_{hot}=q_{max}$, 100% of the possible augmentation was achieved. It will be shown in Chapter 4 that the scaled heat flux ratio is a function of cooling hole geometry, Da, and the blowing ratio, but not a function of H^*. Additional discussion on the models and assumptions used to calculate the change in convective heat transfer coefficient, which is inherent in Equation 2.4, will be discussed in Section 5.3.2.

2.6 Range of Combustor Exit Emissions Characterization

Combustor unmixedness and inefficiency are primarily responsible for energetic emissions into the turbine [39]. The purpose of this section is to present three representative cases where local speciation is determined to estimate the potential magnitude of secondary reactions for current and future engines. For these estimates, it is assumed that the combustor exit composition is a good approximation for mixtures found through the turbine, with the exception that local mixing with film-cooling air may alter the composition. Appendix A discusses this assumption through an analysis of the mixing of fuel-rich streaks emitted by the combustor. It is shown that for any streaks larger than about 5% of span, a portion of the fuel-rich streak will arrive at turbine sites undiluted by the surrounding flow.

Turbine flow compositions are constructed by tracking a fluid streak with an assumed fuel type and initial equivalence ratio, ϕ_{streak}, that reflects the mixedness of the combustor. To estimate the post-combustor composition, equilibrium is calculated for a specified temperature and pressure relevant to the local site. Finally, the mixture is perturbed to account for mixing with oxidizer associated with local

---

[2] The need for such a scaling will be further discussed in Chapter 4 due to the differences in wall temperature between the shock tunnel experiments and the conditions that exist within actual gas turbines.

[3] The influence of near-wall reactions on heat transfer coefficient over a range of temperatures, H^*, B, I, and Da will be discussed in Chapter 5. It was found that the non-reactive and reactive heat transfer coefficients differed by around 20% for turbine conditions, indicating that the maximum heat flux to the surface is primarily a function of driving temperature rather than a change in profile.

cooling flows to provide 'a worst case' near surface equivalence ratio, ϕ_{local}. This process and the range of turbine flow conditions that result are illustrated in Figure 2.1.

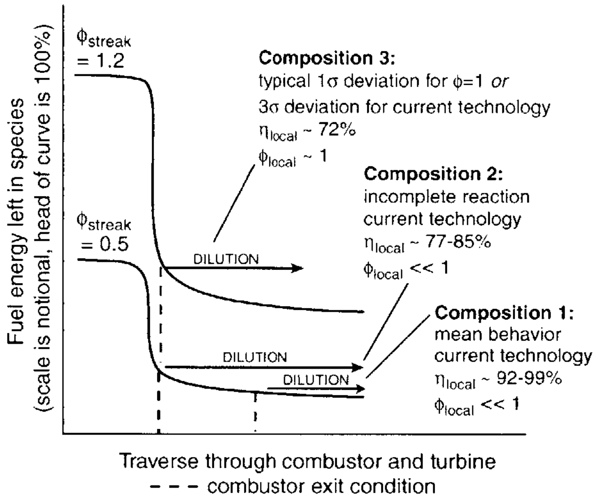

Figure 2.1: Representative Current and Future Turbine Flow Compositions 1-3

Since the total available energy defines the maximum local temperature rise, the non-dimensional heat release potential, H^*, as summarized in Table 2.2 can be determined for each case. More details associated with the development of compositions 1-3 can be found in Reference [39].

Table 2.2: Composition Number and H^* Summary

Composition	H^*
1	0.05-0.05
2	0.06-0.11
3	0.18-0.35

A fuel-lean mixture, Composition 1, with $\phi_{streak}=0.5$ and $\eta_{local} \sim 92\text{-}99\%$, is chosen to represent the performance of a well-mixed, current era combustor of high efficiency. The range of efficiency reflects the influence of different combustor exit temperatures and pressures on equilibrium concentrations of energetic species. Composition 2 reflects an increase in emissions for the same current era combustor, resulting in $\eta_{local} \sim 77\text{-}85\%$. This decline in efficiency could, for example, be due to lack of adequate residence time for complete combustion. A fuel-rich mixture, Composition 3, with $\phi_{streak}=1.2$ and $\eta_{local} \sim 72\%$, represents the additional dimension of unmixedness. This case represents, for example, the 1σ deviation along the upper tail of a future stoichiometric combustor with a $S=\sigma/\phi=0.2$ exit distribution, a level typical of current combustor unmixedness, or a 3σ deviation along the upper tail of the Composition 2, current era combustor.

2.7 Characteristic Time Method: Damköhler Number and ΔT_t Scoping Tools

The previous section presented a range of estimates for energetic emissions entering the turbine for current and future engines. In the high-pressure turbine (HPT), oxidative chemical interactions may occur among primary combustion products, trace species (e.g. CO, H_2, NO_y, SO_x, HO_x, and O) and film-cooling flows [40,45]. These processes are quenched by local temperature changes through the HPT. Thus, whether these species react within the turbine is a function of the temperature and pressure through the turbine, local flow effects, and the constituency of such emissions.

In this section, bounds on the magnitude of energy release that can occur as a result combustor emissions are predicted. The adiabatic flame temperature is a thermodynamic limit for the magnitude of heat released and subsequent temperature rise. The potential heat release, ΔT_t, and Da, are calculated over a range of engine operating conditions. A subset of temperatures and pressures, between 1500-2100 K and 10-25 atm, is taken as representative of the nozzle guide vane (NGV) flow through a current era turbine.

Figure 2.2 shows results for ΔT_t calculated in this manner for the representative turbine conditions described in Figure 2.1.

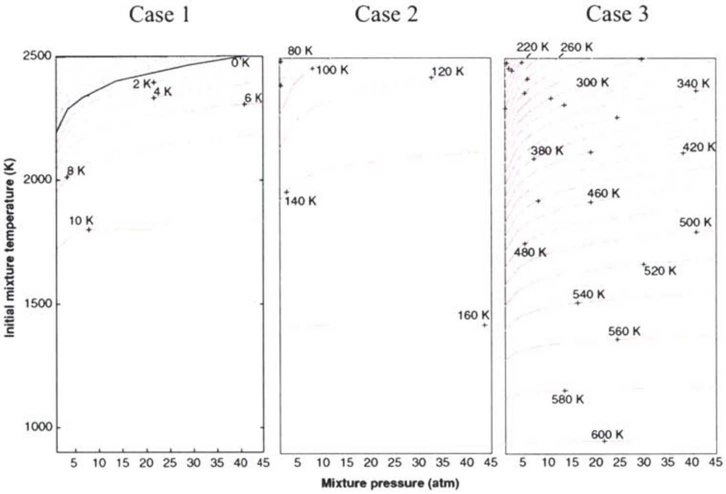

Figure 2.2: Potential Local Temperature Rise for Compositional Cases 1-3[4]

The primary driver of ΔT_t is the total available energy of local energetic emissions. Compositions marked by higher total energetic emissions have a greater potential for larger ΔT_t. There is a generally greater dependence on local temperature than pressure, but pressure dependencies are important below approximately 5-8 atmospheres. The local temperature rise, ΔT_t, is greater for low initial temperature and high-pressure conditions.

---

[4] Grayed area indicates thermodynamically incompatible T, P, X combinations.

Composition 3, $H^{*}\sim0.35$, exemplifies an upper bound for a high equivalence ratio, future engine, of limited efficiency and unmixedness typical of current era combustors. Over a range of temperatures and pressures characteristic of the NGV, the local temperature rise can exceed 500 K. This is much higher than the approximately 10 K rise of Composition 1 ($H^{*}\sim0.0045$) for the same temperature and pressure space, which exemplifies a current, highly-efficient, well-mixed engine. Increasing unmixedness for current engines, as shown in Composition 2 ($H^{*}\sim0.11$), increases the potential local temperature rise to 150 K. Generally, a combustor efficiency of less than 98.5% is required to realize a temperature rise greater than 50 K for Composition 3, whereas an efficiency of less than 95% is required for Composition 1. Such an analysis also indicates that near-wall surface reactions or freestream oxidization may be taking place in current engines, but the total temperature rise associated with the energetic species exiting the combustor may not yet be significant in terms of durability.

In Figure 2.3, a Damköhler number ($\tau_{flow}=0.5$ ms, typical of a turbine blade row) is shown for the mixture compositions outlined in Figure 2.1. The results are overlapped upon the ΔT_t results of Figure 2.1. Moving from the lower left to the upper right of each temperature and pressure space, which is the current direction of technology development, conditions for secondary combustion become more favorable because temperatures, pressures, and concentrations are increasing. Since temperatures are highest at high power conditions, take-off, climb-out, or other accelerations are the most probable time for oxidation and heat release within the turbine. For a current era engine, the Damköhler number is 10-500 for ignition and 1-25 for reaction for all cases. For situations in which residence times would be much longer, i.e. recirculation zones, the temperature and pressure space would consist of high Da for the well-mixed, adiabatic limit.

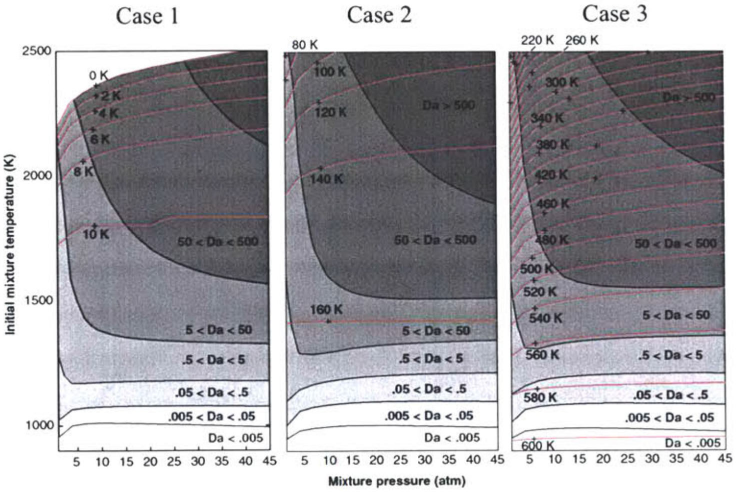

Figure 2.3: ΔT_t and Da Comparing Ignition and Blade Row Traverse Times For Representative Flow Compositional Cases 1-3

Given the magnitude of Da, secondary reactions with cooling air can occur even in current era turbines. The potential for secondary reactions decreases through the turbine due to decreasing temperatures and pressures. Following a streamline through the NGV, Da for reaction decreases to order one, indicating that the HPT would be the section of most concern for heat release impacts. Furthermore, the magnitude of Da indicates that reactions, if begun in the NGV, may lead to the highest temperatures towards the end of the NGV or beginning of the HPT. For Composition 3, which represents an unmixed streak emitted into the turbine of a stoichiometric engine, realizing the full extent of reaction can impact durability since maximum temperature increases may exceed 500 K.

2.8 Chapter Summary

This chapter introduced the important physical parameters used to describe the changes in surface heat flux due to secondary reactions. These physical parameters, as well as the range for which they may exist in a modern engine, are summarized in Table 2.3. The table also indicates what other non-dimensional groups influence the primary parameters.

Table 2.3: Summary of Important Physical Parameters

Parameter	f	Description	Range in Modern Engine
Da	$f(M, \phi, T_{t\infty})$	Characteristic flow to chemical time scale	0->10,000[5]
H^*	$f(\phi, T_{t\infty})$	Freestream heat release potential	0.0-0.5
B, I		Coolant to freestream blowing parameters	0.1-4, 0.005-16
Q_s	$f(M, Re, Pr, St, geometry^6)$	Scaled heat flux ratio	0.0-1.0

Chapters 3 and 4 describe experiments performed over the conditions of Table 2.3, and it will be shown that these are a complete set of parameters to describe the phenomenon. This will be further corroborated by the numerical studies of Chapter 5. Finally, in Chapter 6, these parameters will be put to use in a series of simplified design and analysis problems.

---

[5] In certain portions of the turbine flow path the streamlines may become nearly circumferential leading to very large flow residence times. Although this flow certainly does not remain in the turbine indefinitely long, the number of chemical completion times during such a traverse may be exceptionally large.

[6] Geometry refers to the film-cooling geometry, such as spacing of the cooling holes (x/D, z/D), row-to-row stagger (z/D), and injection angle relative to the surface (α).

Chapter 3

Experimental Investigation

To simulate conditions in which near-wall reactions may occur, an experiment to measure surface heat flux was devised and implemented using the MIT shock tunnel facility. This experiment was capable or probing a wide range of Damköhler numbers, blowing parameters, and fuel concentrations at the freestream conditions existing in combustor exit and turbine environments. The experiment provided the first measurements of the augmentations in surface heat flux that may arise due to the interaction of a fuel-rich combustor exit flow with a film-cooling layer. The purpose of this chapter is to review the experimental apparatus, time-scales associated with shock tunnel transient testing, and reactive heat flux measurements.

3.1 Shock Tube Experiment and Facility Overview

To achieve freestream conditions associated with combustor exit and turbine flow fields, a shock tube testing facility was employed. A shock tube provides a flexible, cost-effective means for exploring a wide range of flow-chemistry interactions at the high temperatures and pressures associated with modern engines. The gas composition and test gas pressures within the tube are easily regulated to yield different freestream stagnation temperatures and pressures. A film-cooled flat plate served as a simulated turbine component on which to make heat flux measurements. To make such measurements, sufficient time must be allowed for quasi-steady flow to develop over the flat plate during the relatively short test duration. However, the short run times associated with shock tube testing are advantageous because the test specimen is exposed to high temperature flow for only a fraction of a second. This reduces the cost and complexity of the test article since it does not have to withstand elevated conditions over an extended period of time.

The shock tube used in this experiment consists of a 7.3 m driven section and 8.4 m driver, both constructed from 30 cm diameter stainless steel pipe. Freestream pressure was measured by four pressure transducers located in the driven section, which also served to measure shock speed and infer total temperature. Argon was used as the test gas because of its high specific heat ratio, allowing for test temperatures up to 2800 K. Furthermore, it is inert and will not react with the seeded fuel prior to the test, so the only reactions taking place are those between the air film-coolant and freestream fuel. A choked nozzle located downstream of the test section served as a throttle to control freestream Mach number over the test plate. By using choked nozzles of different exit area, the Mach number could be varied from 0.15-0.3. Similar transient techniques have been used by others to make non-reactive heat transfer measurements [30]. A brief summary of shock tube operation and wave dynamics can be found in Appendix B, with many more details about the MIT shock tube facility found in Reference [32].

3.2 Test Time Considerations

Calculations were performed to ensure that there would be ample time for the starting of flow through the test section and boundary layer development over the flat plate. Table 3.1 summarizes the duration of the experimental test time, flow speed, and flow time over the range of temperatures studied, as calculated using the methods of Reference [32] and summarized in Appendix B.

Table 3.1: Test Time Summary, Ethylene Fuel, Φ=1.0, P=6 atm.

T_t (K)	τ_{test} (ms)	u_{flow} (m/s)	τ_{flow} (ms, x/D=10)	$C_2H_4\tau_{chem95}$ (ms)	Da ($\tau_{flow}/\tau_{chem95}$)
1000	40	176	0.14	30	0.005
1900	22	243	0.11	0.08	1.4
2800	8	295	0.086	3e-3	28.7

A useful parameter to relate the flow and chemical time scales is the Damköhler number, which was discussed in detail in Section 2.3:

$$Da = \frac{\tau_{flow}}{\tau_{chem}} = \frac{L/u_\infty}{\tau_{chem}} = \frac{10D/M\sqrt{\gamma RT_\infty}}{\tau_{chem}} \qquad 3.1$$

As shown in Equation 3.1, the flow time, τ_{flow}, is taken as the time for the freestream flow to convect over 10 cooling hole diameters, 10D. This value was chosen as a representative spacing between axial rows of film-cooling holes on turbine airfoils, and later it is shown that this also corresponds to the approximate location of the maximum augmentation in surface heat flux due to local reactions.

3.2.1 Freestream Fuel Selection

The primary objective of the experiment was to probe a range of Damköhler numbers representative of conditions in current and future gas turbines, as discussed in Section 2.6. Ethylene, C_2H_4, was chosen as the freestream fuel because of its relatively short ignition time and ability to satisfy the shock matching conditions [1, 32, 39, 61].[7] Chemical ignition and completion times for ethylene were calculated using the methods outlined in Section 2.6 and 2.7 over the range of temperatures used in the experiment, $T_{t\infty}$=800-2800 K. Table 3.1 also presents the chemical time to 95% completion (used in the denominator of the Damköhler number). The ratio of test time to chemical time indicates that the chemical times are much shorter than the available test time, meaning that although the shock tunnel tests are short in duration, they are sufficiently long for full heat release of the fuel to take place over all desired test conditions. Damköhler numbers that range from 0-30 can be examined. In the experiment, the Damköhler number was controlled through varying the freestream temperature. In the numerator of Da, T_∞, sets the freestream velocity since the test section Mach number is fixed. In the denominator, for constant pressure and Φ=1.0, the chemical time is only a function of temperature.

---

[7] Hydrogen was also explored as a possible freestream fuel because of its very rapid ignition and completion chemical time scales. However, hydrogen's high gas constant makes it difficult to satisfy the required shock tunnel operating conditions when amounts corresponding to the required H^* range are seeded into the driven section.

Ethylene fuel content in the argon freestream was set to span a range of levels representative of energetic chemical emissions typical of modern and future combustors, as was discussed in Section 2.6. In that section it was shown that a $H^*=0.15$ case is representative of a modern combustor operating at $\Phi=0.5$ with 85% efficiency, or a future combustor operating at $\Phi=1.0$ with 100% efficiency. The $H^*=0.3$ case represents either a 1 sigma deviation in mixedness from a stoichiometric combustor or a 3 sigma deviation from a modern combustor with $\Phi=0.5$.

As presented in Section 2.3, a more universal unit for fuel level, rather than equivalent CO-equivalent concentration, is the ratio of the potential increase in enthalpy due to the reaction relative to the freestream total enthalpy. Since C_p for argon is a constant, this is expressed approximately in terms of total temperature, as shown in Equation 3.2.

$$H^* = \frac{\Delta h_t}{h_{t\infty}} = \frac{T_{ad} - T_{t\infty}}{T_{t\infty}} \tag{3.2}$$

The range of non-dimensional fuel enthalpy studied in this investigation was 0.005-0.80, which spans the range of combustor operating conditions discussed in Reference [39]. This range spans the three sample cases of combustor exit speciation that were presented in Section 2.6. In the experiments the value of H^* increased with decreasing Damköhler number because the fuel mass fraction of the freestream was kept constant for each case. The results of the reacting flow tests will be shown in the next chapter.

3.3 Test Article Description, Data Acquisition, and Processing

A schematic of the test section (mounted on the driven end of the shock tube) and details of the flat plate test article are shown in Figure 3.1.

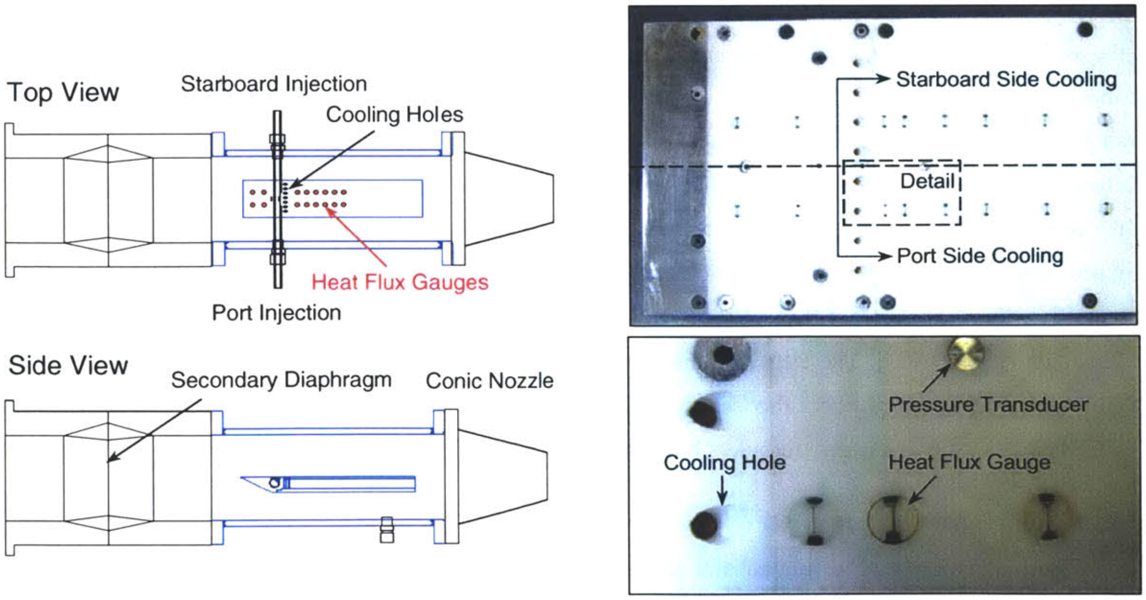

Figure 3.1: Test Section Schematic and Flat Plate Details

3.3.1 Flat Plate Test Article and Heat Flux Gauges

The flat plate used in this experiment is separated into two regions, such that two sets of round 35° holes can be supplied with different film-cooling gases. One side of cooling holes was supplied with nitrogen and the opposite side supplied with air. Four cooling holes were located on each side, with a diameter of 0.25 cm and a lateral spacing of 0.76 cm. The test plate was constructed from aluminum and is 25.4 cm long by 7.62 cm wide. A 0.48 cm thick sheet of MACOR ceramic was used as the plate surface due to its low thermal conductivity, k, (1.46 W/m K, versus 237 W/m K for pure aluminum) giving a high surface temperature rise (~50-100 K) during the 10 ms test duration. Two Kulite XT-90 pressure transducers were located on the forward and aft portions of the test plate to measure freestream pressure and to determine if any pressure gradient existed over the extent of the plate. Mechanical drawings of the test plate, test housing, associated coolant feeds, and wiring diagrams can be found in Appendix C.

Eight thin-film heat flux gauges were located upstream and downstream on each side of one of the film-cooling holes, with x/D locations ranging from –10 to 25 (2 and 6 gauges located upstream and downstream of the film-cooling holes, respectively), as shown in Figure 3.1. The gauges measure the surface wall temperature, which was integrated over time to give surface heat flux. The heat flux gauges were constructed from 0.05 cm MACOR cylinders, with a thin resistive element located on the top of each gauge. Each gauge, along with its signal amplifier, was calibrated in an oil bath after being mounted onto the test plate. This calibration produced a voltage versus temperature relationship, with the temperature known to better than 0.1 K. The passive thin film heat flux gauges were developed specifically for this study, and a detailed account of their construction, installation, calibration, and use is given in Appendix D. The basics of thin-film resistive gauge theory and measurement techniques, and the procedure used to convert the wall temperature versus time data to surface heat flux is outlined in Appendix E.

The freestream, composed of the argon-ethylene mixture, provided a fuel-rich flow that reacted with the air side film-coolant, while simultaneously flowing passively over the inert nitrogen cooled side. This allowed for a same test, side-by-side assessment of the impact of local reaction. In other words, during a single shock tube experiment, differences in heat flux augmentation from near-wall reactions could be compared to a non-reactive scenario at the same freestream flow conditions. The Reynolds number range at the cooling hole location varied from $Re=1.3\times10^5$ to 2.4×10^5 depending on test condition. Care was taken when mounting the gauges onto the test plate to ensure that the gauge surface and the surface of the plate were to within 0.013 cm which satisfies the criterion for sandgrain aerodynamic smoothness at these Reynolds numbers [31]. The transition distance to a turbulent boundary layer was on the order of 1 cm, putting it close to the first heat flux sensor. A thin piece of tape located on the leading edge was used as a boundary layer trip to ensure a turbulent boundary layer over the entire plate.

3.3.2 Film-Coolant Supply System

The blowing system for the air and nitrogen film-coolant was designed so that each side of the test plate could be supplied with mass blowing ratios from near zero to around 3. The film-coolant flow was initiated prior to test, but allowing enough time for a well-developed film-cooling flow to be established.

Once the test is initiated some backflow into the cooling supply plenum occurs. Care was taken to size this plenum so that several flow through times of the coolant gas could occur prior to the actual test window. Kulite XT-90 pressure transducers were located in each of the cooling plenums to measure chamber pressure. A hot-wire anemometer study ensured that the supply plenum was providing uniform blowing through each set of four cooling holes. Also, for the blowing ratios investigated, the lateral cooling hole spacings and heat flux gauges were located such that there would be no cross-stream interaction between the starboard side film-cooling jets and the port side heat flux gauges, or vice versa. This was also corroborated using the hot-wire anemometer study.

3.3.3 Fuel Mixing System

To simulate the conditions exiting the combustor and entering the turbine, the concentration of fuel in the freestream must be well known for the non-dimensionalization of Equation 3.2 to be accurate. To accomplish this, a partial pressure based argon-ethylene mixing tank was set-up so that the mass fraction of each gas was known. The driven section was first evacuated and then filled with argon so that no air would contaminate the mixture. Next the fuel mixture was introduced into the driven section. Any remaining argon within the driven section was taken into account prior to the calculation of the final mass fractions of fuel and argon in the driven section. Using this technique freestream fuel levels spanning a range of H^* could be established to an accuracy of 5%.

3.3.4 Data Acquisition System

The wall temperature and pressure data were acquired at 100 kHz using an ADTEK data acquisition system. Wall temperature data from each individual gauge were processed using the ACQ model. ACQ is an electrical circuit analogy model that was used in the integration of temperature versus time to heat flux. More information on the model can be found in References [53, 63] and in Appendix E.

3.4 Sample Results and Flat Plate Heat Transfer Physics

A sample of driven section pressure traces versus time and a pressure trace just upstream of the test plate are shown in Figure 3.2a for a freestream temperature of 2000 K and pressure of 6 atmospheres. From the pressure traces, the location of the shock wave as it moves through the tube can be seen on both the incident and reflected passes. The vertical lines indicate the region taken as quasi-steady, based on the uniformity of the pressure traces. For this non-reactive test, the region of relevance is approximately 9 ms in duration.

The second plot in Figure 3.2 shows the wall temperature response of the two heat flux gauges located laterally next to each other at 3.2 inches, x/D=32, downstream of the leading edge. The plot indicates a rapid increase in temperature over the start-up time, and then a gradual increase in temperature during the actual test window. This wall temperature versus time trace was then integrated to give the wall heat flux, which is shown in the third plot to be around $5.0\text{x}10^4$ W/m^2 during the test window. A flat plate turbulent boundary layer correlation was used to predict the level of expected heat flux to the surface for these steady-state conditions and was found to be 5.4×10^4 W/m^2, which agrees to within roughly 8% of the experimental data. Such agreement is typical for each gauge measurement of the un-cooled tests, and is shown further in the next chapter.

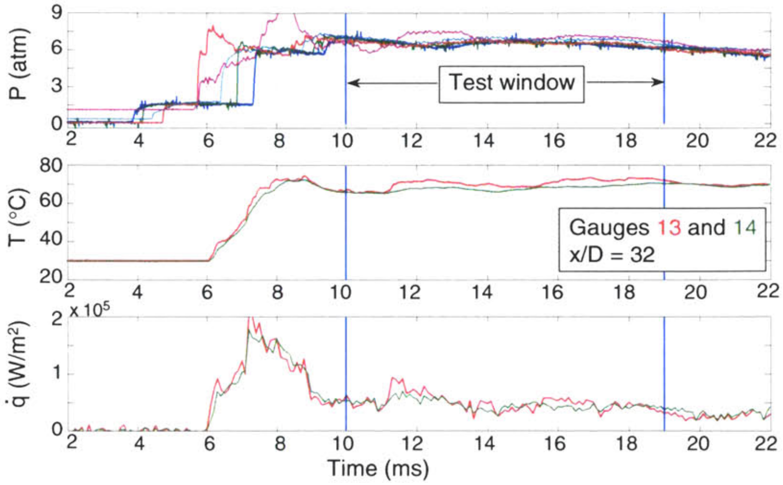

Figure 3.2 (a,b,c): Sample Pressure, Wall Temperature, and Wall Heat Flux Traces, $T_{t\infty}$=2000 K

To understand why the temperature and heat flux versus time traces look the way they do in Figure 3.2b and c, a transient heat transfer model, which takes into account the start-up process, is illustrative. At the outset of the test a shear flow develops over the flat plat. Because no initial boundary layer is present, the high heat load to the plate causes the wall temperature to rise rapidly. Shortly thereafter a boundary layer begins to develop, which buffers the heat load to the wall. Depending on the magnitude of the initial heat flux and the heat flux over the quasi-steady region of the test, the wall temperature may continue to rise, remain level, or even decrease depending on the balance of convective and conductive heat transfer over and into the wall, respectively.

The temperature distribution within a semi-infinite solid for a step change in surface heat flux is given by Equation 3.3, where k is the thermal conductivity, κ is the thermal diffusivity, and ζ is the depth into the surface to be investigated [31].

$$\Delta T = \frac{2\dot{q}}{k}\left[\left(\frac{\kappa t}{\pi}\right)^{0.5} \exp\left(\frac{-\varsigma^2}{4t\kappa}\right) - \frac{\varsigma}{2}\operatorname{erfc}\left(\frac{\varsigma}{2\sqrt{\kappa t}}\right)\right] \qquad 3.3$$

Figure 3.3 provides an example of an initial heat load of 2×10^6 W/m^2 (typical of the freestream temperatures relevant to this experiment) to model the shear start-up flow and then considers three different levels of heat load for a fully developed turbulent boundary layer at the surface of the plate (ζ=0.0).

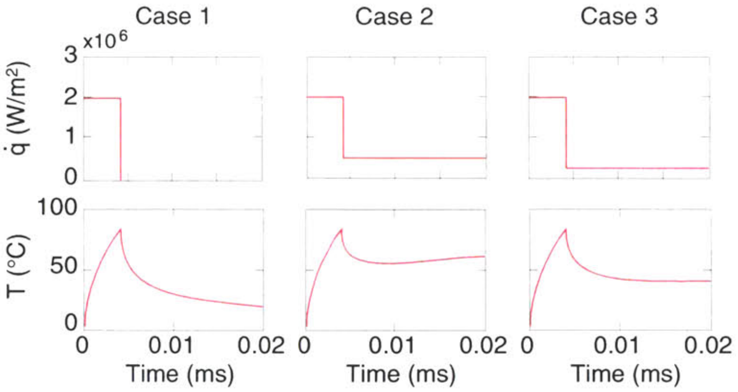

Figure 3.3: Wall Temperature Distributions (ζ=0.0) for 3 Wall Heat Flux Distributions

In case 1, the initial heat load is applied for 4 ms and removed with no subsequent heat flux, modeling the initial start-up time seen in Figure 3.2. The temperature response is an initial spike and then decay since no further heat load is being applied. In case 2, the steady-state heat load is large enough to make the wall temperature continue to climb after the initial shear layer spike. The surface temperature rises because the heat load is larger than the wall can carry away through its depth. In case 3, it is seen that if the proper steady-state heat load is applied, the wall temperature will spike and then remain effectively constant over the duration of the test window. There is a balance between the convective heat load over the top of the plate and conduction of that heat through the depth of the plate. Comparing case 3 with Figure 3.2c, the physical interpretation of the relationship between the temperature response and integrated heat flux is elucidated. To appropriately include these effects, the entire temperature versus time history is used to integrate the wall heat flux during the quasi-steady window. Further discussion of the methods used to convert wall temperature versus time to heat flux are found in Reference [53] and in Appendix E.

3.5 Chapter Summary

The purpose of this chapter was to describe the experimental apparatus employed to make measurements of changes in surface heat flux due to the interaction of a fuel-rich freestream with a film-cooling layer. Various aspects of design and assembly of the experimental hardware and data acquisition systems are included. The chapter also discussed a simplified physical model which explains the behavior of the wall temperature and heat flux versus time traces that were achieved on the flat plate test specimen. In Chapter 4, the results of a series of tests to measure augmented heat fluxes due to local reactions will be shown and the data will be appropriately scaled for comparison to other turbine conditions.

Chapter 4

Experimental Results, Analysis, and Scaling

This chapter begins by establishing the validity of the transient flat plate heat flux measurements through un-cooled and cooled surface experiments. The results and analyses of reacting freestream cases then form the focus of the chapter. The chapter concludes with a presentation of methods to scale the experimental data for comparison with other turbine or experimental conditions.

4.1 Experimental Test Matrix

To proceed toward an assessment of local reactions and to build confidence in the transient heat flux data, the facility was first benchmarked against correlations and data available in the literature, References [1, 16, 17, 22, 41]. Table 4.1 summarizes the tests completed to assess the performance of the facility, including flat plate heat transfer studies with and without cooling, as well as those conducted with a reactive freestream. Also shown in Table 4.1 are the range of blowing ratios studied in the film-cooled, non-reactive, and reactive test series. The final column in Table 4.1 show the span of fuel levels examined in terms of H^*.

Table 4.1: Summary of Experimental Test Cases

Test	P (atm.)	$T_{t\infty}$ (K)	B (port)	B (starboard)	H^*
1. Un-Cooled Flat Plate Tests					
1.1	5-7	800 - 2800	N/A	N/A	N/A
2. Film-cooled, Non-Reactive Tests					
2.1	6	1000 - 2800	1.0 (air)	0.0	N/A
2.2	6	1000 - 2800	0.0	1.0 (air)	N/A
2.3	6	1000 - 2800	0.5-2.0 (air)	0.5-2.0 (air)	N/A
2.4	6	1000 - 2800	0.5-2.0 (air)	0.5-2.0 (N_2)	N/A
3. Reacting Freestream Flow Tests					
3.1	6	1000 - 2800	0.5 (air)	0.5 (N_2)	0.005-0.95
3.2	6	1000 - 2800	1.0 (air)	1.0 (N_2)	0.01-0.80
3.3	6	1000 - 2800	2.0 (air)	2.0 (N_2)	0.01-0.80
3.4	6	1500, 2800	1.0 (N_2)	1.0 (air)	0.1-0.80

A complete summary of all test cases, by run number, is contained in Appendix F.

4.2 Un-Cooled Flat Plate Heat Transfer Results

To benchmark the experiment, a series of un-cooled flat plate tests were conducted. The purpose was to ascertain how well the measured heat flux agreed with correlations for turbulent flat plate heat transfer. The turbulent flat plate heat flux correlation given in Reference [31] is:

$$\dot{q} = h(T_\infty - T_o) = \rho C_p \mathrm{St} M \sqrt{\gamma R T_\infty}(T_\infty - T_o) \qquad 4.1$$

with the Stanton number distribution given by:

$$\mathrm{St} = \frac{0.0287\,\mathrm{Re}_x^{-0.2}}{0.169\,\mathrm{Re}_x^{-0.1}(13.2\,\mathrm{Pr} - 10.16) + 0.9} \qquad 4.2$$

Equation 4.2 is valid for a turbulent boundary layer in the case of a constant free-stream velocity (no pressure gradient) and constant surface temperature. Under such conditions Equation 4.2 has shown agreement with data to within 5% over a range of Re_x from 2e4-4.0e6 [31].

Figure 4.1 presents a summary of a representative set of experimental cases over the temperature range investigated (800-2800 K), with the symbols representing the average heat flux taken at each gauge location over the quasi-steady portion of the test. The solid line shows the predicted turbulent heat flux on a flat plate, given by equations 4.1 and 4.2. The plot indicates that the overall heat flux levels agree to within 10-15 percent over the entire range of tests.

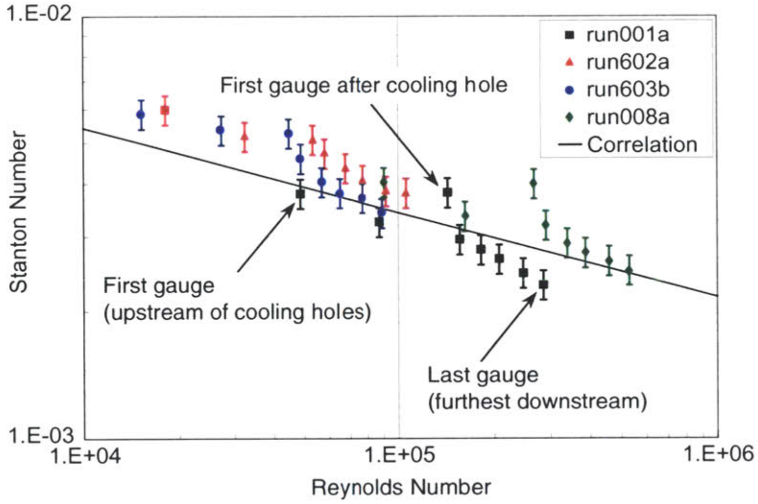

Figure 4.1: Flat Plate Heat Transfer Results

The vertical uncertainty bars shown at each heat flux gauge location represent the peak fluctuations within the steady-state window, as shown in the bottom plot of Figure 3.2. These fluctuations are on the order of 10 percent of the time-averaged value. Side-to-side agreement between lateral heat flux gauges at the same x/D location was on the order of 10 percent. For each test, the points which show the greatest deviation are located just aft of the cooling holes. During these tests a piece of tape was placed over the cooling holes to prevent back-flow and reduce flow disturbances due to the cooling holes. This may explain why these points consistently show the largest deviation. Overall these data show good agreement both in trend and magnitude with equation 4.2. A complete listing of all un-cooled flat plate heat flux tests is given in Appendix F.

4.3 Non-Reactive Film-Cooling Experiments

This section presents results on surface heat flux measurements using film-cooling on the flat plate but without the presence of reaction. These tests served to benchmark the experimental performance over a range of cooling conditions relevant to modern turbine cooling strategies.

4.3.1 Blowing and Momentum Parameter Selection

In these film-cooling experiments where the temperature of the freestream is varied and that of the coolant gas remains constant, either the mass or momentum flux ratio can be controlled independently. Since the objective of this study was to measure changes in surface heat flux, the mass blowing ratio was specified because the convective surface heat flux scales with the quantity ρu. Each of the mass blowing ratios shown in Table 4.1 correspond to a momentum flux ratio, based on the freestream temperature of the test. The range of I can be calculated from equation 2.3, which shows that $I=B^2/DR$, and approximately simplifies to $I=B^2*(R_c/R_\infty)*TR$, where R is the gas constant and $TR=T_c/T_\infty$. The range of momentum blowing ratios studied in this experiment was 0.025-1.8, spanning over the transition from attached to lifted jets, with separation of the jet from the surface occurring at about I=0.7.

One goal of the experiments presented in this chapter was to study the differences in surface heat flux augmentation due to lifted versus attached jets. The mass blowing ratio cases of B=0.5 correspond to an attached jet and a mass blowing ratio of B=2.0 corresponds to a jet that is lifted off the surface. The mass blowing ratio of 1.0 corresponds to a range of momentum blowing ratios that produces attached jets (I=0.375-0.11). However, it must be noted that this is not always the case for mass blowing ratios of unity. In realistic turbine flows, B=1.0 may correspond to either lifted or attached jets, depending on the ratio of the coolant to freestream temperatures. Even for the blowing ratio of 2.0, at the highest freestream temperatures tested, the jet begins to border on the transition from a lifted jet back to an attached one. Results for higher jet momentum could not be examined due to the limitations on the fill pressures associated with the film-coolant supply system, however, results for higher jet momentum ratios are examined numerically in Chapter 5.

4.3.2 Validation Experiments

Two objectives were accomplished in the film-cooling validation tests. The first was to ensure that the film-cooled heat transfer results on each side of the test plate were in agreement with each other as different cooling gases were used. The second objective was to compare the measured heat transfer results from the experiment to literature film effectiveness predictions (experimental and computational) and determine how well the transient experiment captured the details associated with film-cooled surface flows.

Film-cooled flat plate experiments were first conducted to ensure side-to-side agreement of the air and nitrogen cooling gases over a range of mass blowing parameters from 0.5-2.0. Several studies, over a range of blowing ratios while switching the sides that the air and nitrogen gases were injected from, were performed to ensure no side-to-side bias existed. To compensate for the use of different film-cooling gases, corrections to the film-cooling supply pressures were made due to the difference in molecular weight between air and nitrogen. With these corrections, amounting to about 2% in supply pressure, it was found that the side-to-side agreement of lateral heat flux gauges while using different cooling gases was better than 5%, or on the order of the side-to-side agreement when the same gases were used.

A comparison of experimental film-cooled results with the data of References [22, 64, 65] was completed for B=0.5, 1.0, and 2.0 over a range of freestream temperatures. An example is shown in Figure 4.2 for one side having no blowing, B=0, and the other side having a mass blowing ratio of B=1.0. This plot shows the measured heat flux to the wall versus x/D position.

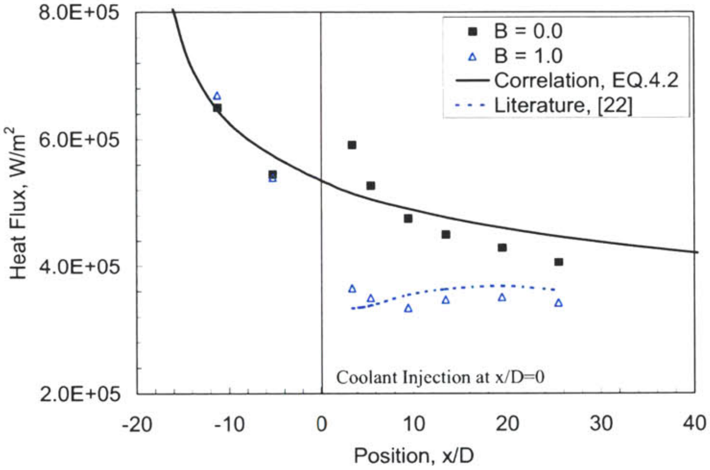

Figure 4.2: Sample of Film-Cooling Test Results Comparing B=0 and B=1.0, $T_{t\infty}$=1900K and T_c=300K.

The side with a blowing parameter of 1.0 shows a 10-35 percent reduction in surface heat flux, depending on downstream distance from the cooling holes, which agrees well with film effectiveness data at this blowing ratio, as will be discussed in Section 4.3.3. Also the two side-by-side gauges, located upstream of the cooling holes, are consistent with each other to about 3%, and the un-cooled results agree with the empirical correlation of Equation 4.1 to within about 10%. This level of agreement was consistent with all film-cooling experiments performed.

The utility of the differential experiment is evident for this type of comparison. Instead of conducting two separate experiments at identical freestream pressure and temperature between the two runs, a direct assessment of the influence of different blowing parameters is available in a single test. In the cases with a reacting freestream, which will be discussed in the next section, both sides will be operated at the same coolant conditions, but with one of the gases being the inert nitrogen and the other side fed by air. In a single test, a back-to-back comparison between reactive and non-reactive scenarios is possible.

4.3.3 Comparison to Literature Results

To assess these results, literature data for film-cooling effectiveness were used to provide an approximate comparison. To arrive at an estimate, adiabatic film-cooling effectiveness versus x/D downstream distance was used for each of the mass blowing parameters tested. The adiabatic film-cooling effectiveness is defined as:

$$\eta_{ad} = \frac{T_\infty - T_f}{T_\infty - T_c} \qquad 4.3$$

The dashed line in Figure 4.2 represents the expected surface heat flux reduction from film-cooling as applied to the experimental data from the side with no cooling. This is done by multiplying the un-cooled side by $(1-\eta_{ad})$ to arrive at an estimate for the predicted change due to film-cooling.

Over the range of blowing parameters investigated, the performance of the film-cooled side agreed with the representative literature effectiveness data to about 5-30 percent. The differences in film effectiveness behavior between the attached and lifted jets were captured in magnitude and trend in the experiments conducted from B=0.5-2.0. It should be noted that the data taken from the literature references are not an exact match for all cases tested. The literature data is for air injection into an air (versus Argon) freestream and the Reynolds numbers and freestream and coolant temperatures are not identical. However, the agreement between literature cases that were close in blowing parameter and freestream conditions were quite good. An exact comparison to the same freestream and coolant conditions will be performed in Chapter 5 using the numerical tool (benchmarked against exact literature conditions), which can simulate the expected adiabatic film effectiveness for the experimental test cases. Using numerical simulations of the shock tube tests, the computational and experimental results for a cooled flat plate agreed to within about 10-20% of each other.

4.4 Reactive Flow Tests

This section is concerned with the primary goal of the experiment: measuring the change in surface heat flux due to local reaction over a range of relevant parameters. A series of tests using ethylene fuel (corresponding to H^*=0.005-0.8) seeded in the argon freestream were conducted. These fuel contents were chosen as a representative range of the levels of chemical emissions due to combustor unmixedness as was discussed in Section 2.6 and in Reference [39]. Blowing ratios of 0.5-2.0 and freestream temperatures of 1000-2800K were examined, corresponding to a Damköhler number range of 0-30. The complete series of reactive flow tests conducted is summarized in Table 4.1 and in further detail in Appendix F. Figure 4.3 shows a sample of the influence of local reaction on measured surface heat flux for a Damköhler number of 25. Air was injected on one side and nitrogen on the other side, both at a blowing ratio of 1.0, corresponding to a momentum blowing ratio of I=0.25. The freestream temperature was 2200K with a non-dimensional fuel heat release potential of H^*=0.3.

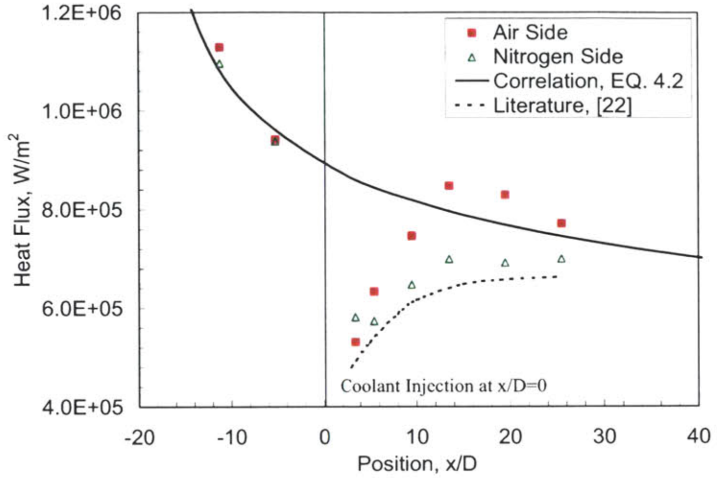

Figure 4.3: Augmented Heat Flux Due to Local Reaction, B=1.0, H^*=0.3, Da=25

Examining Figure 4.3, differences of up to 25 percent exist between the reactive and inert sides downstream of the film-cooling holes. The plot indicates that the influence of reaction extends downstream to the last gauge location at x/D=25, and that the magnitude of the augmented heat flux is higher than the un-cooled flat plate empirical results, shown by the solid line. The agreement of the nitrogen cooled side to the literature is within 15 percent and predicted a decrease in surface heat flux, which is shown by the dash lined and computed as described in Section 4.3.3. To ensure that this behavior was attributable to local reactions, the gas injection sides were switched and the experiment repeated with similar results.

The freestream temperature of the shock tube core flow is usually determined from the incident shock speed, which can typically contain uncertainties equivalent to 10-15% in freestream total temperature. A more accurate way to ascertain the freestream temperature is by aligning the heat flux measurements from the 4 gauges upstream of the film-cooling holes with the empirical correlation and then determining what the necessary driving temperature must have been to achieve this level of heat flux. Thus, to decrease the uncertainty in estimating freestream temperature, the solid line showing the empirical correlation from Equation 4.1 has been aligned with the gauges upstream of the film-cooling holes in Figure 4.3. This method is widely used when making shock tube heat transfer measurements as outlined in Reference [30]. Such a method was employed for the cooled and reactive flow studies, although it is important to note that this only improves absolute accuracy and has no bearing on the relative differences between the inert and reactive heat flux measurements shown in Figure 4.3. This will be discussed further in Section 4.7, which presents the error and uncertainty analysis.

4.5 Summary of Reacting Flow Results

Tests of the type shown in Figure 4.3 were conducted for mass blowing ratios of 0.5, 1.0 and 2.0 over a range of Damköhler numbers at three different fuel enthalpy levels, high: H^*=0.18-0.8, medium: H^*=0.06-

0.24, and low: H^*=0.005-0.5. For each fuel level tested, the maximum difference in side-to-side heat flux was located at an x/D of around 10-20 for the attached jets, and around 10-15 for the lifted jet cases. In all combinations of H^* and B examined, the change in side-to-side heat flux increased with Damköhler number as shown in Figure 4.4, in this case shown for a blowing ratio of 1.0. At the highest Damköhler numbers tested, the cases with high H^* had the most heat flux augmentation of around 30 percent. Similarly, the medium H^* cases also exhibited the maximum change in side-to-side heat flux at the highest Damköhler numbers, however these levels were on the order of 10-15 percent change. No measurable change in side-to-side heat flux above the experimental uncertainty limit was observed in the low H^* cases. In summary, the largest differences in side-to-side heat flux always occurred at the highest Damköhler number and with highest fuel level.

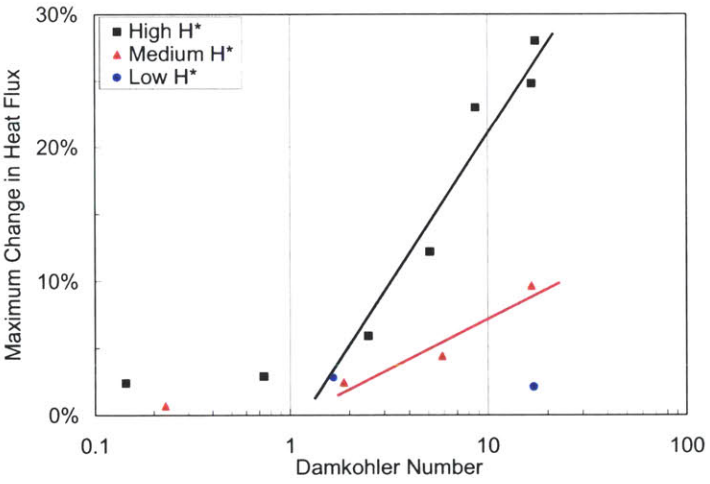

Figure 4.4: Maximum Change in Surface Heat Flux for B=1.0.
High H^*=0.18-0.8, Medium H^*=0.06-0.24, and Low H^*=0.005-0.5

Figure 4.5 compares the differences in the heat flux signatures for an attached jet, B=0.5, and lifted jet, B=2.0, at a Damköhler number of 24. In Figure 4.5, both cases exhibit peak heat flux at an x/D of around 10-15. The augmented heat flux for the attached case decreases slowly after peaking, whereas the lifted jet tends to decrease more rapidly after peaking. This is qualitatively understood because in the attached case more time is required for the heat within the film layer to diffuse and mix to the wall leading to increased heat flux downstream. However, in the lifted case, hot gases are entrained towards the wall as a consequence of vortical re-circulation behind the jet. This allows for increased potential heat release directly behind the film-cooling hole. This mixing with the freestream is also responsible for reducing the temperature of the hot gases, leading to a somewhat lower wall heat flux for the same freestream fuel level. This behavior is further discussed in Chapter 5 where numerical simulations are used to study differences in locally reacting attached and lifted jets. An additional discussion of the mixing processes associated with attached and lifted jets can be found in References [16, 22].

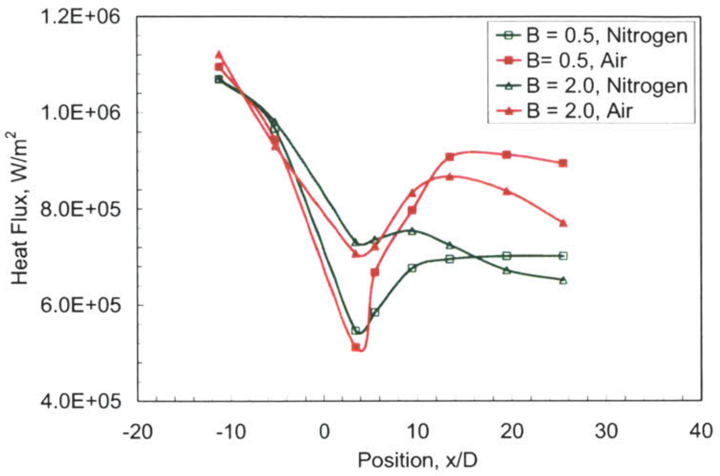

Figure 4.5: Comparison of B=0.5 vs. 2.0, H^*=0.18, Da=24

4.6 Experimental Data Scaling

The goal of this section is to describe the non-dimensional scaling that enables the experimental and numerical data to be used to predict heat loads for other freestream fluid and chemical conditions.

4.6.1 Development of the Scaled Heat Flux Ratio, Q_s

The necessity of scaling arose because, although the data was acquired at similar freestream temperatures, the wall and coolant temperatures were much lower than that of modern turbines. The heat flux scaling is accomplished using the following expression:

$$Q_s = \frac{q_{hot} - q_{cold}}{q_{max} - q_{cold}} = \frac{q_{hot} - q_{cold}}{q(T_{ad}) - q_{cold}} \tag{4.4}$$

The maximum possible heat flux, q_{max}, is that which would be achieved if the local reaction proceeded to the adiabatic flame temperature, T_{ad}, and this temperature was driving the heat flux to the surface. Such a maximum case is evaluated by setting $T_\infty = T_{ad}$ in Equation 4.4. The scaled heat flux, Q_s, represents how much surface heat flux augmentation was achieved for any given test (q_{hot}-q_{cold}) as compared to how much augmentation could possibly have been achieved (q_{max}-q_{cold}). The q_{hot} and q_{cold} heat fluxes were directly evaluated from the measured wall temperature vs. time histories in the experiment as was shown in Figure 3.2. For each test, the adiabatic flame temperature was calculated based on the H^* value at freestream temperature and pressure. Thus if $q_{hot}=q_{cold}$, 0% of the potential augmentation was achieved, and if $q_{hot}=q_{max}$, 100% of the possible augmentation was achieved.

Inherent in the evaluation of $q(T_{max})$ in Equation 4.4 is an estimate for the convective heat transfer coefficient, $h(T_{max})$, since $q_{max}=h_{max}(T_{max}-T_w)$. Evaluation of the convective heat transfer coefficient under reactive conditions is important for setting the limits on the scaling discussed above. Analytical and numerical studies have been performed, and will be discussed in Section 5.3, which indicate that for turbine conditions with reaction the change in heat transfer coefficient is much smaller than the change in driving temperature. For the scaled data sets shown in the next section, the approximation is made that the heat transfer coefficient between reactive and non-reactive cases is constant.

4.6.2 Scaled Data Sets

An example of how the data scaling works is shown in Figure 4.6 for three different blowing ratios, B=0.5, 1.0 and 2.0 for H^{*}~0.35.

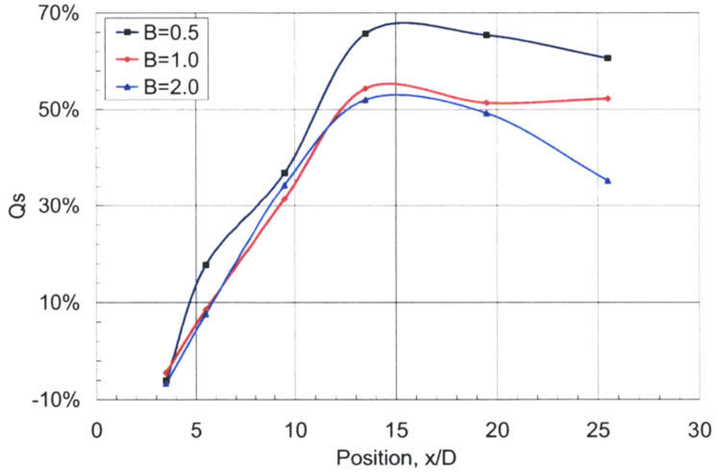

Figure 4.6: Q_s versus x/D for B=0.5, 1.0, and 2.0 for H^{*}=0.35 and $Da_{(x/D=10)}$=24

The first feature to notice about the scaled data is that the Q_s ratio is much higher than the simple algebraic difference between the reactive and inert heat flux measurements (q_{hot}-q_{cold}) that were presented in Figure 4.4, with differences in scaled heat flux as high as 70% for H^{*}=0.35. For these conditions, the heat flux to the surface was between 50-70% of the maximum possible heat flux that the surface could have achieved if the reactions proceeded to the adiabatic flame temperature and if it was this temperature that was responsible for driving the surface heat flux.

This data plot also captures the principal features associated with the differences in blowing ratio that were shown in Figure 4.5. The low blowing ratio case, B=0.5, shows a more distributed nature to the scaled heat flux from x/D=10-25. As the blowing ratio increases, the heat flux tends to peak further upstream, as can be seen for the B=2.0 case. If an alternate Damköhler number definition is employed where the freestream flow time to each x/D location is used in the numerator, the plot would then correspond to a Damköhler number range of 1.5-25, over the x/D range shown. This definition of Damköhler number may be useful if the interest is in the nature of how Q_s varies with x/D distance downstream. Again, Equation 3.1 is a convenient definition of the Damköhler number corresponding to the approximate location of maximum heat flux and typical downstream cooling hole spacings. However, other definitions can certainly be employed depending on the application and desired scaling.

The scaled experimental data is shown in Figure 4.7 for B=0.5 versus Damköhler number. At the highest Da that can be captured in the experiment, the scaled heat flux is on the order of 70-80 percent. Straight lines have been fitted to the data to show the general trend, although the curve is expected to asymptote to 100% as the Damköhler number is further increased.

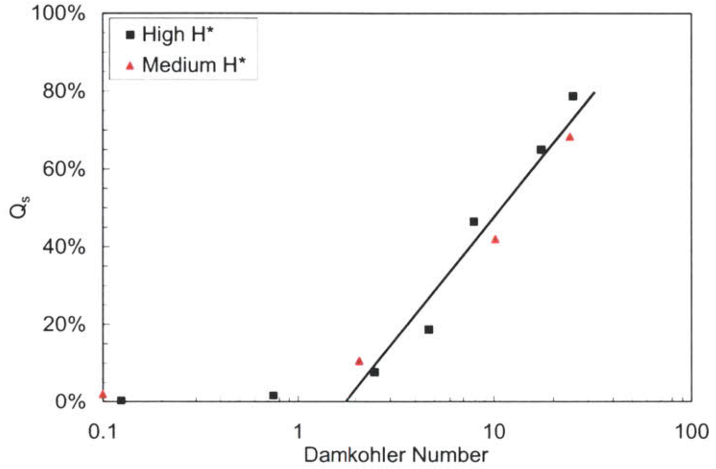

Figure 4.7: Scaled Data Set for B=0.5, H^*=0.05-0.6

At any Damköhler number for the same blowing ratio, the near-wall reactions tended to achieve the same level of scaled heat flux regardless of the non-dimensional heat release potential of the fuel. This behavior is expected and can be understood qualitatively by again examining the scaled heat flux ratio of Equation 4.4. As the level of fuel in the freestream is increased or decreased, the numerator, which is the difference between the hot and cold side heat fluxes, will correspondingly increase or decrease. The maximum adiabatic flame temperature that can be achieved is a function of the fuel level, and hence the maximum attainable heat flux will also vary with fuel level. In this way, when there is little fuel in the freestream, the difference between q_{hot} and q_{cold} may be small, but the corresponding q_{max} that can be achieved, which is based on T_{ad}, will not be large either. However, when the heat fluxes are scaled according to equation 4.4, the heat flux to the surface may have achieved a substantial portion of what is theoretically possible. The collapse of Q_s versus Da for all fuel levels at a given blowing parameter is further corroborated by a series of numerical studies described in Chapter 5.

Another definition of Damköhler number from those described above was also investigated in this work. Instead of simply using the freestream flow time to a x/D location, the definition used a calculated value for the mixed velocity between the freestream and the coolant jet, to arrive at a more representative convective time over the flat plate. Such definition of convective flow time may differ from a definition simply based on the speed of the freestream. The point here is that the numerator of the Damköhler number can be calculated in a number of different ways, which will shift the data to the right or the left on a Q_s versus Da plot, but will not affect the magnitude or shape of the curves.

The effect of mass blowing ratio on the scaled experimental heat transfer data is shown in Figure 4.8 for high H^* (0.18-0.8). Each data point shown in the figure represents the maximum side-to-side change that was shown in Figure 4.4, or the peak points on Figure 4.6 for a range of Da tests.

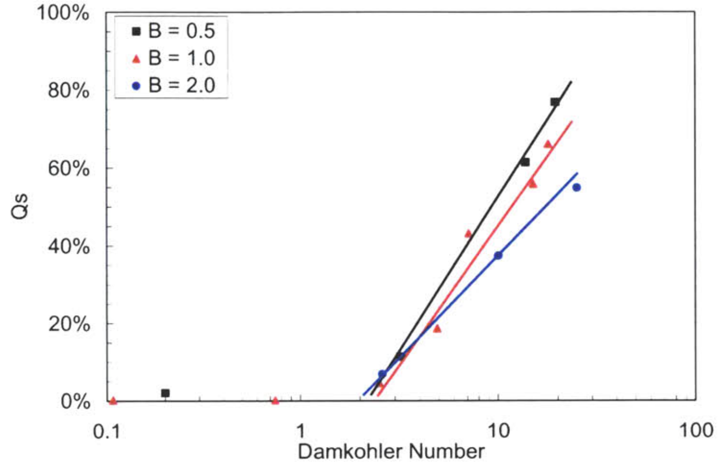

Figure 4.8: Scaled Data Set for B=0.5, 1.0, and 2.0 for H^*=0.18-0.8

As was described in Section 4.2, the greatest heat flux augmentation for a given Damköhler number and fuel level occurred with the attached B=0.5 case, and the scaled heat flux decreased as the blowing ratio was increased. The side-to-side variation in heat flux due to local reaction becomes important at Damköhler numbers of around 2-5 for each blowing ratios examined, based on the definition given in Equation 3.1.

Another interpretation of the Q_s versus Da plots is as a measure of the influence of mixing processes on the driving temperatures that govern the surface heat flux. For example, the B=0.5 case has less mixing of the coolant flow with the freestream than does the lifted B=2.0 case, and consequently higher driving temperatures are achieved in the attached cases, corresponding to higher scaled heat fluxes to the wall. At higher Damköhler numbers there is more time for the mixing to take place, and hence more time for the hot reactive gases to reach the surface. In the cases of low Damköhler number, there is not enough time for the completion of the reactions or the resultant hot gases to mix close to the wall. In this way, the slope of a line on a Q_s versus Da plot can be thought of as a measure of mixing (taking place between the film-cooling layer, the freestream, and the hot oxidized gases) and the delivery of this hot mixed-out gas to the surface. The process of increasing the scaled heat flux to the surface depends on whether the processes are kinetically limited (low Da) or mixing limited (high Da), as well as the fuel to oxidizer mixture ratio.

4.6.3 Calculation of Film Effectiveness From Experimental Data

The experimental data can also be assessed in terms of film effectiveness. It is important to be able to translate these data sets into such terms because film effectiveness is one of the most often used parameters by turbine durability designers. The surface heat flux is defined as the product of the convective heat transfer coefficient and the difference between a driving temperature (which can range between T_∞ and T_f) and the wall temperature. For a measured change in surface heat flux, $q_{hot}-q_{cold}$, it is possible to estimate the change in driving temperature if the behavior of the heat transfer coefficient with temperature and reaction is known The numerical studies presented in Chapter 5 indicate that the change in h due to local reactions for turbine conditions are on the order of –10 to +20 percent. Since these changes in h typically contribute less to the change in surface heat flux than the increase in driving temperature, the heat transfer coefficient is taken to be constant in the forthcoming analyses. However, the levels by which the heat transfer coefficient is augmented may be included as well, as is done in the case studies of Chapter 6. By solving Equations 4.5a and 4.5b for the driving temperatures and knowing the wall and coolant temperature, the film effectiveness can be inferred, using Equation 4.3, with the film temperature being replaced by the appropriately determined driving temperature, T_{dc} or T_{dh}, for the cold and hot cases, respectively.

$$q_{cold} = h(T_{dc})[T_{dc} - T_{wc}] \quad 4.5a$$
$$q_{hot} = h(T_{dh})[T_{dh} - T_{wh}] \quad 4.5b$$
$$q_{max} = h(T_{ad})[T_{ad} - T_{w}] \quad 4.5c$$

Figure 4.9 shows a comparison of film effectiveness with and without reaction for an attached jet at B=0.5, Da=25, and fuel energy content of H^*=0.54.

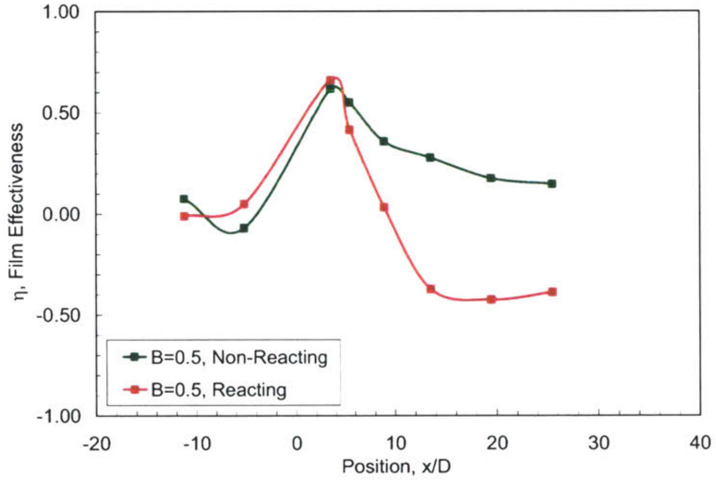

Figure 4.9: Decay in Film Effectiveness due to Local Reactions, B=0.5, H^*=0.54, Da=25

The non-reacting case agrees to within about 25% of the predicted adiabatic effectiveness in literature cases and it will be shown to agree to within 15% of the numerical studies. There is a large difference in film effectiveness between non-reacting and reacting cases at high Da and H^* and the film effectiveness may become negative in the presence of local reactions. This is understood by examining Equation 4.3 and noting that the film temperature, or the estimated driving temperature, may exceed freestream temperatures when local reactions are present, causing the effectiveness to drop below zero. Further examples of the calculated film effectiveness over a range of blowing parameters for attached and lifted jets, and comparisons with the numerical results will be shown in Chapter 5.

4.7 Error and Uncertainty Analysis

This section discusses the errors and uncertainties associated with making transient heat flux measurements. A complete listing of all experimental uncertainties is contained in Appendix G. Two types of errors are considered, 1) absolute error in the calculated quantities, and 2) differential error in evaluating relative changes between the air and N_2 sides of the plate. In the experiment, the wall temperature is known to better than 2 percent, and hence the integrated heat flux is known to better than 2 percent. The freestream temperature is calculated from the shock speed. Although the shock speed is known to better than 0.5 percent, imperfect reflections, viscous effects, and other secondary flow features create uncertainties in total temperature on the order of approximately 10-15 percent [32]. As was discussed in Section 4.2, this uncertainty may be reduced by determining freestream temperature through the alignment of measurements from gauges located upstream of the film-cooling holes with the empirical prediction. Although the heat flux and wall temperature are well known, the absolute heat transfer coefficient is only known to within 10 percent, which is consistent with the run-to-run repeatability of the facility. However, the differential experiment allows for an assessment of the change in the heat flux between the two sides to better than 5 percent. Figure 4.10 shows overall uncertainty bands on a series of data sets over a range of B and H^*.

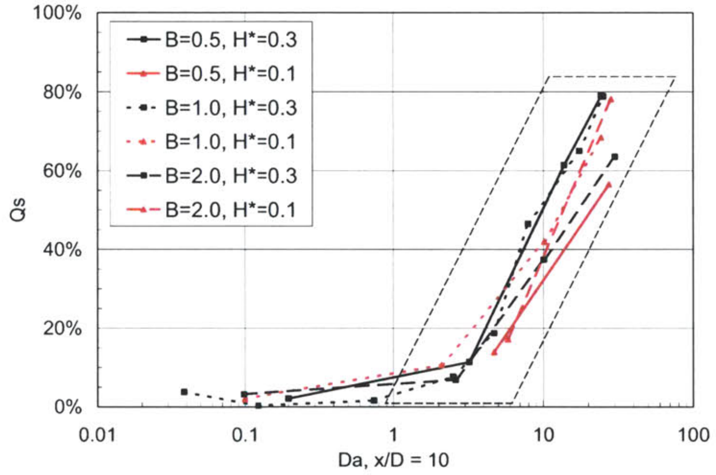

Figure 4.10: Q_s versus Da Uncertainty Bounds

This plot shows that the collapse of Q_s versus Da with fuel level, as was discussed in Section 4.7.2, is within the uncertainty bounds of the experiment, and that uncertainties in the absolute level of Q_s are on the order of 10-15%. The summed experimental uncertainties are around 15% on Da after deducing the driving freestream temperature from the agreement between the transient heat flux measurements and the empirical correlation.

4.8 Chapter Summary

This chapter presented the results from a series of flat plate film-cooling experiments designed to measure the change in surface heat flux due to the presence of near-wall reactions over a range of relevant turbine flow conditions and possible combustor energetic emissions. Experimental tests on an un-cooled and cooled flat plate without a reacting freestream were first shown to demonstrate the validity of the experiment and these results were compared with correlations and predictions from the literature. Reactive flow tests were shown at blowing ratios relevant to turbine operation and over the span of possible combustor energetic emissions discussed in Section 2.6. The resulting data was then scaled for comparison to other freestream conditions. The results indicated that the scaled heat flux, Q_s, increases as the Damköhler number, Da, increases, but is not a function of the freestream heat release potential, H^*. However, the freestream heat release potential is important to determine the level of heat flux augmentation to the surface in terms of total temperature increase. The experimental results and derived parameters of this chapter, as well as the numerical results of Chapter 5, will be implemented in several case study examples contained in Chapter 6.

Chapter 5

Numerical Investigation

To ensure durability in the event of near-wall reactions, film-cooled turbine surfaces must be properly designed such that the film-cooling air does not provide a localized burning region resulting in increased surface heat flux. In this chapter, a numerical study of near-wall reactions is presented to illustrate details of phenomena not accessible through the shock tube experiments. The computational model is compared to the experimental results of Chapter 4 and found to be in good agreement, and the same non-dimensional parameters used to present the experimental data are applied to the computational results. The tool is then extended to study the behavior of near-wall reactions at the freestream, coolant, and wall temperatures associated with modern turbines, as well as over a broader range of mass (B=0.1-4.0) and momentum (I=0.01-8.0) blowing parameters. Finally, the computational tool is used to perform a parametric study over a range of cooling strategies to suggest configurations that are robust to the presence of near-wall reactions. The tool can also be used to rapidly assess current geometries and to predict the range of conditions for which the cooling strategy will remain a viable means of protecting the surface.

5.1 Numerical Approach

The purpose of this section is to outline the computational procedures used in the investigation, including grid generation, sensitivity to grid geometry, and the chemical model employed. The solver used in the numerical studies was Fluent 5.1.

5.1.1 Computational Domain and Grid Construction

A fully unstructured grid was constructed using the methods of References [64, 65]. The results obtained on the grid for adiabatic effectiveness were found to match sufficiently well with the experimental and computational results of References [16, 22, 58] as will be discussed later. The grid was then used for the reacting flow studies with a simple one step reaction model, discussed in Section 5.1.3. In this study, the film-cooling geometry consisted of one or more rows of round, 35° injection holes on a flat surface. Making use of symmetry, the computational domain was reduced to that shown in Figure 5.1.

In the x-direction, the domain extended 20 hole diameters upstream and 40 hole diameters downstream from the first injection hole, which spans the experimental range and range of relevance to film-cooling design studies. The upstream distance, chosen to match the experimental flat plate geometry, allowed for the development of a turbulent boundary layer. In the y-direction, the domain extended 6 hole diameters, with a symmetry condition on the top face. In the z-direction, the domain extended $S_z/2$, so that the center-to-center hole spacing within each row was S_z. In the case of multiple row models, the x-component of the inter-row center-to-center hole spacing was S_x.

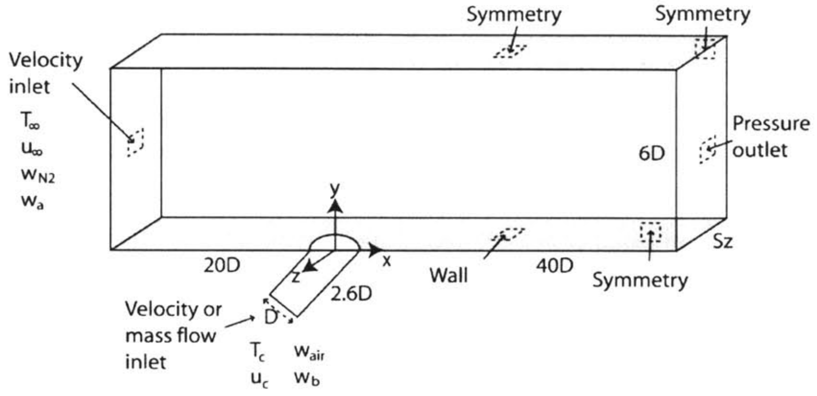

Figure 5.1: Computational Film-Cooling Domain

A fully unstructured mesh was created on the single combined duct and hole volume. First, all edges with variable grid density were meshed. Specifically, edges near the hole inlet area received a higher grid density. Next, a triangular surface mesh was created on each face of the geometry. Finally, the volume was meshed using the Gambit Tet Primitive volume meshing scheme. A close-up of the grid centerline plane near the injection hole is shown in Figure 5.2. The cell density was made higher near the hole region to resolve the rapidly changing flow conditions and to capture the details of the recirculation zone downstream of the injection point.

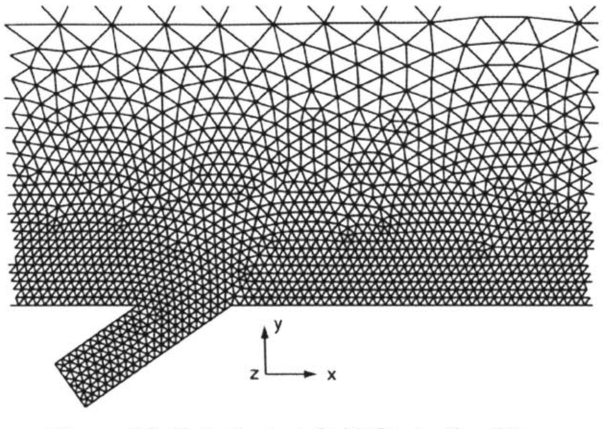

Figure 5.2: Tetrahedral Grid Centerline Plane

5.1.2 Computational Approach, Grid Verification, and Sensitivity

In each simulation, the velocity and temperature were specified for both the duct inlet and cooling hole inlet. At the duct inlet, this specification was direct, while at the cooling hole inlet, it was more relevant to specify the mass flux for blowing ratio comparisons. The duct walls were either adiabatic for effectiveness calculations, or at constant temperature for heat flux calculations, whereas the cooling hole inlet wall was always adiabatic.

The turbulence model used was the standard k-ε, with generalized wall functions for the calculation of near-wall quantities. According to References [64, 65], this combination represents the current standard approach to this class of problems (1999). At both inlets, the turbulence intensity was 1%, and the viscosity ratio was 10. The solver for the simulations was part of the Fluent 5.1 software package. This solver uses a steady, explicit, time-marching procedure to solve the Reynolds-averaged Navier-Stokes equations. Convergence was determined based on overall mass and energy imbalances of less than 0.01 percent. In each case, the scaled residuals were reduced approximately 3 orders of magnitude after about 1500 iterations. Computational times were on the order of 4 hours for non-reacting cases and 8 hours for cases with freestream reactions using a SPARC workstation computer.

To verify adequate cell density for the grid, adiabatic effectiveness results were compared to previous experimental and computational studies in the literature. For the same flow conditions, η(x) from Equation 4.3, was compared to the experimental data documented in Sinha et al. [58], and to the computational data of Walters and Leylek [64, 65]. To compare with these cases, the velocity and temperature at the duct inlet were 20 m/s and 302 K, respectively. The coolant temperature was 153 K, yielding a density ratio of approximately 2.0, assuming ideal gas behavior and negligible pressure difference between the duct inlet and hole inlet. The coolant velocity was set according to the desired blowing ratio. For B=0.5, $u_c=u_\infty B/(DR)=5$ m/s. Plots of centerline η(x), downstream of the cooling hole, are shown in Figure 5.3.

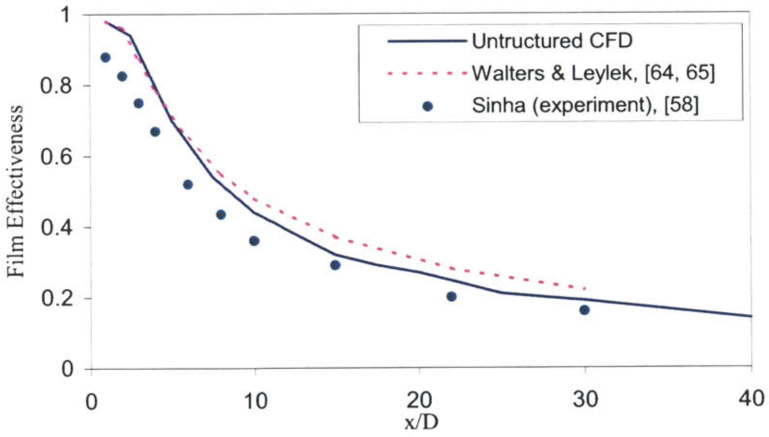

Figure 5.3: Comparison of Centerline (z=0) Adiabatic Film Effectiveness

The effectiveness from both computational cases is higher than from the experimental case of Reference [58]. However, the effectiveness from the current study falls between the experimental data and the previous computational data. This matching of film effectiveness, the main output from adiabatic-wall film-cooling simulations, suggests that the current grid density adequately models the non-reacting flow.

Additional assessments were performed on the mixing rates of the jets with the freestream flow through comparison to experimental and computational cross-sections from 3-20 x/D downstream using References [58, 64]. Comparisons of cross-sectional velocity vector plots indicate that the grid density was sufficient to capture the details of the mixing between the coolant jet and the freestream flow, as well as the re-circulation zone under the jet for the lifted cases.

5.1.3 Two-Layer Grid Models and Modeling Domain Simplifications

The standard viscous model in Fluent uses a wall function approach to simulate a boundary layer. However, a two-layer model can be used if the boundary layer grid size permits resolution of the viscous sublayer. With sufficient boundary layer refinement, the two-layer model is more physically correct because it makes no wall function approximation, however computational run times are significantly longer (3-5 times longer for reactive cases). The advantage of the two-layer grid was that it was able to resolve the recirculation zone immediately following the cooling hole better than the tetrahedral grid, as observed through velocity vector plots. However, in comparison to the tetrahedral grid, there was no marked change in the centerline adiabatic effectiveness. The conditions tested involved mass blowing ratios of 0.5 to 2.0, Damköhler numbers from 0.1 to 30, and $H^*=0$ and 0.5. The similarity between the results of these cases led to the choice of using the tetrahedral grid with wall functions for further studies.

One of the main differences between the computational domain and grids shown in Figure 5.2 and literature test cases is that the plenum supply to the film-cooling jets was not modeled in this investigation. The reason for this was that in developing the numerical tool, the simplest computational grid was initially selected for development and preliminary scoping studies. Since this grid captured many of the details of film-cooling flows and agreed reasonably well with the experimental results in magnitude and trend, studies proceeded without integrating the plenum into the modeling domain. It is important to note that the effects of the plenum can be important and the details of the flow field coming through the film-cooling channels can have an impact on downstream film effectiveness. This may help to explain some of the deviation seen between the numerical and experimental results. A future improvement to these studies would be to add a supply plenum to the computational domain and to examine the differences in downstream film effectiveness.

5.1.4 Reaction Model

To completely model all the details and time scales associated with near-wall reactions, a full chemical mechanism associated with the freestream fuel (ethylene for the shock tube experiments, or more complex combinations for combustor exhausts) would be needed. Although such chemical mechanisms exist for some simple hydrocarbons, they involve many steps (O(50-100)) and can often be inaccurate when applied computationally. The goal of the numerical tool was to provide a quick means for rapidly scoping a range of conditions and cooling strategies. Instead of modeling all of the complex details associated with a reacting flow, a direct matching of the non-dimensional parameters of Chapter 2 was the primary goal. In order to calculate the Da and H^*, a simple, irreversible, one-step reaction was used to model the burning of fuel in the free-stream with the coolant air. In this model, a hydrogen-like species, a, in the free-stream reacts with an oxygen-like species, b, in the cooling air to form a water-vapor-like species, c:

$$a + \tfrac{1}{2} b \rightarrow c \tag{5.1}$$

The properties of each species were taken as hydrogen, oxygen, and water vapor. The molar rate of creation of c is given by the Arrhenius model, where [a] and [b] are the molar concentrations of a and b, respectively.

$$R_c = A^*\exp(-E_a/RT)\,[a][b] \tag{5.2}$$

The initial flow conditions were specified by mass fractions, w, at the duct and cooling hole inlets. The remaining species were nitrogen in the duct, and air in the jet: $[N_2]$, [air]. An argon freestream was used for simulating the experimental cases, and a nitrogen freestream for the turbine conditions of Section 5.3.1.

For particular flow conditions, the calculation of Da proceeded as follows. First, the characteristic flow time, τ_{flow}, was defined as $\tau_{flow}=L/U_\infty=10D/U_\infty$, as in Equation 3.1 Second, the reaction time, $\tau_{chem,}$ was estimated for an equivalence ratio of $\Phi=1$, simulating the region of mixing between the coolant and freestream flows. Initially taking the fuel [a] as a parameter, $[b]=\tfrac{1}{2}[a]$. The initial densities of the free-stream and coolant were computed using the ideal gas law at the operating pressure. These densities were used to find the initial molar concentrations, $[a]_0$ and $[b]_0$, in the freestream/coolant. For example, $[a]_0=w_a\rho_\infty/M_a$, where M_a is the molar mass of species a. The associated N_2 and air concentrations are found under the assumption that the species proportions in the duct and hole remain constant: $[a]/[N_2]=[a]_0/[N_2]_0$, $[b]/[air]=[b]_0/[air]_0$. The Damköhler number can be easily varied in the numerical cases by changing the pre-exponential factor, A, whereas in the experimental investigation, the primary control of the Damköhler number was through the chemical time, which was varied by changing the freestream temperature.

For the fuel-lean conditions tested, it was assumed that $\Phi=1$ was reached at freestream conditions at some location through diffusion of the coolant into the freestream. The chemical time was determined from the initial rate of creation of c, and the characteristic concentration of c:

$$1/\tau_{chem} = R_c/[c] = A^*\exp(-E_a/RT)\,[a][b]/[a] = A^*\exp(-E_a/RT)[b] \tag{5.3}$$

In addition to the Damköhler number, which is representative of the rate of the reaction, the reaction is also characterized by a maximum heat release potential which is simplified from Equation 2.2 as:

$$H^* \sim (T_{ad} - T_{t\infty})/T_{t\infty} \tag{2.2}$$

H^* is determined for a given free-stream temperature and fuel concentration through an adiabatic flame temperature calculation. T_{ad} was found from a chemical equilibrium calculation with the species a, b, N_2, and background diluant of either argon or nitrogen.

5.2 Numerical Results and Comparison to Experimental Data

Section 5.1 presented comparisons which benchmarked the numerical tool to literature film-cooling studies. However, for the tool to be useful in the design of reactive flow film-cooling strategies, it must be compared against the experimental results from the shock tube experiments. A numerical study was completed over the range of blowing parameters, Damköhler numbers, and fuel levels that were studied in the experiments to form a back-to-back comparison and to determine the utility of the numerical tool.

Figure 5.4 presents a comparison between attached, B=0.5, and lifted, B=2.0, jets in non-reactive, Da=0.3, and highly reactive, Da=25, cases for $H^*=0.54$ with an adiabatic wall.

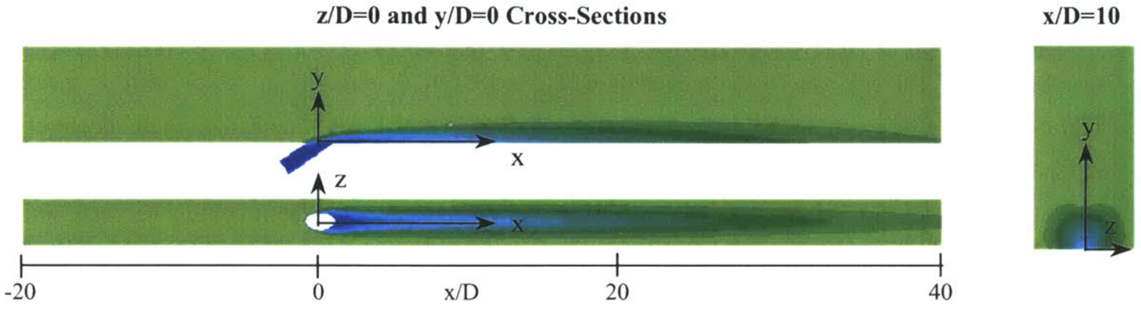

Case 1a: B=0.5, Da=0.3, H^*=0.54

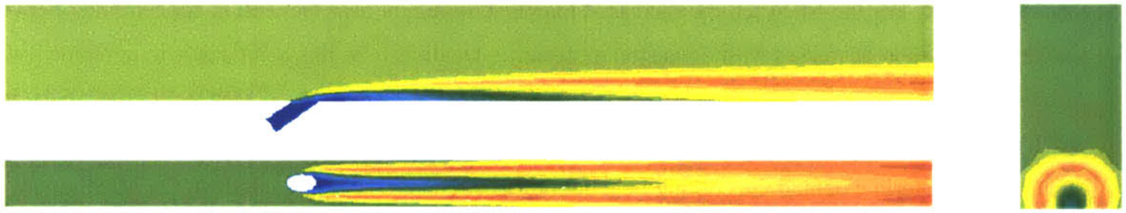

Case 1b: B=0.5, Da=25, H^*=0.54

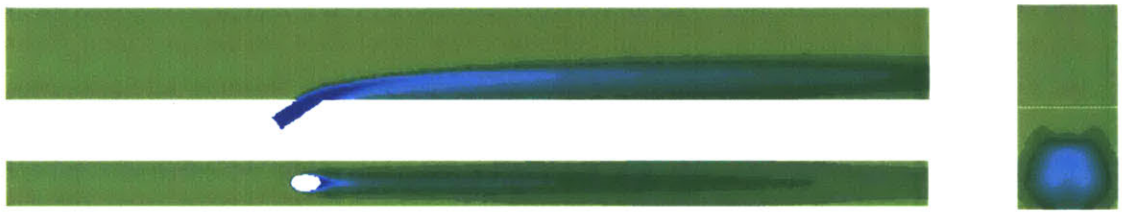

Case 2a: B=2.0, Da=0.3, H^*=0.54

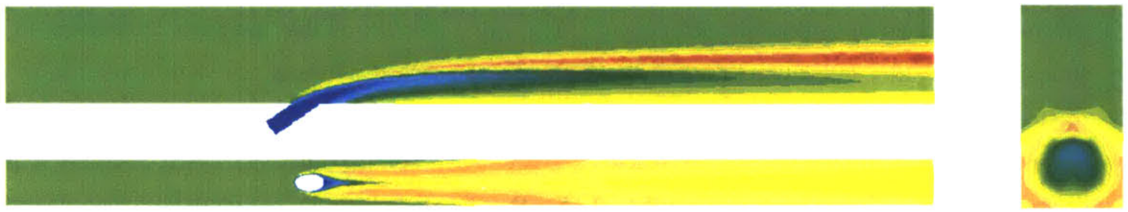

Case 2b: B=2.0, Da=25, H^*=0.54

Figure 5.4: Sample Numerical Study Results for Adiabatic Wall Cases

In each set, the upper total temperature contour plot shows a cross-section through z/D=0, and the lower plot is a cross-section at the wall, y/D=0. In each case, the freestream temperature was 1200 K, the coolant air temperature was 300 K, and the freestream velocity was 100 m/s. Case 1a and 2a show non-reacting film-cooling flows. The results of these numerical simulations were compared with literature predictions for film effectiveness and with the experimental results for a non-reacting freestream, and agreed to within 20 percent.

Cases 1b and 2b demonstrate the result of increasing the Damköhler number, keeping all other quantities fixed. The adiabatic flame temperature, T_{ad}, is 1850 K. The maximum temperature in the flow field downstream of the film-cooling holes reaches 1722 K. Attached jet temperature contours show the region of increased temperature is first concentrated on the edges of the jet and on the top of the film layer and then mixes toward the surface. The region of augmented heat flux propagates to the centerline at around x/D=10 and continually increases downstream. The lifted jet shows two distinct regions of reaction, the top and bottom of the jet cross-section. The reactions take place circumferentially around the cooling jet as can be seen in the x/D=10 cross-sectional view of Figure 5.4. The peak temperature in each of these zones is 1683 K. For the lifted jet, the increased temperature region near the wall is concentrated between 3<x/D<15, and then decreases with downstream distance. Qualitatively, this behavior is in agreement with the experimental data of Figure 4.5.

The z/D=10 cross-section plots indicate that for the attached jet the peak wall temperature does not occur on the centerline behind the cooling hole but rather around z/D=±1.0. In contrast, the lifted jet always exhibits a peak wall temperature increase on the centerline. This can be understood because the location of the reactive interface between the freestream and the coolant is different for attached and lifted jets. In the attached case this interface meets the wall off-centerline, whereas for lifted jets this interface is closest to the wall at z/D=0. The difference between the wall temperature at z/D=0 and z/D=±1.0 for the attached cases, at x/D=10 is 5-15 percent depending on Da and H^*.

Another important result of such cases is the degradation in adiabatic film effectiveness with reaction, which are shown for the cases of Figure 5.4 in Figure 5.5. These figures show that effect of near-wall reactions can cause the adiabatic film effectiveness to become negative, meaning the film temperature has become hotter than the freestream temperature. The figure also shows that there are differences in the structure of the film effectiveness between the lifted and attached jet cases, for both non-reacting and reacting flow scenarios. For attached jets, the film effectiveness continues to decrease with increasing downstream distance when near-wall reactions are present. For the lifted jet cases, there is a peak degradation in film effectiveness at around 10-15 x/D, which is where the re-circulation zone under the lifted jet is still active and trapping the hot gases. For these two cases, the peak decrease in film effectiveness is larger for the attached jet and occurs further downstream, but positive film effectiveness is maintained up to 15 x/D. In contrast, the degradation in film effectiveness for the lifted case is never as severe as the attached cases (because of the mixing of the freestream and coolant gases) and improves with downstream distance. However, the effectiveness becomes negative near the film-cooling holes at 3-5 x/D.

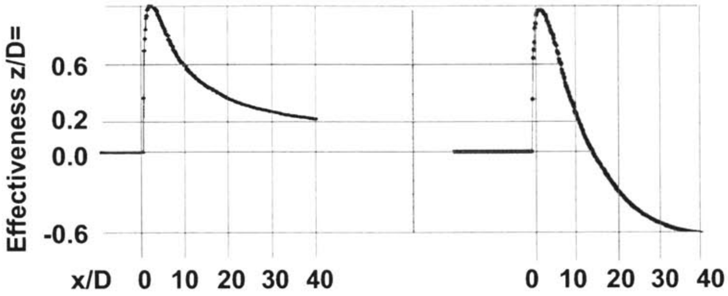

Case 1a: B=0.5, Da=0.3, H^*=0.54 **Case 1b: B=0.5, Da=25, H^*=0.54**

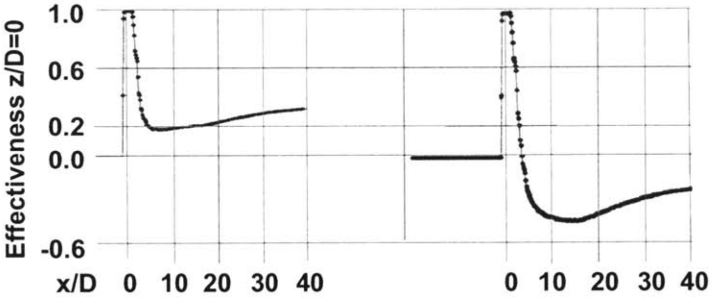

Case 2a: B=2.0, Da=0.3, H^*=0.54 **Case 2b: B=2.0, Da=25, H^*=0.54**

Figure 5.5: Degradation in Adiabatic Film Effectiveness for Cases Shown in Figure 5.4

Figure 5.4 and Figure 5.5 represent a set of sample cases that were studied to develop the numerical tool and to compare with experimental results of Chapter 4 after being appropriately non-dimensionalized.

Figure 5.6 shows a recap of Figure 4.7, but also contains numerical results showing the collapse of Q_s versus Da for any fuel concentration at B=0.5. In the experimental investigation the range of H^* displayed on this plot was 0.05-0.6, and the H^* studied in the numerical simulation was 0.54. Figure 5.6 indicates that there is good agreement between the numerical results and the shock tunnel tests in magnitude and in trend over the range of Da investigated, particularly at the higher Da range. At Damköhler numbers of less than about 0.5, both the experiment and computational results show no change in scaled surface heat flux, regardless of the amount of freestream fuel that was present. The agreement between the experimental results and numerical studies deviates the most in the range of Da=0.5-10.

Reasons for this deviation may include real chemical effects that are taking place in the experiment, but not captured by the simple, 1-step computational reaction model. This may be attributable to the differences in the way the Damköhler numbers are varied in the experiment and numerical studies (to change the Da in the experimental cases, the freestream temperature had to be varied, whereas in the numerical studies Da could be varied by changing the pre-exponential factor of Equation 5.3). Also, since the Damköhler number definitions are slightly different in the way that the chemical times are estimated (computation versus Arrhenius form of Equation 5.3 for the CFD), this may lead to a shift of the data on the Da axis, but not a change in shape. Nonetheless, if the uncertainty bounds developed in Figure 4.10 are applied to Figure 5.6 (and Figure 5.7), the numerical results are close to lying within this range. The comparisons with the experimental results provided confidence that the numerical tool can be used to perform studies that inform about trends and behavior of near-wall surface reactions.

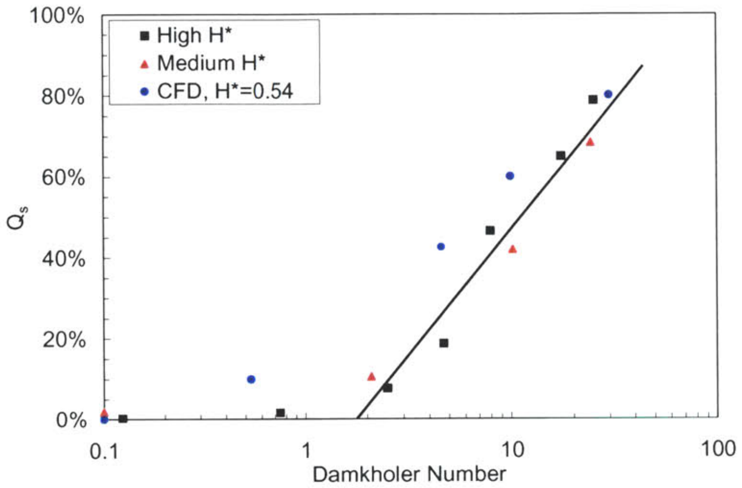

Figure 5.6: Comparison of Q_s versus Da for Numerical and Experimental Results B=0.5

Another comparison of experimental to numerical results for variation with blowing ratio is shown in Figure 5.7 which is analogous to the experimental results presented in Figure 4.8.

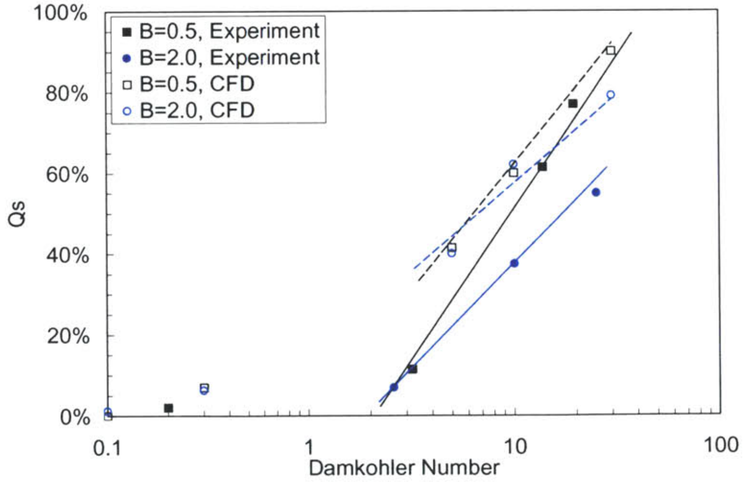

Figure 5.7: Influence of Blowing Parameter for Numerical and Experimental Cases

This plot shows that the numerical tool captures the decrease in scaled surface heat flux as the blowing ratio is increased for high Damköhler numbers. The difference in Q_s between B=0.5 and 2.0 at a Da of 30 is about 18% for the experimental results and 13% for the computational equivalent.

The numerical studies were also used to determine the change in film effectiveness due to local reaction, as was presented in Figure 4.9 of the experimental results. Summary plots are shown in Figure 5.8 for two blowing ratios (attached and lifted jets), at freestream fuel levels for both inert and reacting cases.

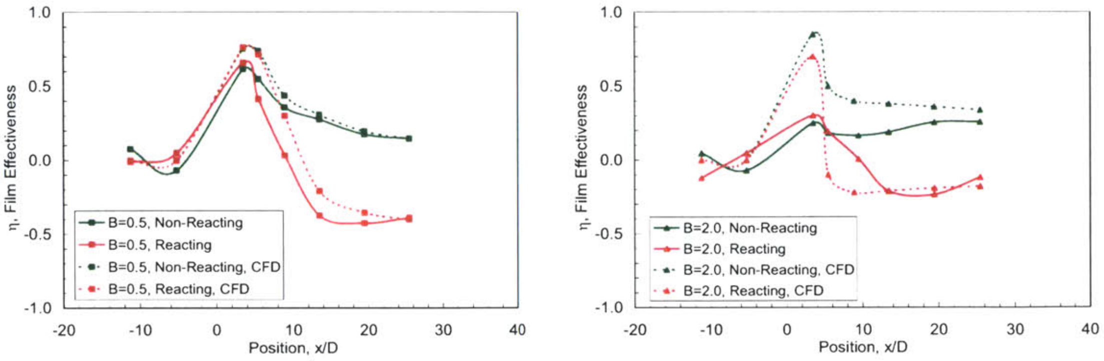

Figure 5.8: Film Effectiveness Comparison for B=0.5 and B=2.0, H^*=0 and 0.35, Da=25

The figures show that the effects of local reaction, as predicted by the numerical tool and the experiment are in good agreement to within about 15% and in behavioral trend. For the H^*=0.35 case the impact of on film effectiveness is substantial. The maximum degradation in film effectiveness occurs for the attached jet, but at downstream distances on the order of 20-25 x/D, whereas for the lifted jet the maximum impact to film performance is located at around 5-10 x/D downstream. The numerical model predicts a sharper improvement in the film effectiveness after peak degradation than the more distributed results from the experiment at B=2.0. This was a consistent observation in all experimental to numerical data comparisons, although downstream predictions, after x/D=10, are in better agreement. Considering the performance behind the centerline alone, this plot suggests that it may be more advantageous to use attached jets than lifted ones, as long as the film-cooling holes are spaced no more than 10-15 x/D apart, which is upstream of where the attached jets react with the freestream enough to lead to maximum heat flux augmentation. For lifted jets, the peak heat flux is within 10 x/D of the cooling hole and spacings would have to be on the order of 3-5 x/D apart to protect the surface from the hot reactive gases. More on film-cooling hole spacing surveys will be presented in Section 5.4. A complete list of all the numerical studies completed in this research program can be found in Appendix F.

5.3 Further Numerical Studies

The results of Section 5.2 were encouraging in their agreement with the experimental data, and suggest that the numerical tool is a useful and rapid way to scope film-cooling performance in the presence of local reactions. The purpose of this section is to apply the tool at realistic turbine conditions and evaluate changes in surface heat flux, as well as to examine the assumptions made about the changes in convective surface heat transfer coefficient.

5.3.1 Application of the Numerical Tool to Turbine Conditions

After the numerical tool was benchmarked, conditions were altered to freestream temperatures from 1600-2500K, wall and coolant temperatures from 900-1200K, blowing ratios from 0.1-4.0, Damköhler numbers from near zero to 30, and freestream fuel levels from zero to $H^*=0.5$, to simulate realistic 1st-stage turbine environments. The numerical tool was able to complete individual reacting cases in about 10 hours per test, and provided resultant data plots similar to those shown in Figure 5.7 and Figure 5.8, with maximum scaled heat fluxes of $Q_s=90\%$ at Da=30 and $H^*=0.5$. The basic results looked similar to those shown in the example plots of Figure 5.4. The impacts of varying the wall temperature and coolant temperature will be discussed in the next section.

5.3.2 Convective Heat Transfer Coefficient and Wall Temperature Impacts

The numerical studies were useful for ascertaining how much of the augmentation in heat flux due to local reactions was attributable to a change in driving temperature and how much was due to a change in heat transfer coefficient, $h=q_w/(T_\infty-T_w)$. To investigate the changes in h, the wall temperature was varied from 300 K (coolant temperature) to 1200 K (freestream temperature) with and without reaction. As the wall temperature was increased, the percent change in spatially-averaged heat transfer coefficient, $(h_{hot}-h_{cold})/h_{cold}$, increased from –5 to +50 percent. For a similar series of cases at turbine conditions, where the percentage increase in wall temperature to the freestream temperature is less, the maximum change in heat transfer coefficient was around 25-30%.

For the numerical studies with an adiabatic-wall, it is useful to compare T_s ($T_s=(T_{hot}-T_{cold})/(T_{max}-T_{cold})$) and Q_s. It was found that these two non-dimensional parameters are equivalent to within 10-20%, indicating that changes in convective heat transfer coefficient are small relative to changes in driving temperature. This equivalence can be shown by expressing the wall heat flux at a given x location as a product of a heat transfer coefficient and the difference between a driving temperature and the wall temperature. Two possible heat transfer coefficients are obtained by using the film temperature, T_f, and the free-stream temperature, T_∞:

$$q_w(x) = h_f(x)\,(T_f(x)-T_w) = h_{ref}(T_\infty - T_w) \qquad 5.4$$

To determine the variation in these heat transfer coefficients, the numerical studies were performed at shock tube experimental conditions, with a non-adiabatic wall, at three values of θ, defined by:

$$\theta = (T_\infty - T_c)/\,(T_\infty - T_w) \qquad 5.5$$

Using the relation $h_{ref}=h_f(1-\eta\theta)$ and adiabatic wall test cases, the heat flux from these simulations were scaled to produce the heat transfer coefficients shown in Figure 5.9.

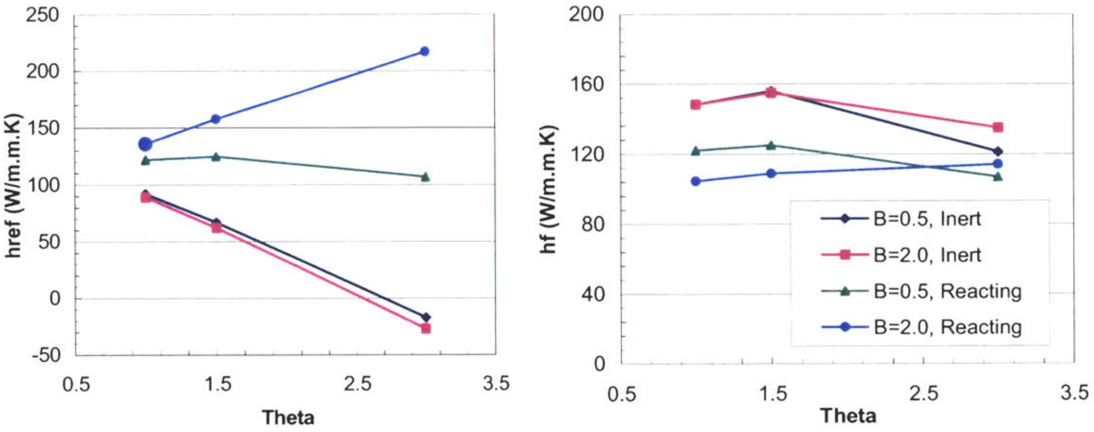

Figure 5.9: h_{ref}, and h_f from Numerical Heat Flux Survey of Varying θ

While h_{ref} varies significantly with θ, B, and reaction, the variation in h_f is much lower – on the order of 25% for a given set of flow and reaction parameters. It is this convective heat transfer coefficient associated with the film or driving temperature, shown in the first of Equations 5.4, that is used in this study. Conversely, the last of Equations 5.4 does not account for changes in surface heat flux through the driving temperature, which remains at T_∞, but entirely through changes in h_{ref} and T_w, the later of which is small for the experimental test cases. Based on these results, the simplifying assumption is made that h_f is constant between the reactive and non-reactive cases. Expanding the scaled heat flux yields:

$$Q_s = \frac{q_{hot} - q_{cold}}{q_{max} - q_{cold}} = \frac{h_{hot}\left(T_{f,hot} - T_{w,hot}\right) - h_{cold}\left(T_{f,cold} - T_{w,cold}\right)}{h_{max}\left(T_{f,max} - T_{w,max}\right) - h_{cold}\left(T_{f,cold} - T_{w,cold}\right)} \qquad 5.6$$

The maximum film temperature is identified with the adiabatic flame temperature, $T_{f,max}=T_{ad}$, so under the assumption that $h_{hot}=h_{cold}=h_{max}=h_f$, and consequently $Q_s=T_s$. Thus, the temperature rise from the adiabatic wall runs can be used to predict the expected heat flux rise in the presence of reaction. To verify the calculation procedure for Da and H^*, numerical T_s data was compared to shock tube Q_s data for $H^*=0.35$ and varying Da and gave comparisons in magnitude to within 10-15% of those shown in Figure 5.7.

This study not only indicated that to estimate the change in surface heat flux due to local reaction the changes in convective heat transfer coefficient could be neglected to first order, but also established a data base of what these changes were for a range of turbine conditions, as shown in Figure 5.9. The numerical tool can be run relatively quickly (~1 day) to ascertain the changes to convective heat transfer coefficient and film effectiveness over a range of hydrodynamic and reactive conditions. An analytical study of the changes in convective heat transfer coefficient in Equation 4.1 with driving temperature was performed using a constant pressure heat addition model. The results indicated that for the range of driving temperatures possible for H^*=0-0.8, the change in convective heat transfer coefficient decreased from zero to 30 percent.

5.4 Film-Cooling Design Strategy with a Reactive Freestream

The numerical tool was used to study the impact of heat transfer on surfaces using multiple rows of cooling at different downstream spacings and lateral stagger. The goal was to parametrically determine the film-cooling strategies best suited to protecting the surface over a range of thermal and fluid conditions associated with an advanced engine design, as well as over a range of fuel levels that might be present in the freestream. The test conditions for this optimization study were the turbine base-line conditions of Section 5.3.1, $T_{t\infty}$=2000 K, T_c=950 K, P=20 atm. and U_∞=100 m/s.

A reasonable method for designing film-cooled surfaces for round holes is to first decide a baseline film effectiveness the surface must be kept above to maintain integrity for the required lifetime. This criterion sets the x/D spacing, which will vary with blowing ratio. The second row of film-cooling holes at a particular x/D location can then be staggered at some z/D distance so to cover more of the surface and eliminate large gradients between nearby hot freestream and cold cooling flows. This type of design can be constructed from effectiveness data over a range of blowing ratios and x/D and z/D profiles, which already exists in the literature [22]. For a flow with a reacting freestream, the same strategy can be adopted, but the necessary data base and set of film effectiveness correlations have not yet been developed. This section of the thesis takes some of the first steps toward establishing such a database for round, 35° cooling hole configurations.

5.4.1 Multiple In-Line Cooling Hole Studies

A series of numerical tests were completed at turbine conditions over a range of B=0.1-4.0, I=0.005-8.0, Da=0-30, and H^*=0-0.5 for a row of round film-cooling holes. Several averaging domains (0<x/D<10, 20, and 40) were examined and the mean film effectiveness was calculated for z/D lateral spacings of 3 and 5 diameters. For example, at a blowing ratio of B=0.5 (I=0.15, attached jet), H^*=0.15, and a z/D lateral spacing of 5, the average film effectiveness from 0 to 10 hole diameters behind the cooling jet was –0.03 and for a domain of 0 to 40 hole diameters downstream behind the cooling jet was –0.14. These results demonstrated the expected trend because the surface heat flux augmentation due to near-wall reaction increases with downstream distance for the attached jet case, as shown in Figure 5.4.

The averaging domain over which the effectiveness is taken is an important parameter in these studies because the presence of more or less film cooling within the domain will yield different values. This is affected by design constraints such as the total compressor bleed mass flow that is available to cool a turbine stage. For this reason, three averaging domains were tracked of 10, 20 and 40 x/D behind the first row of cooling holes and with a width set by the lateral spacing of the holes in the row. The values attained in each of the averaging domains may be counterintuitive. This is because for cases where the film temperature is lower than the freestream temperature more cooling is favored (smaller domains show higher average effectiveness), whereas when the film temperature increases to levels above the freestream temperature the average effectiveness of the surface improves with less cooling (larger domains show higher film effectiveness). Plots of film effectiveness, as were shown in Figure 5.4 and Figure 5.8 are helpful in understanding what is occurring. For example, the overall trend was that as the lateral spacing is increased the average film effectiveness decreases for positive film effectiveness. However, when film effectiveness becomes negative (the case where it is better to have no film-cooling at all), larger z/D spacings are favorable because more of the surface is exposed to the freestream temperature, which is cooler than that of the reacting film layer. As a result an averaging domain that contains more wall surface would be biased in such a case. A complete list of the numerical cases studied can be found in Appendix F.

Completion of this initial series of tests, at z/D spacings of 3 and 5, allowed for the positioning (x/D) of the next row of in-line cooling holes behind the first row. From these results it was decided to proceed with a cooling strategy that utilized attached jets, B=0.1-1.0, since a second row of cooling holes could be located at x/D=10, and would maintain an average film effectiveness above zero for $H^{*}<0.25$. For lifted jets the next row of cooling holes would have to be located at an x/D of about 3-5 to maintain positive film effectiveness at the same H^{*} maximum.

Numerical tests were completed for B=0.1-1.0, for 2 and 4 rows of in-line film-cooling holes and an example of the downstream film effectiveness is shown in Figure 5.10. In this case the film effectiveness was always above a threshold level of 0.2 for all averaging domains examined. The plots show film effectiveness for two in-line rows of film-cooling holes spaced 10 x/D apart for attached and lifted jets under non-reacting and reacting scenarios. The top two figures demonstrate that for the attached jet cases, a second row of film cooling holes located at 10 x/D keeps the film effectiveness above zero between the two rows of film cooling holes and the film effectiveness remains positive 10-15 x/D downstream of the second row of film cooling holes. For the lifted jet cases, the second row of film cooling holes is too far downstream and there is a region between the two rows of holes that has negative film effectiveness. Such plots form the basis for suggesting hole locations and spacings to keep the surface film effectiveness above zero when the freestream flow is fuel-rich.

Each figure also shows a superposition method, which is often used to predict the performance of multiple rows of in-line and staggered film cooling holes. The details of this method are contained in References [22, 37]. Superposition over-predicts the effectiveness for the low Damköhler number cases, and under-predicts the effectiveness for high Damköhler number cases. This is expected since at high Da, most of the fuel reacts at the first cooling hole, shielding the second cooling hole from reaction and increasing the adiabatic effectiveness following the second hole. At low Da, the reaction from the first hole coolant becomes important by the time the flow reaches the second hole, decreasing the effectiveness. In addition, superposition does not take into account the three-dimensionality of the flow (such as the vortical mixing taking place at the boundary of the cooling jet and freestream [16]), and the increased mixing is not modeled. A new method of superposition in the case of fuel-rich freestream will be discussed in Chapter 7.

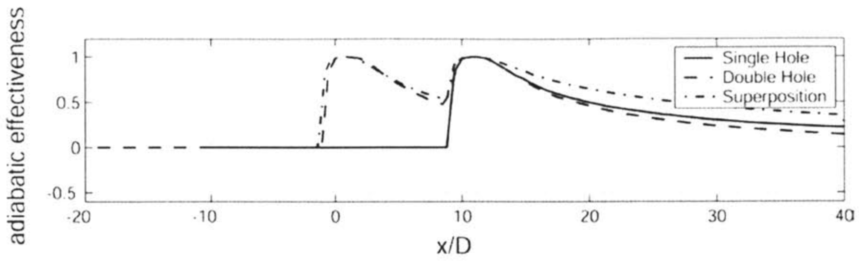

Case 1a: B=0.5, Da=0.3, H^*=0.54

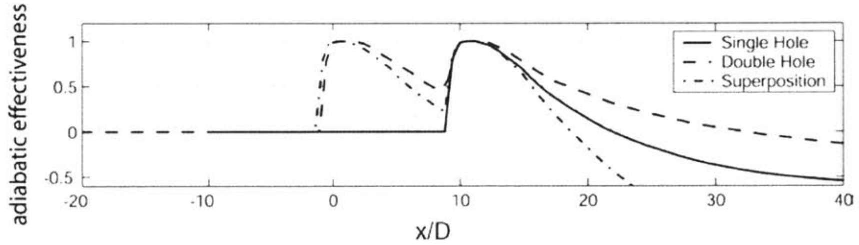

Case 1b: B=0.5, Da=25, H^*=0.54

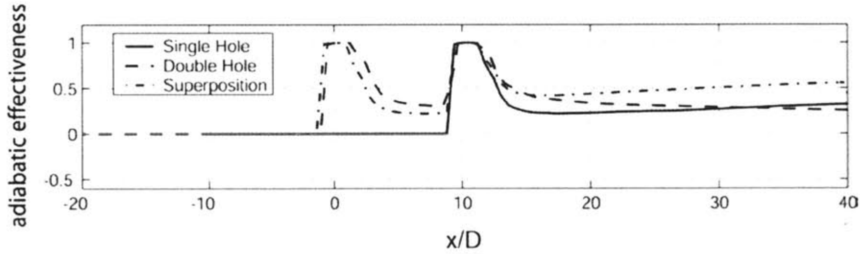

Case 2a: B=2.0, Da=0.3, H^*=0.54

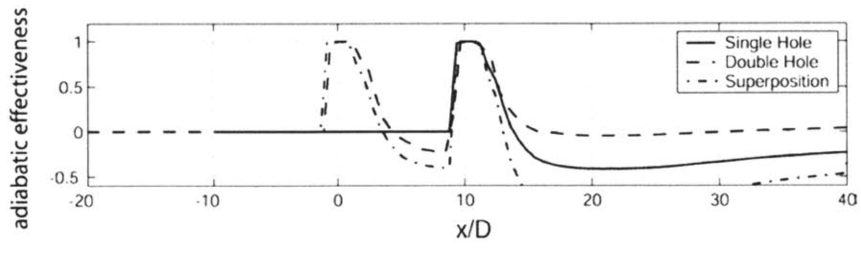

Case 2b: B=2.0, Da=25, H^*=0.54

Figure 5.10: Film Effectiveness for Two In-Line Rows of Film-cooling Holes, B=0.5, H^*=0.15

5.4.2 Multiple Row, Staggered Film-Cooling Hole Studies

To obtain improved film-cooling effectiveness in the lateral direction, a parametric study of stagger in alternating rows of film-cooling holes was performed over the same range of parameters summarized in Section 5.4.1, but also including stagger studies at z/D=3 and 5 at an x/D=10 spacing of each row. As an example, the average film effectiveness for two rows of cooling holes at 10 x/D apart, 5 z/D spacing, and stagger of z/D=5 for B=0.5 and $H^*=0.15$ gives an average film effectiveness of 0.03 and –0.08 for averaging domains of 20 and 40 x/D downstream of the first row of film-cooling holes, respectively. The complete test matrix of these tests is also included in Appendix F, which covers 36 possible combinations of stagger and spacing over $H^*=0\text{-}0.5$, and B=0.1-2.0 (I=0.005-1.9).

A sample result for two rows of film-cooling holes, with an z/D spacing of 5, z/D stagger of 3, for B=0.5, $H^*=0.3$, at Da=0.3 and 25 are shown in Figure 5.11.

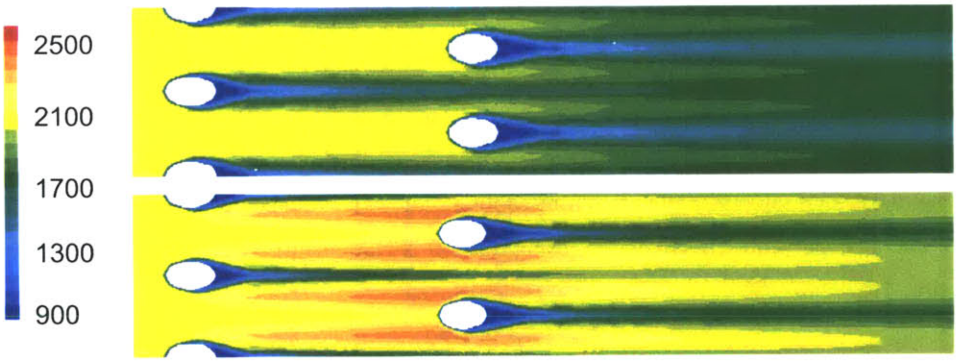

Figure 5.11: Example Surface Temperature for Multiple Row, Staggered Film-Cooling Design, B=0.5, $H^*=0.3$, $T_{t\infty}=2000$ K, $T_c=900$ K. Upper Plot Da=0.3, Lower Plot Da=25

The upper plot contains a fuel-rich freestream, but Da is sufficiently low that no relevant augmented heat release to the surface occurs. The z/D spacing of the two rows, and the z/D stagger of the second row relative to the first, provides one of the best combinations of film coverage over the parameterized space that was investigated, with an average film effectiveness of 0.35 averaged over 40 diameters downstream of the first row of film-cooling holes. The bottom wall temperature plot shows the effect of reaction on this design with $H^*=0.3$. Although some regions behind the first row of film-cooling have negative film effectiveness, this particular design was successful in maintaining a positive film effectiveness for averaging domains taken 20 and 40 cooling hole diameters downstream of the first row of holes. Figure 5.11 also shows that after two rows of film-cooling holes, the reaction is kept away from the surface by the protective attached layer. The burning, and correspondingly the hottest film temperatures, are confined to the upper portion of the film-cooling layer and not allowed to progress toward the surface. This was evident in the analogous 4 row example to that shown in Figure 5.11. In this case, as the hot reactive gases start to mix toward the wall, a new row of film-cooling jets replenishes the layer with a cool fluid momentum flow, keeping the hot reacting flow on the top side of the layer.

The design strategy of Figure 5.11 suggests that another way to protect a surface from near-wall reactions may be with a sheet of film-cooling gas. Such a design might be established by concentrating the lateral and downstream spacings of the first few rows of film-cooling holes close together, say x/D=5 and z/D spacing of 3. The second row would have a stagger of 3 z/D to keep even the regions directly behind the first row, where the film surface, freestream, and wall intersect (which is the reaction flame front) at film effectiveness above zero. Subsequent rows of staggered film-cooling holes could then be located further apart, say 10-15 x/D, because the attached sheet of film-cooling would keep the burning zone on the upper surface of the layer [56]. Such a geometry should be examined in future investigations.

5.4.3 Assessment of a Geometrically Fixed Film-Cooling Strategy

The numerical tool is also able to assess the performance of a given film-cooled surface as the freestream fuel concentration is increased, to determine when the cooling scheme will no longer be favorable relative to no cooling. For example, consider two film-cooling strategies similar to the one shown in Figure 5.11, where the first row has a z/D spacing of 5, and the second row is located 10 x/D downstream with staggers relative to the first row of 3 and 5 z/D. The question to be answered in this section is how much can the freestream fuel content be increased, and hence how much additional surface heat flux can the design tolerate, before this film-cooling strategy is no longer effective? Figure 5.12 shows a plot of the average film effectiveness (using the 40 x/D domain) versus freestream fuel energy concentration, H^*.

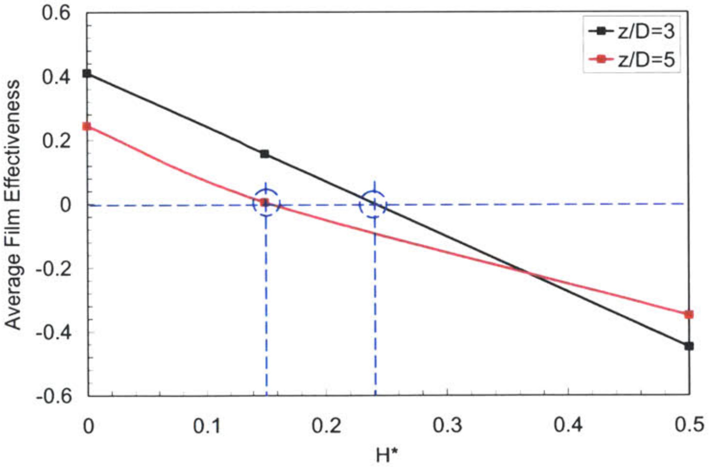

Figure 5.12: Example of Assessment of a Film-Cooling Strategy

The plot shows, for both z/D staggers of the second rows, at what levels of H^* the average film effectiveness to the surface becomes negative. For example, at a z/D staggering of 3, the film-cooled surface design no longer protects the surface for H^* greater than about 0.25. Such plots can be constructed rapidly, for a given Da, using the numerical tool. They will be employed again in the case study examples of Chapter 6 to critique potential cooling design strategies.

5.5 Chapter Summary

The purpose of this chapter was to review the development, validation, and exploitation of a numerical tool that characterizes near-wall reactions, as well as to develop a primitive film-cooling design capability for turbine surfaces. The results of the numerical model were found to agree well with literature predictions over a range of film-cooling conditions relevant to turbine design and with the experiments presented in Chapter 4. The agreement was sufficient so the numerical tool could be used to rapidly scope potential design spaces, to understand the basic trends and magnitudes in the change in surface heat flux, degradation to film effectiveness, changes in convective surface heat transfer coefficient, and to study off-surface effects in the presence of near-wall reactions. The numerical tool was also employed to investigate a parametric space of hole spacings and blowing ratios which were likely to be robust enough to withstand near-wall reaction effects. It was found that attached jets, B=0.1-1.0, at a z/D spacing of around 10 and lateral stager of 3-5, were effective in keeping the film effectiveness over values of 0.2 for freestream fuel levels up to $H^*=0.15$. The comparisons with data show that the numerical tool can also be used to assess given film-cooling designs and to determine at what values of the critical parameters (B, Da, and H^*) the design no longer becomes an effective way to protect the surface.

Chapter 6

Application of Results

This chapter contains three case study examples which are an application of the experimental and computational data for prediction of surface heat flux augmentations due to near-wall reactions.

6.1 Case Study 1: Airfoil with Film-cooling

To determine the effect local reactions have on the heat flux to a blade surface, consider a film-cooled turbine blade, such as that shown in Figure 6.1. This blade will be taken as a high pressure turbine, 1st-stage airfoil for the purposes of the case studies [69].

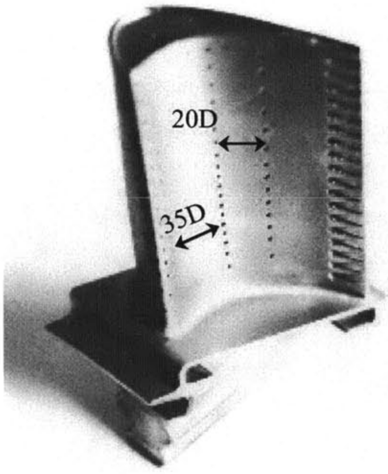

Figure 6.1: Sample Film-Cooled Turbine Blade [69]

The figure shows the approximate distances between two rows of film-cooling holes, at about 35 and 20 diameters apart. To demonstrate how the tools developed in this thesis may be applied to this geometry, the airfoil will be taken to operate at B=1.0 with a average film effectiveness of 0.4. Velocity over the blade is 100 m/s, freestream temperature and pressure are 2000 K and 25 atm., respectively, the coolant temperature is 950 K, and the wall temperature is 1200 K, which are generic fluid conditions in the 1st-stage of a modern aircraft engine [56]. Fuel-rich streaks with an energy of $H^*=0.2$ are assumed to have convected from the combustor to the blade surface. Such a case is analogous to a fuel-rich streak with an equivalence ratio of 1.2 exiting the combustor.

A representative Damköhler number for this flow scenario can be calculated using the definitions provided in Equation 2.1. Using a spacing of 2 cm to the mid-point distance between film-cooling holes on the blade, the flow time over this distance is 200 μs. An adiabatic, premixed calculation, as discussed in Reference [39], is then performed to arrive at the chemical time and maximum total temperature change. The τ_{chem} and ΔT_t for the freestream temperature, pressure, and fuel content are 40 μs seconds and 350 K, respectively giving a Damköhler number of approximately 5. From Figure 4.8, the scaled heat flux ratio, Q_s, is roughly 0.2. Given η=0.4 for this scenario, T_f is calculated from Equation 4.5, which is used as the representative driving temperature, T_{dc} (T_f~T_{dc}=1630 K).

Next q_{cold} and q_{max} are calculated for the given conditions. The heat transfer coefficient, calculated using the flat plate correlation, Equation 4.1, is about 1700 W/m^2 K. For simplicity, the change in convective heat transfer coefficient may be considered negligible, or using the numerical results this calculation may be refined by estimating a change in heat transfer coefficient of about 15% based on Figure 5.9 for θ=1.2 from Equation 5.5. Increase in the heat transfer coefficient with reaction would further magnify the estimated augmentation in heat flux due to reaction. Also note that in the calculation for q_{max}, the film effectiveness is allowed to go to zero to arrive at a maximum wall heat flux.

$$q_{cold} = h(T_{dc})[T_{dc} - T_{wc}] = 1700[1630 - 1200] = 7.3\text{x}10^5 \text{ W/m}^2$$
$$q_{max} = h(T_{ad})[T_{ad} - T_w] = 1850[2350 - 1200] = 2.2\text{x}10^6 \text{ W/m}^2$$

Solving Equations 4.5a and 4.5c, gives q_{hot}=9.9x10^5 W/m^2. This analysis indicates there would be 35 percent more heat flux to the blade surface due to the presence of local reactions, and a degradation of film effectiveness from 0.4 to around 0.0-0.1 between the rows of film-cooling holes.

This type of calculation can be repeated for different blowing ratios. For example, if the blowing ratio of this row were B=0.5, the maximum increase in surface heat flux would have been roughly 40% at the midpoint between rows, and even higher further downstream. At B=2.0, which corresponds to a lifted jet, the maximum augmentation to the surface would have been roughly 30%, and the location of maximum heat flux around 5 exit diameters behind the film-cooling holes.

The sensitivity to freestream conditions can also be examined. For example, if the freestream temperature were to be varied by 100 K to 2100 K, the corresponding change in chemical time, would result in a new Da of around 10. This would change the Q_s ratio to 30%, and the calculations would lead to an augmented surface heat flux over the non-reacting conditions of 40% for B=1.0. If the level of H^* is varied the calculation of Da, and consequently Q_s, will remain the same. However, the ΔT_t, which is responsible for the changes in driving temperature, is of consequence to increases in surface heat flux augmentation to the blade. Consider the case where H^*=0.01, or a very low level of fuel is transported from the combustor exit to the turbine airfoil surface. In this case the ΔT_t is on the order of only 10 K, and the change in surface heat flux is on the order of only 2%, even at high Da.

6.2 Case Study 2: Combustor Liner Film-Cooled Surfaces

This example will proceed in the same manner as case study 1, but with different operating conditions to illustrate a larger potential change in q_{hot}/q_{cold}. Consider a film-cooled combustor liner operating at a

B=0.5, with an average film effectiveness of 0.7. Velocity in this region is 10 m/s, freestream temperature and pressure are 1800 K and 20 atm., respectively, the coolant temperature is 950K, and the wall temperature is 1200 K. A freestream with an energy equivalent of $H^*=0.25$ is present over the liner surface. In this case, the spacing is 2 cm between film-cooling holes, and the flow time over this distance is 0.002 seconds.

For these conditions, Da=20 and $\Delta T_t=300$K. From Figure 4.7, the scaled heat flux ratio is about 0.75. Given $\eta=0.7$ for this scenario, T_f is calculated from Equation 4.5 ($T_f \sim T_{dc}=1290$ K). The value of q_{cold} and q_{max} are calculated as $1.3\text{x}10^5$ W/m^2 and $1.4\text{x}10^6$ W/m^2, respectively. Solving 4.5a and 4.5c gives $q_{hot}=1.1\text{x}10^6$ W/m^2. A factor of 10 in increased heat flux over the non-reactive case would be expected due to the presence of local reactions.

In each of these two case studies, it is important to note the sensitivity of q_{hot} and q_{cold} to T_w, T_f, and T_c. As the film temperature approaches the wall temperature, q_{cold} decreases, making the denominator in the ratio of q_{hot}/q_{cold} small and the ratio of q_{hot}/q_{cold} may become large. However, the additional heat load to the film-cooled surface may not be significant in terms of ΔT_t. Therefore scaling with q_{hot}/q_{cold} can be misleading. Thus, the scaling shown in Equation 4.4 (based on percent of maximum achievable heat flux) is suggested when making comparisons between non-reactive and reactive scenarios. To estimate the severity of the impact to the film-cooled surface, B, Da, Q_s, and H^* all must be known.

6.3 Case Study 3: Fixed Cooling Geometry Airfoil Assessment and Design Improvement Suggestions

Again, consider the airfoil shown in Figure 6.1, which is also shown in a rotated view in Figure 6.2. The film-cooling performance of this airfoil can be assessed using the tools presented in Section 5.4.3. The leading edge cooling design of this airfoil features 4 rows of cooling holes with a z/D spacing of 5, x/D spacing of 3, and an alternating stagger of z/D=3 between the rows. From the numerical results, it can be expected that this level of film-cooling on the leading edge will maintain the desired film effectiveness over the surface for attached jet blowing ratios of B<1.0. The region on the blade between this leading edge cooling portion and the next row of holes at around 30 D downstream represents the areas on the blade surface that may be most susceptible to large surface heat loads. Even with attached blowing ratios of B=0.5, the scaled surface heat flux may approach its maximum value before the next row of holes. For example, at an H^* of 0.3 and Da of 20, the increases in scaled surface heat flux may be around 50-70%, leading to high augmented surface heat flux because the high fuel level would correspond to increases in driving temperature of over 300K.

The multiple row film-cooling studies performed in the numerical investigation suggest that this blade surface could be made more robust to near-wall reactions by adding another row of film-cooling holes between the leading edge cooling and the subsequent row, as shown in Figure 6.2. If the blowing ratio of the leading edge holes were kept around 0.5, this geometry would keep the film effectiveness above 0.2 for

$H^* < 0.15$. If the entire surface of the blade needed to be kept at a film effectiveness higher or lower than this value, the results of the computation tool shown in Figure 5.10 could be used to develop such a scheme.

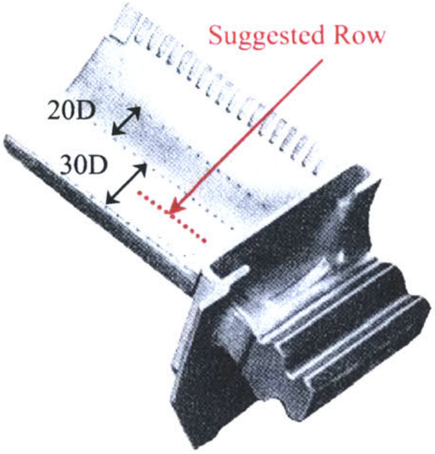

Figure 6.2: Sample Film-Cooled Airfoil with Leading Edge Detail

Finally, it should be mentioned that many assumptions, such as neglecting the effect of surface curvature on heat transfer coefficient or neglecting end-wall effects, have been made. The results of research into such areas can however readily fit into the governing non-dimensional parameters outlined in this thesis to capture more realistic turbine flow field effects. For example, Q_s versus Da plots, such as those shown in Figure 4.8, could be obtained for pressure and suction sides of an airfoil.

Chapter 7

Summary, Conclusions, and Recommendations

As the equivalence ratios within modern combustors increase, the potential for reactive species to interact at downstream film-cooled locations must be taken into account during the design of gas turbine engines. Experimental and numerical studies of the changes in surface heat transfer due to the interaction of a fuel-rich freestream with a film-cooling layer have been completed. The studies included evaluations of the changes in film effectiveness, convective heat transfer coefficient, and surface heat flux over a range of blowing parameters, flow and chemical times scales, and freestream fuel concentrations relevant to advanced gas turbines. A set of governing non-dimensional parameters was established which can be utilized to analyze changes in turbine surface heat load under conditions associated with combustor inefficiency and unmixedness. The utility of these tools was evaluated through their application to the design and assessment of film-cooled surfaces in the presence of near-wall reactions.

7.1 Conclusions

Several conclusions can be drawn from the work presented here.

1. *The impact of near-wall, secondary reactions on a film-cooled surface is primarily a function of 5 non-dimensional groupings: The Damköhler number (Da), heat release potential (H^*), scaled heat flux (Q_s), and mass and momentum blowing ratios (B and I).* The scaled heat flux ratio always increases with Damköhler number and depends on the structure of the cooling jet (B and I), but is not a function of the freestream fuel energy content, H^*. To estimate the severity of the impact to the film-cooled surface, B, Da, Q_s, and H^* must be known. The newly developed scaled heat flux ratio, Q_s, is the appropriate way to make comparisons between non-reactive and reactive scenarios, rather than simply the ratio of reactive to non-reactive quantities.
2. *Transient shock tube experiments can be employed to make accurate surface heat flux measurements on a fuel-rich freestream interacting with a film-cooling layer.* For example, the data indicate that the scaled heat flux, Q_s, increases with increasing Damköhler number to a value of around 80% at Da=30 for B=0.5 and H^*=0.3. Such conditions lead to a degradation in film effectiveness from 0.5 to around -0.6 at downstream locations between 10 and 20 x/D.
3. *A numerical model was able to capture the critical features of near-wall reactions over a range of conditions relevant to turbine design.* For example, numerical reacting flow studies were performed demonstrating that for attached jets the location of greatest surface heat flux augmentation occurs for x/D>10, at z/D=±1. For lifted jets, increased heat load is concentrated

between $3<x/D<10$ on the centerline. The film effectiveness degrades significantly in the presence of local reactions, and in certain cases may become negative.

4. *The numerical models can be useful for turbine film-cooling analysis of current geometries under reactive conditions.* The numerical models provided insight into film-cooled surface designs that are more robust to near-wall reactions. For example, lateral ($z/D=3$), downstream ($x/D=10$), and staggered hole spacings ($z/D=3$) may be arranged such that the average film effectiveness of the surface will be kept above 0.2 for fuel energy contents of $H^*<0.15$.
5. *Augmentations in surface heat flux due to near-wall reactions are well represented by an increase in the driving temperature, ΔT_b, related to that level of surface heat flux.* The levels of increased heat flux to a surface may be modeled as a convective heat transfer coefficient times the difference in driving (or film temperature) and the wall temperature. The levels of driving temperature at high Da conditions may approach that of the adiabatic flame temperature, corresponding to nearly a maximum in scaled heat flux. The changes in surface heat flux attributable to changes in convective heat transfer coefficient are much smaller than those associated with increased driving or film temperature.

7.2 Recommendations

The experimental and numerical efforts of this thesis have taken some first steps toward understanding, predicting, and designing for near-wall reactions on film-cooled components. This section outlines some of the tasks for future work.

7.2.1 Study of Alternate Cooling Schemes and Geometries

Future computational studies should focus on multiple row and staggered hole cooling geometries to examine how well single hole results extend to such configurations. Slot film-cooling also represents a method for keeping the surfaces of film-cooled components completely separated from reactive gases, and should be investigated. The broad literature base on shaped holes, compound holes, etc., could be extended to provide a data base which accounts for near-wall reactions on downstream film effectiveness. Additionally, heat loads downstream of backward facing step geometries, such as those of Reference [22], should be explored computationally and experimentally in the presence of a fuel-rich freestream. Local reactions near step and recirculation zones, where τ_{flow} is very large, may exhibit substantially different behavior as compared to the single film-cooling hole studies. Such experimental work should be compared to the results from this thesis. Curved surfaces in adverse and favorable pressure gradients should also be examined experimentally, such as was performed for non-reactive cases in Reference [30], to quantify these effects on the proposed governing parameter set.

7.2.2 Unsteady and Rotational Effects

The results described in this thesis, both experimental and numerical, are for steady flows in a non-rotating environment. The influence of unsteadiness, may result in redefining the Damköhler number to be consistent with the fluid time scales associated with the unsteady flow field. Furthermore, the scaled heat flux ratio may need to be defined for transient heat loads to the surface. The effects of rotation should also be explored, as the heat flux to the surface may be altered in the rotating environment [57]. The change in heat transfer coefficient may be corrected for in the definition of the scaled heat flux for these unsteady or rotating environments.

7.2.3 Improvements in Numerical Simulation

Several improvements could be made to the numerical tool including additions to the computational domain and the reaction mechanism. For example, a more representative plenum geometry could be included to more accurately model the incident cooling flow field. The single-step chemical mechanism could be replaced with an improved mechanism for various hydrocarbon fuels that are found in combustor exhaust flows. Such improvements in the details of the chemical kinetics would come at a computational cost relative to the simple one-step scoping tool. If sufficient agreement was found between the two cases, the tool could be used for broad sweeps of the design space, and then more accurate computations for studying particular details of the flow-chemistry interaction could be performed. A grid that simulates the curved surfaces of a turbine airfoil could also be used to investigate the effects of surface curvature on heat transfer results.

7.2.4 Development of Reactive Film Layer Correlations

Analytical correlations for film effectiveness from multiple rows of cooling holes have been developed and successfully used for predictive capabilities, such as those found in Reference [22]. Similar correlations might be developed for reactive cases and a preliminary method for doing so, incorporating the Da and H^*, is under development. More work in this area would lead to analytical expressions that could be used to predict the film effectiveness over a range of the relevant parameters.

7.2.5 Integration of the Results with Modern Design Codes

The final step should be to integrate the results of this study into modern film-cooling design. Data scaling methods, such as by film effectiveness versus downstream and lateral distance, should be readily adaptable since modern methods already employ such correlations. Initially, it is proposed that examples such as those shown in the case studies of Chapter 6 would serve as a complement to current design systems, providing designers with insight into such phenomena and eventually their potential utility should be integrated with the complete system.

Bibliography

1. Ammari, H.D., Hay, N., and Lampard, D., "The Effect of Density Ratio on the Heat Transfer Coefficient from a Film-cooled Flat Plate." ASME 89-GT-176.
2. Behbahani, A.I., and Goldstein, R.J., "Local Heat Transfer to Staggered Arrays of Impinging Circular Air Jets." ASME 82-GT-211.
3. Bowman, C.T. Hanson, R.K., Davidson, D.F., Gardiner, W.C., Jr., Lissianski, V., Smith, G.P., Golden, D.M., Frenklach, M., and Goldenberg, M., 1995, "GRI-Mech 2.11, http://www.me.berkeley.edu/gri_mech/."
4. Brodkey, R.S., "Fluid Motion and Mixing." Chapter 2.
5. Butler, T.L., Sharma, O.P., Joslyn, H.S. and Dring, R.P., "Resdistribution of an Inlet Temperature Distortion in an Axial Flow Turbine Stage." AIAA-86-1468, presented at the AIAA/ASME/SAE/ASEE 22nd Joint Propulsion Conference, Huntsville, Alabama, June 1986.
6. Dorney, D.J., and Gundy-Burlet, K., "Hot-Streak Clocking Effects in a 1-1/2 Stage Turbine." Journal of Propulsion and Power. Colume 12, Number 3, Pages 619-620.
7. Dorney, D.J., and Gundy-Burlet, K., and Sondak, D.L., "A Survey of Hot Streak Experiments and Simulations."
8. Dorney, D.J., Davis R.L., and Edwards, D.E., "Investigation of Hot Streak Migration and Film-cooling Effects on Heat Transfer in Rotor/Stator Interacting Flows." United Technologies Research Center Report 91-29, April 1992.
9. Emmons, H.W. "The Film Combustion of Liquid Fuel." Zeitschrift fur Angewandte Mathematic und Mechanik 36:1-2. Pp. 60-71. 1956.
10. Eckert, E.R.G., Goldstein, R.J., Patankar, S.V., and Simon, T.W., "Studies of Gas Turbine Heat Transfer: Airfoil Surfaces and End-Wall Cooling Effects." AFOSR-TR-91-0954.
11. Epstein, A.H., Guenette, G.R., Norton, R.J.G., and Yuzhang, C., "High-Frequency Response Heat-Flux Gauge." Review of Scientific Instruments, Vol. 57, No. 4, April 1986.
12. Fotache, C.G., Wang, H., and Law, C.K., 1999, "Ignition of Ethane, Propane, and Butane in Counterflow Jets of Cold Fuel versus Hot Air Under Variable Pressures," Combustion and Flame, 117, pp. 777-794.
13. Fric, T.F., 1993, "Effects of Fuel-Air Unmixedness on NO_x Emissions, Journal of Propulsion and Power, 9(5), pp. 708-713.
14. Godin, Th, Harvey, S., and Stouffs, P., 1997, "Chemically Reactive Flow of Hot Combustion Gases In An Aircraft Turbo-Jet Engine," 97-GT-302, Presented at the International Gas Turbine & Aeroengine Congress and Exhibition, Orlando, FL.

15. Goebel, S.G., Abuaf, N., Lovett, J.A., and Lee, C.P., "Measurements of Combustor Velocity and Turbulence Profiles."
16. Goldstein, R. J., "Film-cooling." Advances in Heat Transfer, Academic Press, Vol 7, pp. 321-379.
17. Goldstein, R.J., Eckert, E.R.G., and Ramsey, J.W., "Film-cooling with Injection Through Holes: Adiabatic Wall Temperatures Downstream of a Circular Hole."ASME 68-GT-19.
18. Gordon, S., and McBride, B. J., 1994, ``Computer Program for Calculation of Complex Chemical Equilibrium Compositions and Applications I. Analysis,''. NASA-RP-1311, NASA Glenn Research Center, Cleveland, Ohio.
19. Graf, M.B., "Investigation of the Effects of Inlet Radial Temperature Distortion on Turbine Heat Transfer." Master's Thesis, Department of Mechanical Engineering, Massachusetts Institute of Technology, May 1993.
20. Gundy-Burlet, K.L. and Dorney, D.J., "Three-Dimensional Simulations of a Hot Streak Clocking in a 1-1/2 Stage Turbine." AIAA 96-2791, 32nd AIAA/ASME/SAE/ASEE Joint Propulsion Conference. Lake Buena Vista, FL, July 1-3.
21. Haldeman, C.W., "An Experimental Study of Radial Temperature Profile Effects on Turbine Tip Shroud Heat Transfer." Master's Thesis, Department of Aeronautics and Astronautics, Massachusetts Institute of Technology, 1989.
22. *Handbook of Heat Transfer Applications*, 2nd ed., McGraw-Hill, New York, NY, 1985.
23. Harasgama, S.P., "Combustor Exit Temperature Distortion Effects on Heat Transfer and Aerodynamics within a Rotating Turbine Blade Passage." ASME Paper 90-GT-174, June 1990.
24. Harnett, J.P., *Chapter 1: Mass Transfer Cooling,* In Rohsenow, W.M., Hartnett, J.P., Ganic, E.N., eds., 1985, Handbook of Heat Transfer Fundamentals, McGraw-Hill, New York, N.Y.
25. Hermanson, J.C. and Dimotakis, P.E., "Effects of Heat Release in a Turbulent, Reacting Shear Layer." Journal of Fluid Mechanics, Vol. 199, pp. 333-375. 1989.
26. Heywood, J.B., and Mikus, T., 1973, "Parameters Controlling Nitric Oxide Emissions from Gas Turbine Combustors, Paper 21, Presented at AGARD Propulsion & Energetics Panels 41st Meeting on Atmospheric Pollution by Aircraft Engines, London, England.
27. Howard, R.P., *et al.*, 1996, "Experimental Characterization of Gas Turbine Emissions at Simulated Flight Altitude Conditions," AEDC-TR-96-3, Arnold Engineering Development Center, Arnold Air Force Base, Tennessee.
28. International Civil Aviation Organization. 1995, "ICAO Engine Exhaust Emissions Data Bank," First Edition With Addendums, ICAO Doc 9646-AN/943. Montreal, Canada.
29. Kee, R.J., Rupley, F.M., and Miller, J.A., 1991, "CHEMKIN-II: A FORTRAN Chemical Kinetics Package for the Analysis of Gas-Phase Chemical Kinetics," SAND89-8009, Sandia National Laboratories, Livermore, California.
30. Kercher, D. M., "Short Duration Heat Transfer Studies at High Free-Stream Temperatures," ASME, 82-GT-129.

31. Keyes, W.M., and Crawford, M.E. 1980, *Convective Heat and Mass Transfer*, McGraw-Hill Book Company, New York.
32. Kirk, D. R., Aeroacoustic Measurement and Analysis of Transient Hot Supersonic Nozzle Flows. Master's Thesis, Massachusetts Institute of Technology, 1999.
33. Kirk, D.R., Guenette, G.R., Lukachko, S.P., and Waitz, I.A., 2002, "Turbine Durability Impacts of High Fuel-Air Ratio Combustors, Part 2: Impact of Intra-Turbine Heat Release on Film-Cooled Surface Heat Transfer," GT-2002-30182, Presented at ASME Turbo Expo 2002: Land, Sea & Air, Amsterdam, The Netherlands.
34. Krouthen, B., and Giles, M.B., "Numerical Investigation of Hot Streaks in Turbines," AIAA Paper 88-3015, 1988, Boston, MA.
35. Kundo, K.M., Banerjee, D., and Bhaduri, D., "On Flame Stabilization by Bluff Bodies." Journal of Engineering for Power, Vol. 102, pp. 209-214. January 1980.
36. Kuo, K.K., "Principles of Combustion." 1986.
37. L'Ecuyer, M.R., "A Model for Crrelating Flate Plate Film-cooling Effectiveness Data for Rows of Round Holes." ME-TSPC-TR-85-11. June 1985.
38. Lakshminarayna, B., 1996, *Fluid Dynamics and Heat Transfer of Turbomachinery*, J. Wiley, New York, N.Y.
39. Lukachko, S.P., et al, "Turbine Durability Impacts of High Fuel-Air Ratio Combustors, Part 1: Potential For Intra-Turbine Oxidation of Partially-Reacted Fuel," GT-2002-30077. Presented at ASME Turbo Expo 2002: Land, Sear & Air, Amsterdam, The Netherlands.
40. Lukachko, S.P., Waitz, I.A., Miake-Lye, R.C., Brown, R.C., and Anderson, M.R., 1998, "Production of Sulfate Aerosol Precursors in the Turbine and Exhaust Nozzle of an Aircraft Engine," Journal of Geophysical Research, 103(D13), pp. 16159-16174.
41. Metzger, D.E., and Mayle, R.E., "Gas Turbine Heat Transfer." Mechanical Engineering Magazine, Vol. 105, 6, pp. 44-52, 1983.
42. Mikus, T. and Heywood, J.B., 1971, "The Automotive Gas Turbine and Nitric Oxide Emissions," Combustion Science and Technology, 4, pp. 149-158.
43. Pappas, G., "Influence of Inlet Radial Temperature Distortion on Turbine Rotor Heat Transfer." Master's Thesis, Massachusetts Institute of Technology, August 1990.
44. Paxson, D. E., and Mayle, R. E., "The Influence of a Mainstream Thermal Boundary Layer on Film Effectiveness." Journal of Turbomachinery, October 1989. Vol 111, pp. 491-496.
45. Penner J.E., Lister, D.H., Griggs, D.J., Dokken, D.J., and McFarland, M., eds., 1999, *Special Report on Aviation and the Global Atmosphere*, IPCC, WMO/UNEP, Cambridge University Press, Cambridge, U.K.
46. Pietrzyk, J.R., Bogard, D.G., and Crawford, M.E., "Effects of Density Ratio on the Hydrodynamics of Film-cooling." ASME 89-GT-175.

47. Prasad, D., and Hendricks, G.J, "A Numerical Study of Transport Mechanisms in Axial Flow Turbomachines with Application to Radial Transport of Hot Streaks." UTRC Report R99-1.114.9801, February 1999 and also presented at ASME IGTI Turbo Expo 2000. Munich, Germany, May 8-11.
48. Roback, R.J. and Dring, R.P., "Hot Streaks and Phantom Cooling in a Turbine Rotor Passage Part 1: Separate Effects." ASME Paper 92-GT-75.
49. Roback, R.J. and Dring, R.P., "Hot Streaks and Phantom Cooling in a Turbine Rotor Passage Part 2: Combined Effects and Analytical Modeling." ASME Paper 92-GT-75.
50. Rohmat, T.A, Katoh, H., Obra, T., Yoshihashi, T, and Ohyagi, S., "Diffusion Flame Stabilized on a Porous Plate in a Parallel Airstream."
51. Rolls-Royce, plc., 1992, *The Jet Engine*, 4th Edition, Derby, England.
52. Schultz, D.L. and Jones, T.V., "Heat-Transfer Measurements in Short-Duration Hypersonic Facilities," AGARD No. 165. 1973.
53. Schultz, D.L., and Jones, T.V., "Heat-Transfer Measurements in Short-Duration Hypersonic Facilities.", AGARDograph No. 165. AGARD-AG-165. 1973.
54. Schwab, J.R., Stable, R.G., and Whitney, W.J., "Analytical and Experimental Study of Flow Through an Axial Turbine Stage With a Nonuniform Inlet Radial Temperature Profile." NASA Technical Memorandum 83431, AIAA-83-1175.
55. Seller, J.P., "Gaseous Film-cooling With Multiple Injection Stations." AIAA Journal. Vol. 1, 9, pp. 2154-2156. 1963.
56. Seochting, Frederick. Personal Communication. June, 2002.
57. Shang, T., "Influence of Inlet Temperature Distortion on Turbine Heat Transfer." Doctoral Thesis, Massachusetts Institute of Technology, February 1995.
58. Sinha, A.K., Bogard D.G., and Crawford, M.E., "Film-cooling Effectiveness Downstream of a Single Row of Holes with Variable Density Ratio." ASME 90-GT-43.
59. Sirignano, W.A. and Kim, I., "Diffusion Flame in a Two-Dimensional, Accelerating Mixing Layer." Physics of Fluids, Vol. 9, Septemeber 1997.
60. Sirignano, W.A. and Liu, F., 1999, "Performance Increases for Gas-Turbine Engines Through Combustion Inside the Turbine," Journal of Propulsion and Power, 15(1), pp. 111-118.
61. Sturgess, G.J., McKinney, R., and Morford, S., 1992, "Modification of Combustor Stoichiometry Distribution for Reduced NO_x Emission from Aircraft Engines," 92-GT-108, Presented at the International Gas Turbine and Aeroengine Congress and Exposition, Cologne, Germany.
62. U.S. Environmental Protection Agency, 1992, "Procedures for Emission Inventory Preparation: Volume IV, Mobile Sources," EPA420-R-92-009, Washington, D.C.
63. Vidal, R.J., "Model Instrumentation Techniques for Heat Transfer and Force Measurements in a Hypersonic Shock Tunnel." Cornell Aeronautical Laboratory, Inc. Contract No. AF33(616)-2387, Report No. AD-917-A-1. February 1956.

64. Walters, D.K. and Leylek, J.H., "A Detailed Analysis of Film-Cooling Physics: Part 1 – Streamwise Injection With Cylindrical Holes," ASME. Vol. 122. January 2000.
65. Walters, D.K. and Leylek, J.H., "A Systematic Computational Methodology Applied to a Three-Dimensional Film-Cooling Flowfield," Journal of Turbomachinery. Vol. 119, 777-785. October 1997.
66. Wey, C.C., *et al.*, 1998, "Engine Gaseous, Aerosol Precursor and Particulate at Simulated Flight Altitude Conditions," NASA-TM-1998-208509, NASA Glenn Research Center, Cleveland, Ohio.
67. White, F.M., *Viscous Fluid Flow*, McGraw-Hill Book Company, Boston. 1991.
68. Zukoski, E.E and Marble, F.E., "Experiments Concerning the Mechanism of Flame Blowoff From Bluff Bodies." Proceedings of the Gas-Dynamics Symposium on Thermochemistry, Northwestern University, Evanston, Illinois, 1956.
69. http://www.soton.ac.uk/~genesis/Misc/Refpic.htm

Appendix A

Mixing of Fuel-Rich Streaks En Route to Downstream Turbine Surfaces

Low mixedness is manifest at the combustor exit by spatial non-uniformities in fuel-air ratio. As a result of low mixedness, and in contrast to the emission of CO or HC resulting from inadequate residence time, some portion of the flow will be characterized by a greater than stoichiometric composition. In time, these spatial non-uniformities are emitted into the gas path as streaks. These streaks can transport energetic emissions downstream of the combustor where, mixing with oxygen-rich film-cooling or purge flows, stoichiometric combustion can occur somewhere in the interaction. Streaks that carry lean mixtures will be further diluted at the site and are relatively less consequential, both because of the reduced opportunity for reaction and the diminished impact of the subsequent heat release. It can be expected that upon emission, a fuel-rich streak would abut other regions of the exit flow that are lean. The fate of the streak, whether a portion of the streak survives the transit, depends on the scale of the non-uniformity as well as the relative mixing, convective, and chemical time scales.

The importance of a particular non-uniformity is determined by the definition of a minimum scale, representing the smallest streak that survives a single, representative HPT stage. Two simplified mixing models were employed to measure the extent of mixing in transit, a diffusive transport analysis governed by turbulence levels, and the development of a shear layer due to a velocity differential. The resulting estimates were used to define τ_{mix}/τ_{conv}. If τ_{mix}/τ_{conv} is greater than one, some portion of the streak will arrive unperturbed. If oxidation reactions are slow, such that Da, defined by the reaction time and appropriate convective scale, τ_{conv}/τ_{reac}, is small, some of the partially reacted fuel in the mixed-out region may also survive.

Turbulent diffusion is one of the primary mechanisms through which a streak is mixed with adjacent flow. The temperature ratio of the streak to adjacent flow is taken to be unity and thus the density and velocity ratios are also taken to be unity. Under the assumption of isotropic turbulence with no cross velocities, no shear stresses form and thus, no shear layer develops. Additionally, no superimposed molecular diffusion is employed as it is assumed that the turbulence is dominant. In the manner shown in Figure A.1, the diffusion, or mixing time, τ_{mix}, is defined as the time that it takes for a parcel of fluid at the outside of the reactive streak to diffuse to the centerline of the streak.

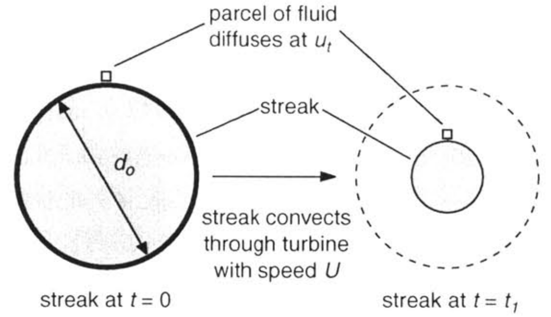

Figure A.1: Turbulent Diffusive Mixing Model

An estimate for τ_{mix} is dependent on the diffusion velocity (V_d) which is related to the turbulent diffusivity (D_t) by analogy to the equation for Fickian diffusion:

$$Y\vec{V}_d = -D_t \nabla Y \approx -D_t \left(-\frac{2Y}{d_o} \right) \qquad \text{A.1}$$

For turbulent diffusion, V_d is approximately the turbulent velocity, u_t. The turbulent velocity is estimated from typical levels of turbulent intensity ($u'/U = 0.1\text{-}0.15$) at the combustor exit. Using the assumption of homogenous isotropic turbulence, $u'=v'=w'$, the turbulent velocity is estimated from the turbulent intensity as approximately u', since:

$$u_t = \sqrt{\frac{u'^2 + v'^2 + w'^2}{2}} = \sqrt{\frac{3u'^2}{2}} = 1.2u' \approx u' \qquad \text{A.2}$$

This gives a conservative definition for the mixing time:

$$\tau_{mix} \approx \frac{d_o}{2u_t} \qquad \text{A.3}$$

If $\tau_{mix} < \tau_{flow}$ the hot streak will mix out prior to arrival at a turbine event site, or in this approximation will react prior to arriving at a turbine event site provided $\tau_{chem} << \tau_{flow}$ or τ_{mix}.

Streak parameters such as temperature, pressure, position, and time were taken from streamlines calculated for a current era advanced engine. Typical levels of turbulent intensity, u'/U_∞, range from 5-30%, with typical values around 15% [15]. In this study, the turbulent intensities were varied from 5-50% of the freestream velocity and a range of streak diameters from 5-50% of the combustor exit span was considered. Results indicated that streaks larger than ~5% of span will not have sufficient time to mix out over the length scale of a turbine stage. The same approach can be used on other downstream components. This method is not designed to be an inclusive way to predict whether or not a fuel-rich or hot streak will be detrimental to a downstream film-cooled component, but rather to provide some rough guidelines that may suggest that certain streak sizes exiting the combustor may be more benign that others because of the possibility of them mixing-out and reacting with the freestream, prior to arriving at a potential turbine event site. Such a concept is closely linked to methods of turbine stage clocking, which have the added benefit of helping to break-up larger streaks from the combustor prior to entering the turbine [20]. For this study, an improved Taylor diffusion mixing model was also employed, which is summarized in Reference [4], and showed agreement with the simplified expression to within 5% for all cases studied.

In addition to the turbulent diffusive mixing, the development of a shear layer between the streak and the adjacent flow also provides a potential mixing mechanism. Different velocities will result from different stream temperatures. Analytical distributions of velocity and pressure for a 2-D, turbulent shear layer between two co-flowing streams of different velocities and temperatures were employed for the analysis, where the velocity anywhere in the shear layer is given by:

$$u = \frac{U_1 + U_2}{2}\left(1 + \frac{U_1 - U_2}{U_1 + U_2}\operatorname{erf}\left(\sigma \frac{y}{x}\right)\right) \qquad \text{A.4}$$

The value of the spreading parameter, σ, is taken to be about 13 for typical shear layers. Temperature differences were derived from typical combustor exit profiles. The temperature difference leads to the velocity non-uniformity between the cold and hot streams, either of which may carry energetic emissions. The definition of τ_{mix} in this case is conservatively defined as the time required for the velocity at the centerline of the streak to slow down by 1%. This is essentially a criterion for the penetration of the shear layer to the center of the streak.

The shear mechanism provides a more vigorous mechanism for mixing than diffusive turbulence. Over the length of a turbine stage, and for a range of velocity ranges, it was found that reactive streaks larger than ~10% of span do not have time to fully mix with the surrounding flow. Thus, in the limit of fast chemistry, $\tau_{conv}/\tau_{reac} >> 1$, some amount of energetic emissions can survive through the HPT unmixed.

For reference, Table A.1 presents a summary of the current literature and relevant parameters associated with hot streak development and transport from the combustor exit and behavior into and through the turbine.

Table A.1: Hot Streak Literature Review Summary

Source/Paper and Author	**Contents**	**Relevance and Pertinent Data**
Measurements of Combustor Velocity and Turbuelence Profiles, S.G. Goebel, N. Abuaf, J.A. Lovett, and C.P. Lee, [15]	Provides realistic exit level axial velocity, axial turbulence intensity, swirl velocity, swirl turbulence intensity and temperature profiles from a model combustor.	Figure 4: Low Swirl Case. U = 93 ft/s (28.3 m/s), mass flow = 0.5 lbm/s (0.23 kg/s), Tad = 1980 F (1355 K), P = 6.8 atm., axial turbulent intensity (u'/U) 0.07-0.12, swirl velocity ~ 1.5 m/s, swirl turbulent intensity (v'/U) 0.06 - 0.10 Figure 5: High Swirl Case. U = 174 ft/s (53 m/s), mass flow = 1.0 lbm/s (0.45 kg/s), Tad = 1980 F (1355 K), P = 6.8 atm., axial turbulent intensity (u'/U) 0.10, swirl velocity ~ 3 m/s, swirl turbulent intensity (v'/U) 0.08-0.10 Figure 7a: Low Swirl Case: Temperature Profile for T_{ad} = 1200 F (922 K) Temperature across exit plane varies from 840-1200 F (722-922 K) Figure 7b: High Swirl Case: Temperature Profile for T_{ad}=1800 F (1255 K) Temperature across the exit plane varies from 1640-1925 F (1167-1325 K) Note: Cases are provided in Figures 4 and 5 for Tad varying from 80 F (unfired) to 1980 F (300-1355 K) and U varying from 15-93 ft/s (4.6-28.3 m/s)

A Numerical Study of Transport Mechanisms in Axial Flow Turbines, D. Prasad, [47]	Appendix A: Effect of vane inlet nonuniformity is of particular interest. Provides an example of typical combustor exit pressure and temperature profiles for an earlier version of the F100-PW229 engine at design conditions. Data taken from experiments in a sector rig.	Figure 13: Contours of Stagnation Pressure (psi) at Combustor Exit. Mean stagnation pressure is 448 psi (30 atm), with typical values ranging from 441-449 psi (30-30.5 atm). The magnitude of the distortion in total pressure relative to the mean is approximately 5%. Figure 14: Stagnation Temperature Contours in R at the Combustor Exit. Mean stagnation temperature is approximately 3200 R (1778 K), with typical values ranging from 2400-3800 R (1333-2111 K). The magnitude of the distortion in total temperature is approximately 30%. Shows the approximate location of a hot streak at around 60% span with a temperature of around 3500 R (1940 K)
Spatial variability in temperature at combustor exit plane	Provides sample of spatial variability in temperature at combustor exit plane.	Range of combustor exit temperatures shown 1600-1900 K. Hot streak location centered at approximately 70% span of combustor exit plane at 1900 K. Radial size spans from 50-85 % span.
Redistribution of an Inlet Temperature Distortion in an Axial Flow Turbine State, T.L. Butler, O.P. Sharma, H.D. Joslyn, and R.P. Dring, [5]	Presents an experimental program aimed at determining the extent of the redistribution of an inlet temperature distortion in an axial flow turbine stage.	Combustor exit flow may have peak temperatures that are 500-1000 F (533-810 K) above the allowable metal temperature. Data obtained from actual gas turbine combustors show large variations in turbine inlet temperature. High response temperature surveys made inside a model combustor by Dills and Follansbee indicate that gas temperatures can vary spatially (and temporally) anywhere between stoichiometric and compressor discharge levels. Introduced hot streak into NGV and first blade at a temperature equal to twice the freestream. T_∞=540 F (555 K) at various spanwise locations
Hot Streaks and Phantom Cooling in a Turbine Rotor Passage (Parts 1 and 2), R.J. Roback and R.P. Dring, [48 49]	Presents experimental and analytical results demonstrating the effect of hot streak migration through the turbine. Part 2 of the paper presents some temperature numbers that are typical of gas turbine combustor exit conditions.	Average exit temperature of a typical gas turbine combustor is 3000 F (1922 K) A defective fuel nozzle can cause a stoichiometric streak at 4100 F (2533 K) If there was a dilution jet in the combustor that was not mixing out it might exit at a temperature of around 1100 F (867 K)
Analytical and Experimental Study of Flow Through an Axial Turbine Stage With a Nonuniform Inlet Radial Temperature Profile, J.R. Schwab, R.G. Stable and W.J. Whitney, [54]	Provides analytical and experimental results for a typical nonuniform inlet radial temperature profile through an advanced single-stage axial turbine. Combustor exit temperature profile was chosen to match Lewis Research Center High Pressure Facility (HPF) in terms of local to mean temperature ratio.	Figure 8: Stator Inlet Temperature Profile: Shows radial variation from 600-720 K with peak temperature occurring at approximately 50% span. Hub and end-wall temperatures are approximately 600 K. The ratio of maximum total temperature to the average total temperature was approximately 1.05, and the ratio of maximum to minimum total temperature was approximately 1.20. Figure 9: Stator Inlet Pressure Profile: Shows radial variation from 3.02-3.06 atm, essentially uniform pressure profile Note: In this experiment the exit profile as measured from the combustor is used as the inlet boundary condition to the NGV.

Appendix B

Shock Tube Operation and Wave Dynamics

The purpose of this appendix is to provide a brief overview of shock tunnel operation and the wave dynamics and the important time scales associated with conducting experiments in the facility. A detailed discussion of the gas dynamic model used to design the shock tube, as well as the effects of shock attenuation, free stream acceleration, shock-boundary layer interaction, and imperfect reflections from an end plate are addressed in Reference [32]. The basic operation of a shock tube is summarized in Figure B.1.

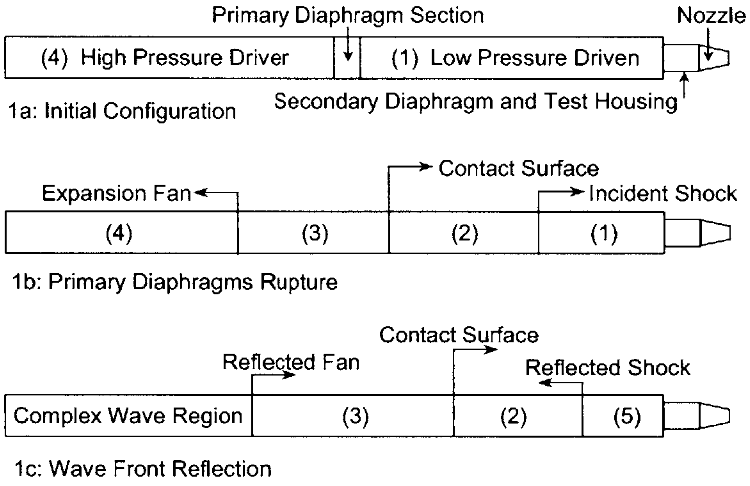

Figure B.1: Shock Tube Operation

The fundamental purpose of the shock tube is to generate a reservoir of high temperature and high pressure fluid that may be passed over the flat plate test specimen. Initially, the tube is separated into a driven section, denoted as region (1), and driver section, denoted as region (4), by two thin primary diaphragms, as shown in Figure B.1a. The driven section contains the test gas, argon or an argon-ethylene mixture for each test, and is typically evacuated to around 1/5th of an atmosphere. The driver section is evacuated and then filled with a mixture of helium and argon to a pressure between 2 and 10 atmospheres depending on the desired shock strength. A secondary diaphragm located between the driven section and the test article acts as a seal between the low pressure gas in region (1) and ambient air of the test chamber. The shock tube affords a great deal of flexibility because the driver pressure, gas composition, and the test gas pressure can be easily and accurately regulated to yield different stagnation temperatures and pressures behind the reflected shock.

When the section of the tube between the two primary diaphragms is evacuated, the pressure difference causes the diaphragms to rupture. The driver gas acts like an impulsively started piston initiating a series of converging compression waves. The compression fronts rapidly coalesce into a shock wave, propagating through the driven section, accelerating and heating the driven gas. Concurrently, a series of diverging expansion waves propagate through the driver gas mixture decreasing the pressure and accelerating the fluid in the direction of the nozzle. The state of the gas which is traversed by the incident shock wave is denoted by region (2), and that of the gas traversed by the expansion fan is denoted as region (3), as depicted in Figure B.1b. The interface, or contact surface, between regions (2) and (3) marks the boundary between the gases which were initially separated by the diaphragm. To first approximation, regions (2) and (3) can be assumed not to mix and are perpetually separated by the contact surface, which is analogous to the face of the piston. The test is initiated when the incident shock wave reaches the nozzle-end of the tube, reflects from the end-plate, and creates a region of stagnant, high-pressure, high-enthalpy fluid, denoted as region (5), which then ruptures the secondary diaphragm and expands to the desired conditions.

On either side of the contact surface it is essential that the speeds of sound between regions (2) and (3) are identical to prevent extraneous waves from the reflected shock as it passes through the contact surface. These waves may substantially limit the available test time.[8] To ensure that this does not occur, the speed of sound is matched by choosing the appropriate composition of gases for the driver section, using the matching condition:

$$\frac{\gamma_2}{a_2^2}\left[(\gamma_2+1)\frac{p_5}{p_2}+\gamma_2-1\right]=\frac{\gamma_3}{a_3^2}\left[(\gamma_3+1)\frac{p_5}{p_2}+\gamma_3-1\right] \tag{B.1}$$

The shock strength can be determined using the basic shock tube equation which relates the shock strength, p_2/p_1, implicitly as a function of the known diaphragm pressure ratio, p_4/p_1:

$$\frac{P_4}{P_1}=\frac{P_2}{P_1}\left[1-\frac{(\gamma_4-1)(a_1/a_4)(P_2/P_1-1)}{\sqrt{2\gamma_1}\sqrt{2\gamma_1+(\gamma_1+1)(P_2/P_1-1)}}\right]^{-2\gamma_4/(\gamma_4-1)} \tag{B.2}$$

Once the shock strength is determined, all other flow quantities can be determined from normal shock relations, and thus the thermodynamic and fluid mechanic properties of the stagnation region (5) are predicted.

The time-distance history of the wave system within the shock tube is illustrated in Figure B.2. The duration of steady flow through the test section is limited by either exhaustion of the test gas or the subsequent arrival of a reflected wave at the nozzle. Time, τ_1, represents the duration of the test being limited by a reflection from the contact surface. As was discussed above, this is eliminated by matching the speeds of sound in the gases to allow the reflected shock to pass undisturbed through the interface. Time, τ_{wave}, represents the duration of the test being limited by a secondary expansion (either the arrival of the

---

[8] As discussed in Section 3.2.1, it is for this reason that hydrogen can not be used as a freestream fuel for these experiments.

reflected head of the primary expansion or the arrival of a weak secondary expansion generated if the reflected shock overtakes the tail primary expansion fan). The maximum test duration for a given geometry and temperature ratio occurs when the reflected shock simultaneously intersects the reflected head and tail of the expansion fan.

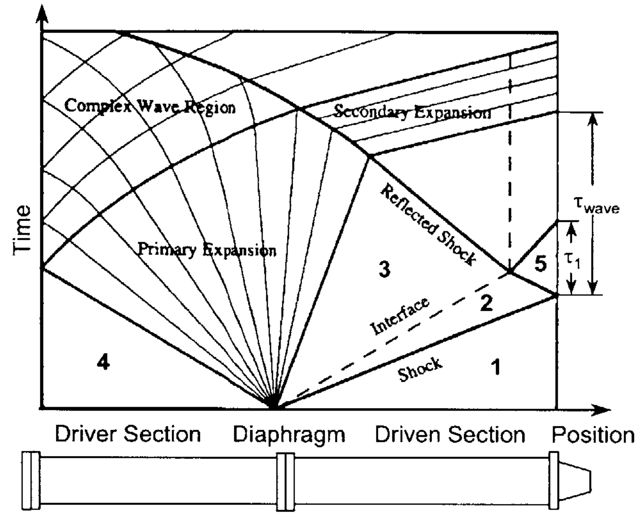

Figure B.2: Shock Tune Operational Wave Diagram

Provided the tailoring condition is met, the test time will be limited by the shorter of two time constraints: 1) the arrival of a reflected wave disturbance, or 2) the exhaustion of the available test gas. The wave impingement time at the nozzle, τ_{wave}, is a function of tube geometry and the total temperature ratio. The time to exhaust the test gas, τ_{exg}, is a function of the total temperature ratio, the size of driven section and nozzle throat area. From each of these two time constraints it is necessary to subtract the sum of the nozzle starting and jet development time to arrive at the net test time, τ_{net}. The nozzle starting time, τ_{nozzle}, is the time it takes to have started flow through the test section and nozzle, and is conservatively estimated as 3 nozzle flow-through times, varying with the total temperature ratio. For each of the tests shown in Table 3.1, the net test time is not limited by the exhaustion of the test gas, but rather by a reflected wave disturbance. However, as was discussed in Section 3.2.1, this experimental test time is still much longer than the time for chemical completion for all test cases.

Appendix C

Flat Plate Test Article and Associated Hardware Drawings

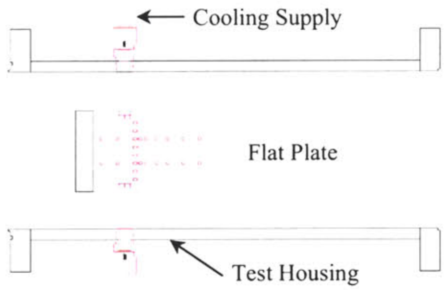

Top View

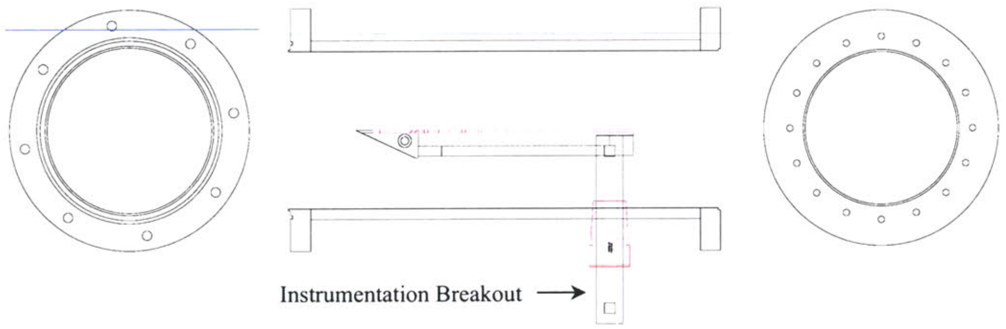

Side View

Figure C.1: Top and Side Views of Flat Plate and Test Housing Assembly

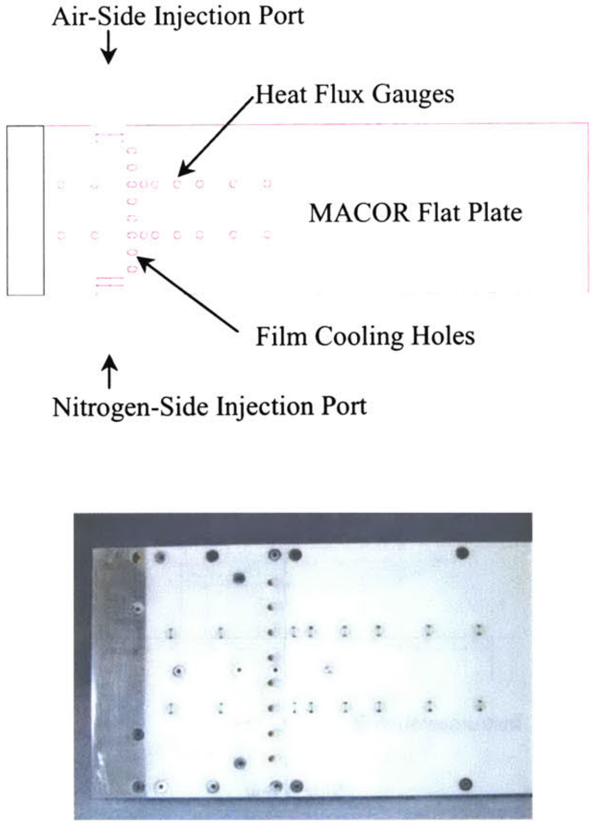

Figure C.2: Flat Plate Test Article Details

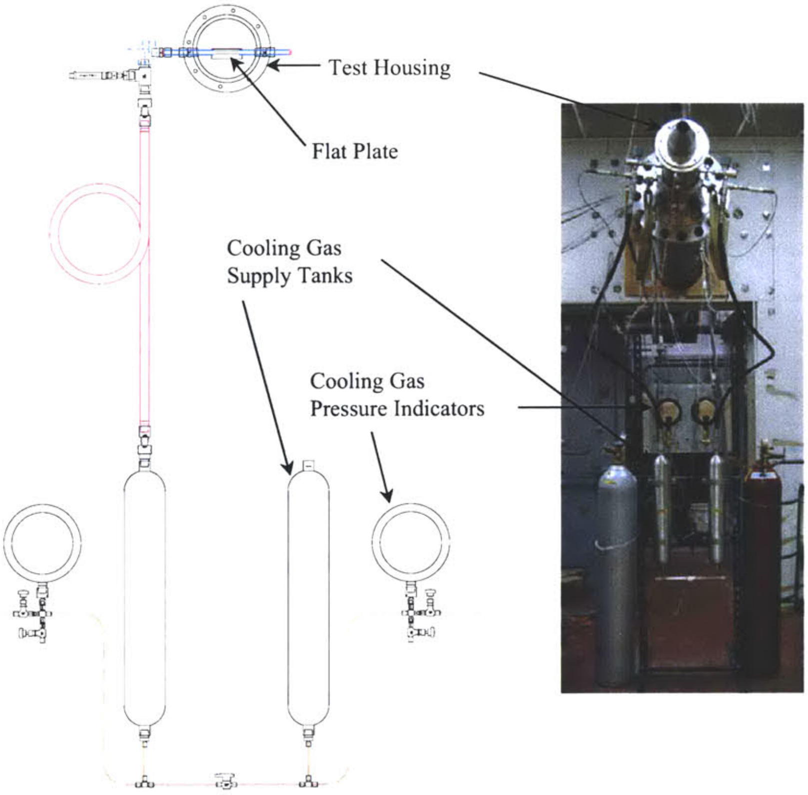

Figure C.3: Film-Coolant Supply System Details

Appendix D

Heat Transfer Gauge Fabrication Process

The passive resistive element heat flux gauges discussed in Chapter 3 were developed specifically for this experiment. The gauges had to be able to survive the harsh temperatures and pressures associated with the reactive environment located just above the surface of the flat plate and have a response time that is much shorter than the duration of the experiment. A close-up picture of one of the gauges is shown below along with installation into the bottom of the test plate.

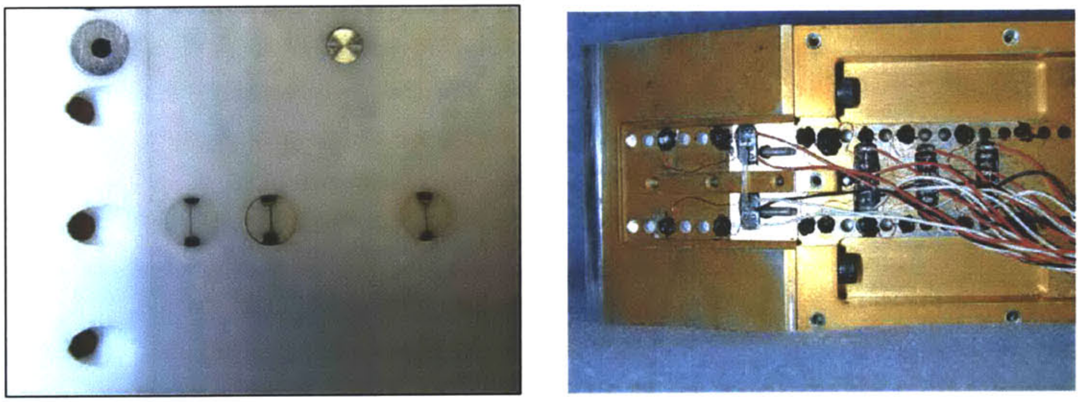

Figure D.1: Heat Flux Gauge Details

Since the process used to develop, fabricate, calibrate, and utilize these gauges was unique to this experiment, the purpose of this appendix is to formally document this process.

Machined Ceramic Glass (MACOR) Heat Transfer Gauge Fabrication Process

1. Machining: Machine pieces to correct outer diameter (O.D.). Machine correct size grooves in the sides. Recommend side-grooves be cut to a depth of 0.010 to 0.015 inches, although the deeper the groove the easier the piece will be to paint, but consequently will result in increased spacing between the side of the gauge and the piece to which it is inserted into. The grooves should be cut using an end mill of standard size of 1/32" to 3/32".
2. Post Machining Cleaning: MACOR shavings and fragments can introduce bias and error if painted into the heat transfer gauge. After machining, the gauges should be carefully rinsed under running water. Allow the MACOR pieces to dry by air-drying process or heat to slightly accelerate the drying process.

3. Sanding to Smooth Top Surface: Using a sanding bar (a block of aluminum with a perpendicular hole in it to align the gauge to the sanding surface), sand the top edge of all the MACOR pieces on 600 grit sandpaper.
4. Sanding to Round Edges: Since the sides of the gauges will serve as conductors and the top will provide temperature-based resistance, it must be ensured that any sharp corners are dulled so that in the flow of current is not inhibited. The 90 degree sharp edge between the sides and the top is such a discontinuity.
    a. Use a microscope holder to mount a gauge with the long axis pointed perpendicular to the table.
    b. Mix together in equal amounts solder flux and pumice powder in an aluminum cup until the mixture achieves a mud-like consistency.
    c. With a cotton-tipped swag, apply a drop of the solder flux-pumice powder mixture to the top of the gauge.
    d. Using a 1-2 foot piece of dental floss, work the sanding paste into the groove on each end of the top of the gauge.
    e. Vary the angle of attack of sanding to round the side-to-top interface and sand the MACOR only enough to round the edge.
    f. Only sand one end of the gauge, as this will be the end that is painted with the thin-strip to make the resistor.
5. Post Sanding Cleaning: Clean each gauge thoroughly with running water after sanding. To facilitate drying and to remove any extraneous sanding mixture, apply streams of compressed air.
6. Ultrasonic Cleaning: Place all sanded gauges into a sealed bag of Ultrasonic solution. Place in the ultrasonic cleaner for at least 30 minutes. Allow gauges to dry after removing from the Ultrasonic cleaner. Gauges can now be placed in an oven at low heat to ensure thorough drying.
7. Side Coat Painting: This is the first critical painting step.
    a. Secure a gauge in the microscope vice holder. Looking at the top of the gauge, determine if you have the correct end for painting (the edges will look rounded from sanding). If viewing is difficult, spray some degreaser or tuner cleaner on the top of the gauge to reflect light more.
    b. Once the correct end is being viewed, re-mount the gauge in the vice holder. The gauge should be held on the end opposite to the sanded end, perpendicular to the microscope field of view. At least half of the gauge should extend beyond the vice holder. Spray the gauge with tuner cleaner or degreaser to wash away dust.
    c. Using white gold paint and a small fine brush, paint one coat on the side of the gauge. Rotate the gauge 180 degrees and paint the first coat on the other side. It is important to paint completely within the machined groove, extending beyond that may introduce error into the gauge.

    d. Paint from the top of the gauge to a length of ¼" to ½". Ensure that no paint makes its way to the top of the gauge, as this will reduce the area to paint the thin film strip. If mistakes are made, use ample degreaser to wash away all paint and start again.

8. Baking: Bake gauges in a stone holder at the desired temperature (usually 800-1200 degrees F). The oven only has to reach the desired temperature for a few moments and the paint should be completely baked into the gauge. Turn the power off and begin the two hour cooling process. Allow the oven to cool down on its own for about 30 minutes; prop the door open for an additional 30 minutes; fully open the door for 45 minutes to an hour of additional cooling.

Repeat steps 7 and 8 for at least 4 coats of paint.

9. Gauge Painting (Top Thin Strip): Using a paint brush with a single hair, very carefully paint one very thin strip on the top of the gauge. This step must be done with the assistance of a microscope. Avoid drops of paint on the brush – the painting should be done very lightly and evenly. The strip should be as thin and as long as possible, spanning the entire diameter of the heat flux gauge.
10. Resistance Verification: After baking the thin strip, check the gauge resistance. Touch leads of a multimeter or Ohm meter to the sides of the gauge. Resistance should be at least 75 Ohms. Preferred range is between 100-300 Ohms.
11. Strain Gauge Bond Glue: Very lightly brush the gauge end of each piece with an even coat of strain gauge glue to protect the delicate thin film from damage and from the harsh environment that the gauges will be exposed to. Inspect the coating under the microscope to ensure that the coat is even and uniform and completely covers the resistive strip. Cure the strain gauge glue coating by baking the gauge again at 350 degrees F for 1 hour.
12. Wire Tinning: Using 36 gauge wire, first tin the ends of the wire above 750 degrees F with standard solder. Inspect the ends under the microscope to ensure a smooth finish. For the end that will attach to the gauge, trim the tinned end to approximately 25 mils. Leave the other end longer for easier mounting to solder tabs located within the device in which the gauges are to be mounted.
13. Wire Soldering: When soldering wire to the gauge, turn the soldering iron's temperature down to 640 degrees or less. Place the gauge in the vice laying flat (long axis parallel with the table) under the microscope. Coat the conductor side with solder flux. Place a small quantity of solder cream on the tinned wire. Solder the wire to the conductor side of the gauge close to the top of the gauge (e.g., at most, 1/8" from the top of the gauge). Tug gently while simultaneously inspecting the solder bond under the microscope. If the solder tab is satisfactory, clean the side of the gauge with PowerWash or another high velocity cleaner. The solder job can be checked by now verifying the resistance measurement across the wire leads using an Ohm meter.
14. Storage: Always store the gauges under clean room conditions and it is a good idea to store the gauges in a container with a lid on a bed of clean photo paper (or equivalent). Never touch the top of the gauge or allow anything to come into contact with it.

After the gauges have been constructed and verified for operation, they can be installed in the Wheatstone bridge assembly and mounted into the experiment, in this case into 16 slots on the film-cooled flat plate, as shown in Figure D.1. The gauges must next be calibrated, and this process is done using an oil bath. A sample is shown in Figure D.2.

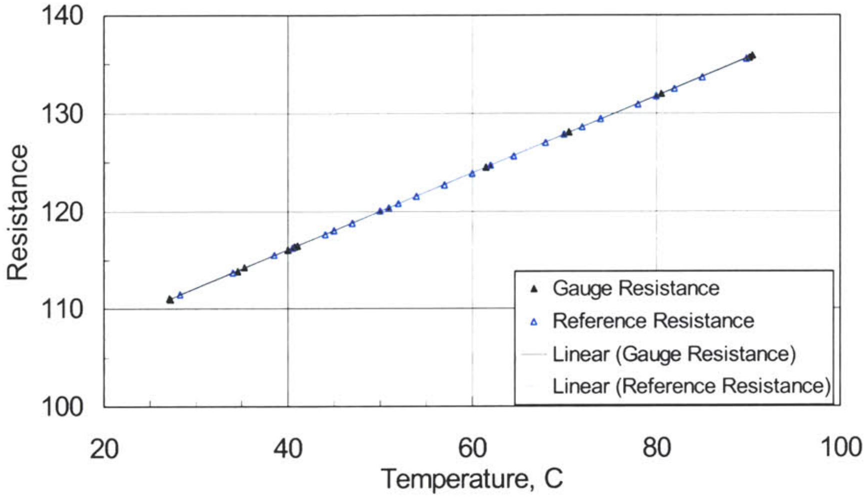

Figure D.2: Sample Heat Flux Gauge Calibration

The gauges are calibrated against a Rosemount reference thermometer which was calibrated to NIST standards. The gauge behavior shown in Figure D.2 is linear with $R^2=0.994$ over the range of temperature rise that the flat plate surface experienced during any of the tests. From this calibration curve, the resistance versus temperature behavior of each gauge can be established.

Appendix E

Heat Flux Gauge Theory and Converting of Wall Temperature vs. Time to Surface Heat Flux

The calibration curve shown in Appendix D can be used to convert the resistance versus time signal from each heat flux gauge to wall temperature versus time. This section presents the techniques used to convert wall temperature versus time to surface heat flux.

The thin-film resistance gauges measure the surface temperature of the flat plate on which they are mounted, and do not function directly as a measurement of heat transfer to the body. However, the theory for heat conduction in a non-homogeneous body can be used to relate the surface temperature history to the rate of heat transfer. In this way it is possible to measure the surface temperature history of the body and to use the heat conduction theory for the body to calculate the heat transfer rate.

The theory for heat conduction in a non-homogeneous body is based on the one-dimensional model of Reference [63] for 2 regions (ceramic MACOR cap material and an aluminum under-layment) of dissimilar thermal and physical properties. It is possible to use a one-dimensional model because the top region is thin and the edge area is an order of magnitude smaller than the planform area of the thin region. Consequently, the lateral heat flow will be correspondingly small in comparison with the longitudinal heat flow. The material of the thick sub-layer (aluminum) is assumed to be infinitely thick. For example, if the 0.2 cm thick slab of ceramic were subjected to a constant rate of heat flow for 10 ms, the temperature of the face adjacent to the aluminum sub-layer would be less than $10^{-4}\%$ of the temperature of the upper face.

For the upper region, the governing equation with domain and boundary conditions is:

Governing Equation	Domain	Boundary Conditions	
$\frac{\partial T_1}{\partial t} = k_1 \frac{\partial^2 T_1}{\partial y^2}$	$0 \le y \le l$	$t \le 0 : T_1(y) = 0$ $t > 0, y = 0 : \left(\frac{\partial T_1}{\partial y}\right)_{y=0} = -\frac{1}{k_1} q(t)$	E.1

Similarly for the aluminum sub-layer, the governing equation is:

Governing Equation	Domain	Boundary Conditions	
$\frac{\partial T_2}{\partial t} = k_2 \frac{\partial^2 T_2}{\partial y^2}$	$l \le y \le \infty$	$t \le 0 : T_2(y) = 0$ $t > 0, y = l : T_1(l) = T_2(l), k_1\left(\frac{\partial T_1}{\partial y}\right)_{y=l} = k_2\left(\frac{\partial T_2}{\partial y}\right)_{y=l}$ $\lim_{y \to \infty}, T_2 = 0$	E.2

Equations E.1 and E.2 can be solved using a Laplace transformation, and the results can be inverted to obtain solutions for the temperature. Equation E.3 gives the exact solutions for the temperatures in a semi-infinite body composed of two thermally dissimilar materials with different thermal properties:

$$T(t)=\frac{1}{\sqrt{\pi k_2\rho_2 C_{p_2}}}\int_0^t \frac{q(\lambda)}{\sqrt{t-\lambda}}d\lambda - q(t)\frac{1}{k_1}\left(\frac{k_1\rho_1 C_{p_1}}{k_2\rho_2 C_{p_2}}-1\right) \qquad \text{E.3}$$

Equation E.3 can then be inverted in closed form to obtain the heat transfer rate as a function of the surface temperature. The mathematical details of this process are summarized in Reference [63], with the final result shown in Equation E.4,

$$q(t)=\frac{1}{\pi}\sqrt{\pi k_2\rho_2 C_{p_2}}\left(\frac{\pi}{\beta}\frac{T(t)}{\sqrt{t}}+\frac{1}{k_1}\left(\frac{k_1\rho_1 C_{p_1}}{k_2\rho_2 C_{p_2}}-1\right)\beta\frac{T(t)}{\sqrt{t}}\right) \qquad \text{E.4}$$

where:

$$\beta = T(t)\frac{\sqrt{\pi k_2\rho_2 C_{p_2}}}{t} \qquad \text{E.5}$$

This method can be used to convert the wall temperature versus time traces obtained from the surface mounted gauges to surface heat flux. This results of this process were shown in the bottom two plots of Figure 3.2.

Appendix F

Complete List of Experimental and Numerical Tests

This appendix outlines the complete set of experiments performed in Chapters 4 and the numerical investigation completed in Chapter 5.

Table F.1: Complete Experimental Test Matrix

TEST ID	TFS	B1	B2	FUEL, H*
516a	2475	N/A	N/A	N/A
517a	2363	N/A	N/A	N/A
518a	2670	N/A	N/A	N/A
519a	1910	N/A	N/A	N/A
523a	2230	N/A	N/A	N/A
526a	2502	N/A	N/A	N/A
531a	1452	N/A	N/A	N/A
531b	2756	N/A	N/A	N/A
601a	2363	N/A	N/A	N/A
602a	2670	N/A	N/A	N/A
602b	920	N/A	N/A	N/A
602c	2335	N/A	N/A	N/A
603a	2581	1	1	N/A
603b	2864	N/A	N/A	N/A
603c	2475	1	1	N/A
606a	2475	N/A	N/A	N/A
607a	1650	N/A	N/A	N/A
608a	2080	N/A	N/A	N/A
608b	2625	N/A	N/A	N/A
608c	1900	N/A	N/A	N/A
608d	1176	N/A	N/A	N/A
608e	2363	N/A	N/A	N/A
609a	1825	N/A	N/A	N/A
612a	1939	N/A	N/A	N/A
613a	2670	N/A	N/A	N/A
613b	1910	N/A	N/A	N/A
614a	963	N/A	N/A	N/A
614b	2335	N/A	N/A	N/A
619a	2401	1	1	N/A
619b	1965	1.5	0.5	N/A
619c	1254	1.5	0.5	N/A
620a	2560	1	1	N/A
620b	1652	1.5	0.5	N/A
623a	2548	1	1	0.044
626a	2563	1	1	0.048
626b	2485	2	2	0.108
627a	2478	2	2	0.107
627b	2680	2	2	0.516
628a	2760	1	1	0.602
630a	2744	2	2	0.644
630b	2763	1	1	0.802
630c	1451	1.75	1.75	N/A
711a	2236	1.75	1.75	N/A
711b	2805	N/A	1	N/A
711c	2768	1.75	1.75	N/A
001a	2554	0.5	0.5	N/A
002a	2487	1	1	N/A
004a	2748	0	0.5	N/A
006a	2731	0	1	N/A
007a	2795	0	2	N/A
008a	1170	0.5	0.5	N/A
009a	2580	0.5	0.5	N/A
010a	2585	1	1	N/A
011a	2565	2	2	N/A
012a	2350	1	1	0.581
013a	1250	1	1	0.520
014a	1355	1	1	0.517
015a	1650	1	1	0.520
016a	2080	1	1	0.509
017a	2625	1	1	0.202
018a	1900	1	1	0.528
019a	2230	1	1	0.564
020a	2502	1	1	0.556
020b	2475	0.5	0.5	0.048
020c	2363	0.5	0.5	0.186
021a	2670	2	2	0.647
022a	1910	2	2	0.639
022b	963	2	2	0.517
023a	2335	2	2	0.697
024a	2581	0.5	0.5	0.738
025a	1965	0.5	0.5	0.437
025b	1254	0.5	0.5	0.553
026a	2560	0.5	0.5	0.556
027a	2551	0.5	0.5	0.213
027b	1253	0.5	0.5	0.182
028a	2752	0.5	0.5	0.073
028b	1380	0.5	0.5	0.069
029a	2841	2	2	0.233
029b	2759	2	2	0.175
030a	2804	2	2	0.084
030b	1155	2	2	0.073
031a	890	1	1	0.161
031b	1256	1	1	0.018
031c	1608	1	1	0.173
031d	2360	1	1	0.176
032a	950	1	1	0.042
032b	1455	1	1	0.042
032c	2753	1	1	0.044

The next section summarizes the numerical studies presented in Chapter 5.

Table F.2: Complete Numerical Test Matrix

Key to Test Cases and Grids:

*.msh = Tgrid mesh file *.dbs = Gambit database file (mesh + geometry) **bold** = used primarily

1. Tutorial Grids	/u3/kfid/project1/tutorial
film_hex.msh	duct (hex)
film_tet.msh	plenum and hole (tet)
filmcool.msh	duct, plenum, hole (hex and tet)
2. Inlet hole grids	/u3/kfid/project1/hole_only
hole2.dbs	inlet hole geometry
hole1.dbs	meshed inlet hole geometry (tet), interval size = 0.05 (1D/.5) = 0.1D
hole3.dbs	meshed inlet hole geometry (tet), interval size = 0.1 (1D/.5) = .2D
3. Duct only grid	/u3/kfid/project1/duct_only
duct2.dbs	duct geometry, experimental
duct3.dbs	meshed duct geometry (hex), boundary layer present
duct4.dbs	duct geometry, unmeshed except boundary layer
duct5.dbs	coarsely meshed duct geometry (tet), interval size = 0.5 (1D/.5) = 1D
4. Duct and inlet hole	/u3/kfid/project1/duct_hole
duct_hole.dbs	two volume geometry
duct_hole2.dbs	two volume geometry
duct_hole3.dbs	one volume geometry
duct_hole8.dbs	same as duct_hole3.dbs
duct_hole9.dbs	meshed one volume geometry (tet), interval size=0.4 (1D/.5)=0.8D, finely meshed inlet
duct_hole10.dbs	meshed one volume geometry (tet), grid density similar to Walters and Leylek.

Baseline Cases and Grids:

1. filmcool.cas	filmcool.msh, tutorial grid with plenum
2. filmcool_run3.cas	hole1.dbs and duct3.dbs (hex grid)
3. filmcool_run1200a.cas:	filmcool_run3.cas; duct refined manually ahead of hole
4. tet_run1200.cas	10,350 cell grid; dense inlet hole; sparse duct
5. tet2_run1200.cas	8,662 cell unstructured grid; sparse
6. tet_run1200a.cas	14,564 cell unstructured grid; dense inlet hole; slightly refined duct
7. tet_run1200b.cas	20,500 cell unstructured grid; dense inlet hole; manually refined duct
8. tet3_run1200a.cas	148,237 cell unstructured grid; 1 volume; used duct_hole10.dbs
9. tet3_run1200k.cas	181,802 cell unstructured grid; refined on pressure and velocity gradients from tet3_run1200a.cas
10. 1200v2.cas	169,083 cell unstructured grid; refined on temperature gradients from tet3_run1200a.cas
11. abc.cas	grid same as tet3_run1200a.cas; species transport and reactions enabled. $a + b \rightarrow c$ a: hydrogen like b: oxygen like c: water vapor like species entering into duct: ar,a (.9962, .0038) (mass fractions) species entering into inlet hole: air, b (.77, .23) Mass flow inlet mass fraction of b chosen arbitrarily (assumed b in similar concentration to oxygen in air). From this choice, the mass fraction of a was determined based on molar masses, stoichiometric coefficients, relative mass flows, and expected area of interaction.
12. ar_air.cas	grid same as tet3_run1200a.cas; species transport enabled; Ar entering duct, air entering inlet hole

Data Files:

File name	T_f	T_c	u_f	u_c	ρ_f	$\rho_c u_c$	B	DR	ρ_c	path
filmcool.dat	273	136.5	20	11.5	1.29	29.8	1.16	2.0	1.6	/tutorial
	filmcool.cas: tutorial grid, tutorial conditions, Air/Air									
filmcool3_1.dat	300	285.7	10	4.49	1.18	4.71	0.4	1.05	1.235	/tutorial
	filmcool.cas: tutorial grid, conditions same as in Atul Kohli's experiment, Air/Air									
filmcool1850a.dat	1850	300	200	15.6	1.11	110	0.5	6.4	7.1	/tutorial
	filmcool.cas: tutorial grid, shock tube experimental conditions, Air/Air									
filmcool2500a.dat	2500	300	280	16.3	.81	114	0.5	8.6	7.0	/tutorial
	filmcool.cas: tutorial grid, shock tube experimental conditions, Air/Air									
filmcoolnp.dat	300	285.7	10	4.49	1.176	4.71	0.4	1.05	1.235	/tutorial
	filmcoolnp.cas: tutorial grid without plenum, Atul Kohli's conditions, Air/Air									
filmcool_run3a.dat	1200	300	20	3.5	2.43	24.3	0.5	2.9	7.0	/runs_hex
	filmcool_run3.cas: hex grid, approximately tutorial conditions, Argon/Air (*)									
filmcool_run1200a.dat	1200	300	194	34	2.43	235.7	0.5	2.9	7.0	/runs_hex
	filmcool_run3.cas: hex grid, shock tube conditions, Argon/Air (*)									
filmcool_run1200b.dat	1200	300	194	135	2.43	943	2	2.9	7.0	/runs_hex
	filmcool_run3.cas: hex grid, shock tube conditions, high blowing ratio, Argon/Air(*)									
filmcool_run1850a.dat	1850	300	240	29	1.58	189	0.5	4.1	6.5	/runs_hex
	filmcool_run3.cas: hex grid, shock tube conditions, Argon/Air (*)									
filmcool_run1850b.dat	1850	300	240	116	1.58	756	2	4.1	6.5	/runs_hex
	filmcool_run3.cas: hex grid, shock tube conditions, high blowing ratio, Argon/Air (*)									
filmcool_run2500a.dat	2500	300	280	24.7	1.17	163	0.5	5.7	6.6	/runs_hex
	filmcool_run3.cas: hex grid, shock tube conditions, Argon/Air (*)									
filmcool_run2500b.dat	2500	300	280	24.7	1.17	163	0.5	5.7	6.6	/runs_hex
	filmcool_run3.cas: hex grid, shock tube conditions, extra 300 iterations, Argon/Air (*)									

Numerical Test Cases:

File name	T_f	T_c	u_f	u_c	ρ_f	$\rho_c u_c$	B	DR	ρ_c	path
tet3_run1200a.dat	1200	300	20		1.77	17	0.5		7.1	/runs_tet
	tet3_run1200a.cas: tet grid, approximately tutorial conditions, Air/Air									
tet3_run1200e.dat	1200	300	208		1.77	184	0.5		6.73	/runs_tet
	tet3_run1200a.cas: tet grid, shock tube conditions, Air/Air									
tet3_run1200f.dat	1200	300	208		1.67	184	0.5		6.73	/runs_tet
	tet3_run1200a.cas: tet grid, shock tube conditions, extra iterations, Air/Air									
tet3_run1200h.dat	1200	300	208		1.67	294	0.8		6.78	/runs_tet
	tet3_run1200a.cas: tet grid, shock tube conditions, increased blowing ratio, Air/Air									
tet3_run1200i.dat	1200	300	208		1.67	368	1.0		6.8	/runs_tet
	tet3_run1200a.cas: tet grid, shock tube conditions, increased blowing ratio, Air/Air									
tet3_run1200j.dat	1200	300	208		1.64	1473	4.0		7.6	/runs_tet
	tet3_run1200a.cas: tet grid, shock tube conditions, increased blowing ratio, Air/Air									
tet3_run1200k.dat	1200	300	208		1.66	184	0.5		6.9	/runs_tet
	tet3_run1200k.cas: tet grid refined on pressure and velocity , shock tube conditions, Air/Air									
tet3_run1200l.dat	1200	300	208		1.61	1841	5.0		8.14	/runs_tet
	tet3_run1200a.cas: tet grid, shock tube conditions, increased blowing ratio, Air/Air									
tet3_run1200m.dat	1200	300	208		1.67	736	2.0		6.96	/runs_tet
	tet3_run1200a.cas: tet grid, shock tube conditions, increased blowing ratio, Air/Air									
tet3_run300a.dat	300	285.7	10		1.176	4.71	0.4	1.05	1.235	/runs_tet
	tet3_run1200a.cas: tet grid, Atul Kohli's conditions, Air/Air									
1200v1.dat	1200	300	208		1.67	184	0.5		6.73	/runs_tet/refine_temp
	1200v1.cas: same as tet3_run1200a.cas.									
1200v2.dat	1200	300	208		1.67	184	0.5		6.73	/runs_tet/refine_temp
	1200v2.cas: tet grid refined on temperature gradients, Air/Air									
abc.dat	1200	300	20		2.27	24.3	0.5		7.25	/runs_tet/combust
	abc.cas: simple combustion model a + b → c									
ar_air4.dat	1200	300	194		2.29	235.7	0.5		6.66	/runs_tet/argon_air
	ar_air.cas: tet grid, experimental conditions, species transport enabled: Ar/Air									

Appendix G

Experimental Error and Uncertainty Analysis

This Appendix presents calculation of the experimental uncertainties to generate the uncertainty band shown in Figure 4.10. The spreadsheet used to calculated the error bars is summarized below:

Table G.1: Error and Uncertainty Analysis Summary

Item	**How Obtained**
Damkholer number	flow time / chemical time
flow time	L/u_∞
L: characteristic length scale	blade length scale or x/D
u_∞: flow velocity	CFD stream lines
chemical time	
fuel level	range of estimates
ΔT_t	calculation

EXPERIMENT

Notes:

For both facilities, wall temperature as a function of time is the basis measurement with all other quantities calculated.

Two types of error categories are considered:

1) absolute error: knowing the absolute value of the calculated quantities

2) differential error: knowing the value of the calculated quantities of the differential experiment with respect to each other.

For example, using the shock tunnel experiments, the wall temperature is known to better than 1%, and q is known to better than 1%.

However, the difficulty occurs in inferring the mainstream temperature, which is calculated from the shock speed.

Total temperature is known to 10%, and consequently, although q and T_w are well known, the absolute h, h = / (T_∞-T_w), is known to 10%.

Item	**How Obtained**	**Absolute Case**	**Differential Case**
Absolute Case			
T_∞, freestream temperature	Calculated		N/A
Tc, coolant temperature	Measured (upstream plenum)		N/A
Tw, wall temperature	Measured at surface		
q, heat flux	Calculated	20-50 K	N/A
h, heat transfer coefficient, wall	Calculated		
η_f, film effectiveness	Calculated	2-5 %	N/A
h_g, heat transfer coefficient, film	Calculated	2-3 %	N/A
T_f, film temperature	Calculated	1-2.5 %	N/A
Differential Case			
T_∞, freestream temperature	Calculated		10% N/A
T_c, coolant temperature	Measured (ambient)		1% N/A
T_w, wall temperature	Measured	< 1 %	< 1 %

q, heat flux	Calculated	< 1 %	< 1 %
h, heat transfer coefficient, wall	Calculated	5-10 %	< 1 %
h_f, film effectiveness	Extrapolated	10-45 %	< 5%
h_g, heat transfer coefficient, film	Extrapolated	10-45 %	< 5%
T_f, film temperature	Extrapolated	10-45 %	< 5%

Analysis

Damkholer number			
flow time			
L: characteristic length scale	x/D = 10		
gauge installation location	< 0.01"		
u_∞: flow velocity	calcualted: M * a		
choked area	7.295 in2		
housing area	26.67 in2		
gemoetric area blockage	3.3265 in2		
boundary layer blockage			
speed of sound	calculated sqrt(gamma * R * T_∞)		
driven composition	measured from partial pressure		
Mach number		0.3125	
incident shock Mach number, Ms	measure from transducers		

chemical time			
$T_{t\infty}$, freestream temperature	calcualted from incident Ms		10%
fuel level	set from partial pressure in tank		
driven pressure	partial pressure		
mixture pressure	total mixture of Argon / Fuel		

Blowing Parameter			
$B = (u_\infty * \rho_\infty) / (u_c * \rho_c)$			
transducer pressure	0.2 - 0.036 % error at transducer		
injected gas temperature	taken as room temperature		
choked orifice diameter	known to within 0.01"		
plenum pressure	1 - 0.5 %		
$T_{t\infty}$	10-15%		
total error in blowing paramter		20%	
introduced error in film effectiveness		25%	

COMPUTATIONAL FLUID DYNAMICS STUDIES

grid error		
turbulence modeling		
Damkohler number		
flow time scale	L/u_∞	
L, characteristic length	set to 10 x/D	known precisely
u_∞	taken as the freestream velocity	u_∞ = 20-150 m/s
chemical time scale	estimated as 1/ kf	
A, pre-exponential factor	set in code to control Da	known precisely

Ea, activation energy	set value	known precisely
R	taken for Argon only, not mixture	< 2 %
T	taken as freestream temperature	T range: T_c - T_{ad} at wall
b	T_∞ exponent	estimated from literature
lateral vs. centerline measurement	function of x/D location and B	
attached jet	centerline is not max temperature	
lifted jet	centerline is max temperature	
film effectiveness	function of x/D, z/D and B	
attached jet	max degradation not at centerline	
lifted jet	max degradation at centerline	

MODELS AND DESIGN TOOLS

linear fit through data points	
Damkohler number error	primary source of error in T_∞
without calibration to flat plate	10 - 15 %
calibration to flat plate	< 10 %, depending on x/D
Qs	
q_{cold}	integrated Tw vs. t
q_{hot}	integrated Tw vs. t
q_{max}	heat flux evaluated at Tad
T_{ad}	calculation
fuel level	known to within 3 %
$T_{r\infty}$	10 - 15 %
model employed for variation in h	
depends on initial and final temperatures	
constant pressure heat addition	5 - 8 % decrease in h
constant Mach number hear addition	2 - 4 % decrease in h
constant area heat addition	2 - 4 % increase in h